FACHBEREICH C - PHYSIK
BERGISCHE UNIVERSITÄT
WUPPERTAL

Search for Signatures of Extra-Terrestrial Neutrinos with a Multipole Analysis of the AMANDA-II Sky Map

Jan-Patrick Hülß

Diplomarbeit

Fachbereich C - Physik
Bergische Universität Wuppertal

Juni 2006
WU D 06-04

Contents

List of Figures

List of Tables

1 Introduction

Astroparticle physics uses elementary particles arriving at the earth to explore the universe. These particles are used as messengers from remote regions. A great variety of experiments has been installed to detect the various particles. They have in common to obtain information about the source objects or probe the big bang scenario. One of these experiments is the AMANDA neutrino telescope at the South Pole. The main purpose of the telescope is to detect astrophysical neutrinos.

The data of the AMANDA detector can be analysed in various manners to obtain information about the extra-terrestrial neutrino sources (diffuse or point like). Here, the data is investigated for characteristic signatures at different angular scales. The presented analysis studies the angular power spectrum of neutrino events. As reference the power spectrum of atmospheric neutrinos is used. This is our basic background and will dominate the data set. The goal of this work is to study the deviation or non-deviation of the measured data from this background in a statistical way.
We have to face the situation of different source types. Each source type has its own characteristic angular power spectrum. This offers the opportunity to search for angular structures like the galactic or super galactic plane as well as to look for small scale structures produced by neutrinos from point sources.
For different source hypotheses simulations are made to understand the characteristics in the angular power spectra. These hypotheses are based on many parameters and we show how they influence the analysis. The simulations are based on a Monte Carlo data set describing the full detector response, the trigger and the reconstruction. This is necessary because the angular power spectrum is affected by the detector resolution as well as by the detector acceptance and the reconstruction efficiency.
A similar method has already been used to analyse the anisotropies in the cosmic background radiation (WMAP). In comparison a data set of much smaller statistics is used here. Additional problems and effects have to be considered, e.g. structures due to the detector acceptance and correlations in the angular power spectrum.

This thesis will explain the theoretical basis of neutrino physics and possible neutrino sources in chapter 2. Then, the general detection technique and the AMANDA detector are explained in chapter 3. The analysis procedure (chapter 4 and 6) and the required simulations (chapter 5) are discussed. Finally, the result for the angular power spectrum of the measured data is obtained in chapter 7 and limits on the contributions from differed source hypotheses are set (chapter 9 and 10). Additionally, tests of the data sample are performed in chapter 8.

2 High Energy Neutrinos

This chapter provides an overview on the properties of neutrinos. Section 2.1 summarises the general properties, with special emphasis put on neutrino oscillations. Afterwards terrestrial (chapter 2.3) and cosmic (chapter2.4) neutrino sources and the corresponding fluxes are discussed.

2.1 General Properties of Neutrinos

Neutrinos are elementary particles (fermions with spin 1/2) and part of the standard model of particle physics. Three types of neutrinos (so called flavours) are known: the electron-, muon- and tau-neutrino and their corresponding anti-particles. Neutrinos are the lightest massive particles in the standard model with very small masses. They have no electrical or colour charge. Thus, they interact only via the weak force and have a very small interaction cross section. Parity violation of the weak interaction induces a fixed helicity (relation between spin direction and moment) for massless neutrinos. Neutrinos have a helicity of -1 and it is 1 for anti-neutrinos.[Pe91]

2.1.1 Neutrino Oscillation

An important property of non massless neutrinos are neutrino vacuum oscillations. This effect occurs because of the difference between the weak eigenstates ν_e, ν_μ, ν_τ and the mass eigenstates ν_1, ν_2, ν_3. Both sets of eigenstates are a linear combination of the other set. Considering only oscillations between two flavours the mixing is described by:

$$\nu_\mu = \nu_1 \cos\theta + \nu_2 \sin\theta \quad \text{and} \quad \nu_e = -\nu_1 \sin\theta + \nu_2 \cos\theta \; . \tag{1}$$

Here θ is the mixing angle between electron- and muon-neutrinos. Neutrinos are produced and decay only in weak (flavour) eigenstates. The propagation is determined by the evolution of their mass eigenvalues:

$$\nu_1(t) = \nu_1(0) e^{-iE_1 t} \quad \text{and} \quad \nu_2(t) = \nu_2(0) e^{-iE_2 t} \; . \tag{2}$$

t is the time and E_i is the energy of the neutrino (here $c = \hbar = 1$ is used). At energies E_i much larger than the mass m_i the following equation can be used:

$$E_i = p + \frac{m_i^2}{2p} \; . \tag{3}$$

For identical momentum p the oscillation is determined by the neutrino mass. So flavour changes are possible while travelling. The probability for not changing the flavour is [Pe91]:

$$P(\nu_\mu \to \nu_\mu) = 1 - \sin^2(2\theta) \sin^2\left(\frac{1.27 \Delta m^2 L}{E}\right) \; . \tag{4}$$

$\Delta m^2 = m_1^2 - m_2^2$ is the squared mass difference in $(\mathrm{eV}/c^2)^2$. L denotes the travelling distance in meters and E the neutrino energy in MeV.

There are compelling pieces of evidence for neutrino oscillations. (E.g. Super-Kamiokande, SNO or KamLAND measurements) [PP04].
The observation of neutrino oscillation, means $\Delta m^2_{ij} = m^2_i - m^2_j \neq 0$. Thus, at least two neutrino masses cannot be zero. Values for Δm^2 for atmospheric (90% CL[1]) and solar neutrinos (best fit values from solar and KamLAND) [PP04] are:

$$1.3 \cdot 10^{-3}\ \text{eV}^2 < \Delta m^2_{atms.} < 3 \cdot 10^{-3}\ \text{eV}^2 \ \text{ and } \ \Delta m^2_{sol.} \approx 1.7 \cdot 10^{-5}\ \text{eV}^2\ , \tag{5}$$

$$\sin^2 2\theta_{atms} > 0.9 \text{ and } \sin^2 2\theta_{sol.} \approx 0.82\ . \tag{6}$$

Here, the squared mass differences are denoted by "atms." and "sol." because is is not sure which of the possible mass differences $(\Delta_{12}, \Delta_{13}, \Delta_{23})$ is observed. These results only imply a non-zero mass difference but provide no information on the absolute scale of the neutrino masses. One reason is the unknown hierarchy. Direct upper limits for the neutrino masses are [PP04]:

$$\begin{array}{lll} m_{\nu_e} & < 3 \text{ eV} & (90\%\text{CL}) \\ m_{\nu_\mu} & < 0.19 \text{ MeV} & (90\%\text{CL}) \\ m_{\nu_\tau} & < 18.2 \text{ MeV} & (95\%\text{CL}) \end{array} \tag{7}$$

These limits do not include the restrictions from neutrino oscillation.

2.2 Cosmic Information Messenger

Figure 1 shows the different astronomical messengers. Hadrons (e.g. protons) can be accelerated at sources. An accelerated proton produces different secondary particles in interactions with a target. Furthermore, decay of unstable particles results in protons (α nuclei), neutrinos and gammas. High energy photons are absorbed on their way through the universe. Charged particles change their direction due to magnetic fields. Neutrinos travel without interactions on nearly all energy scales to the earth. Thus, they point directly to the source making them ideal cosmic messengers.

The mean free path λ depends on the neutrino cross section $\sigma(E)$ and the matter number density of the universe n [Ne04]:

$$\lambda = \frac{1}{\sigma(E) n}\ . \tag{8}$$

A typical neutrino energy of this work is 1 TeV. In this case the cross section is $\sigma \simeq 10^{-35}$ cm^2. Assuming a nucleon density n of about 6 nucleons /m^3 (critical nucleon density of the universe) one finds $\lambda = 5.4 \cdot 10^{21}$ lightyears (ly). This is 11 orders of magnitude larger than the horizon of the observable universe $1.4 \cdot 10^10$ ly [Be03]. Even uncertainties in this approximation due to non-isotropic mass distribution or other effects cannot compensate this difference of 11 orders of magnitude. (For example dark energy might interact weakly.) The flavours of the neutrinos oscillate while travelling through the universe. Therefore, for an estimation of the flavour ratio of the neutrinos arriving at the earth, the initial ratio need not to be known precisely. As mentioned above the neutrinos are produced in interactions of protons with the source. In these interactions many different particles

[1] CL = confidence level

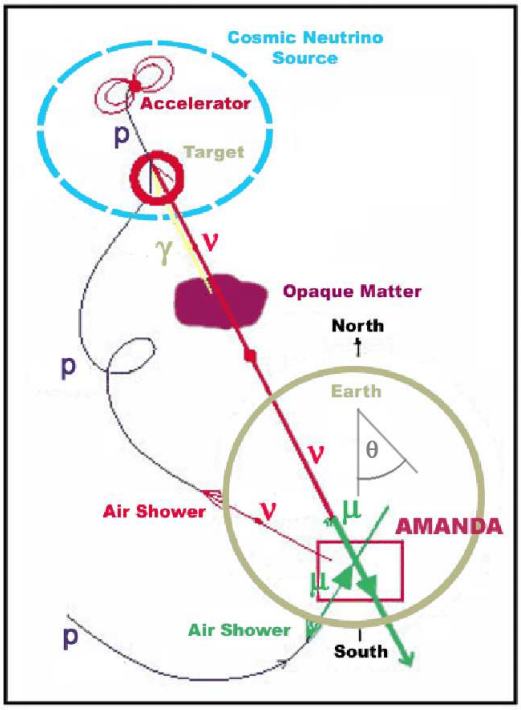

Figure 1: Astronomic Messengers.

are produced. An important production channel for neutrinos is the pion decay into a muon-neutrino and a muon. The muon decays into an electron and an additional muon- and electron-neutrino.

$$\pi^+ \to \mu^+ + \nu_\mu \quad ; \quad \pi^- \to \mu^- + \bar{\nu}_\mu \tag{9}$$

$$\mu^+ \to e^+ + \bar{\nu}_\mu + \nu_e \quad ; \quad \mu^- \to e^- + \nu_\mu + \bar{\nu}_e \tag{10}$$

From this channel a composition of $\nu_e : \nu_\mu : \nu_\tau = 1 : 2 : 0$ is generated. The distance to the sources from the earth is large compared to the length for oscillations, so full mixing is expected. Under the assumption of the mixing angles observed by neutrino oscillation experiments [PP04] a ratio of $\nu_e : \nu_\mu : \nu_\tau = 1 : 1 : 1$ is expected to be observed at the earth. This is described in detail in [GM03].

We will discuss the measurement technique for these values in chapter 3.2.

2.3 Terrestrial Neutrino Sources

The dominant source of terrestrial neutrinos are air showers induced by cosmic particles. Above 1 GeV the energy spectrum of the cosmic rays is proportional to $\sim E^{-2.7}$ (figure 2). It slightly steepens at the so called "knee" ($\sim 10^{15}$ eV) and flattens again at the "ankle" ($\sim 5 \cdot 10^{18}$ eV).
When a high energetic cosmic particle interacts with the atmosphere of the earth it produces particles which also interact. The induced showers contain many different particles.

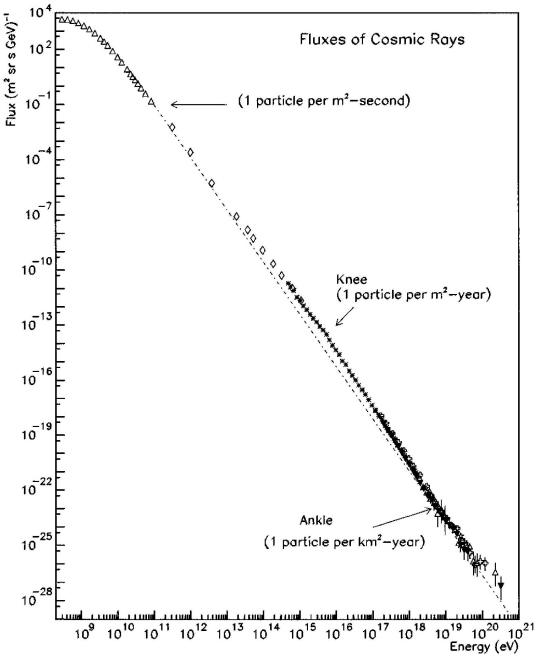

Figure 2: Energy spectrum of cosmic rays.[Sw97]

The neutrinos originate from decays of kaons, pions, muons and charm particles. Neutrinos originating from charm particles are called "prompt neutrinos".
The flux of neutrinos from pion decay is given by [Ga90]:

$$\frac{dN_\nu}{dE_\nu} = \frac{N_0(E_\nu)}{1 - Z_{NN}} \left[\frac{A_{\pi\nu}}{1 + B_{\pi\nu} \cos\theta E_\nu / \epsilon_\pi} + (...) \right] \tag{11}$$

where $A_{\pi\nu} = Z_{N\pi}(1 - r_\pi)^{(\gamma-1)}/\gamma, r_\pi = (m_\mu/m_\pi)^2$ and γ is the power index of the primary energy spectrum. $B_{\pi\nu}$ is a constant with respect to the energy and depending on the nucleon and pion attenuation lengths. ϵ_π reflects the ratio of decay and interaction in the medium. For cascades in the earth's atmosphere this is $\epsilon_\pi \sim 115$ GeV. The nadir angle θ is included here because of the angular dependent effective decay length of the mesons. As the high atmosphere is less dense, horizontal mesons travel a larger distance through thin air and the interaction probability is smaller, while the decay rate is higher. [Ga90]
(...) represents the contributions of other mesons which must not be neglected. They can be parametrised in the same way. These have different energy scales: $\epsilon_{K^\pm} \sim 850$ GeV and $\epsilon_{D^\pm} \sim 4 \cdot 10^7$ GeV. Additionally, the branching ratio has to be taken into account. For pions this is about one, but for kaons ($K^\pm \to \mu + \nu_\mu$) this is only 0.64. For neutrino energies E_ν below ϵ_i $i = \pi, K, D$ the neutrino energy spectrum follows the primary flux, because all mesons decay. For $E_\nu > \epsilon_i$ the spectrum steepen by one power of E_ν. Muons are not included here, because for energies $E_\mu > 2$ GeV they reach the ground and stop before decaying.
The neutrino spectrum is dominated by neutrinos from different source processes at different energy scales. The low energetic neutrinos are mostly from pion decay, while at higher

energies the kaon decay dominates. This leads to a power index of $\gamma \sim 2.7$ corresponding to the initial spectrum up to ~ 100 GeV and $\gamma \sim 3.7$ above. Additionally, the spectrum has a characteristic angular dependency with more neutrinos from the horizontal direction. Prompt neutrinos can be described similarly to the mesons. The difference is the higher energy scale ($\epsilon_{charm} \sim 10^4$ TeV) and an isotropic distribution. The lifetime of theses particles is so short that most of them decay. The energy spectrum remains with an index of $\gamma \sim 2.7$ also at high energies. At a scale of $10 - 100$ TeV prompt neutrinos eventually dominate the energy spectrum.

2.3.1 Oscillation of Atmospheric Neutrinos

The neutrinos generated in the atmosphere change their flavour while travelling through the earth to the detector. For a fixed energy E the oscillation depends only on the length L the neutrinos travel before reaching the detector (equation (4)). The distance between the origin and the detector is fixed by geometry (figure 1). The oscillation is zenith angle dependent. The distance L is:

$$L \approx 2R_{earth} \sin\theta/2 \; . \tag{12}$$

$R_{earth} = 6342$ km is the radius of the earth. Figure 1 shows the nadir angle θ.

2.4 Extra Terrestrial Sources of High Energy Neutrinos

High energetic neutrinos are also expected from various objects in the universe. The production mechanism of these neutrinos is similar to the production in air showers. The neutrinos originate from interactions of high energetic hadrons. A possible acceleration mechanism for hadrons is the Fermi-acceleration (chapter 2.4.1).
Candidates for sources of high energetic neutrinos have to fulfil some requirements. Protons must be available and for Fermi-acceleration high magnetic fields must exist. Additionally there must be targets for producing neutrinos. These targets could also be the particles or even the shock front itself. Thus, the detection of neutrinos from a source would be a proof of hadronic acceleration.

Candidates fulfilling these requirements are supernova remnants, active galactic nuclei and micro quasars. They are discussed in the following chapters (2.4.2 - 2.4.4). Other candidates for sources of high energetic neutrinos can exist (e.g. WIMP[2] annihilations [Ga94]). High energy neutrinos also are also expected in top-down scenarios [LeMa]. Such possibilities are not discussed further in the context of this work.
Additional candidates for neutrino sources are proposed which do not accelerate particles by their own. One source of this type is the galactic plane filled with interstellar matter. Here high energy cosmic rays can interact producing neutrinos. (chapter 2.4.5).

2.4.1 Fermi-Acceleration

Neutrinos themselves cannot be accelerated to high energies. An acceleration mechanism for charged particles which then may produce secondary neutrinos is the Fermi-acceleration [Fe49][Ga90].

[2]WIMP = weakly interacting massive particle

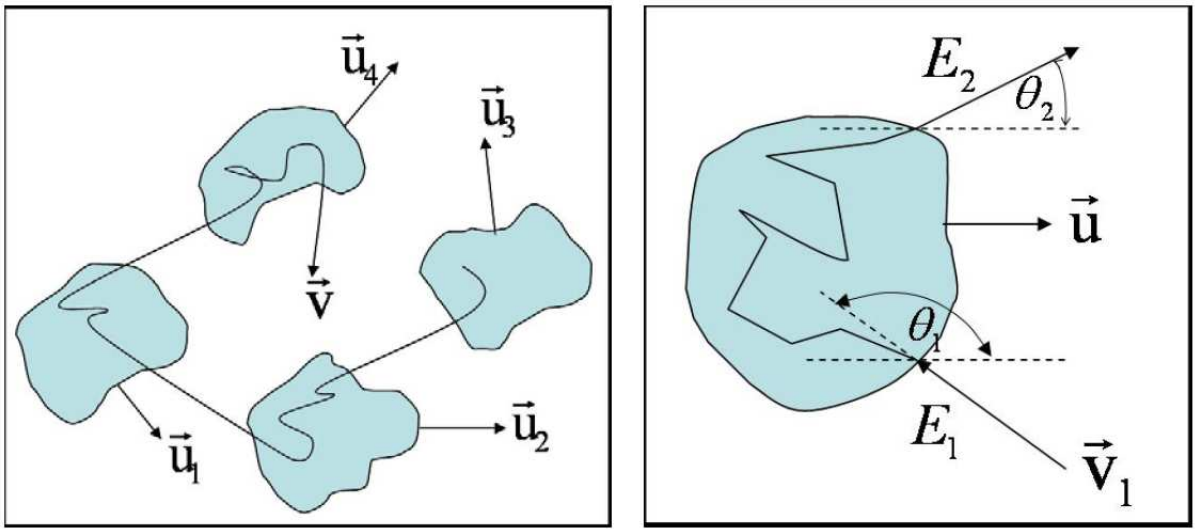

Figure 3: Fermi-acceleration. Left: Step vise acceleration by different clouds. Right: Sketch for the interaction with a cloud

Fermi-acceleration is based on a step-wise energy transfer by scattering at magnetic fields. This can be induced by partly ionised gas clouds or shock waves of changing matter density. A gas cloud has a typical speed of about $v_c \sim 15$ km/s. This is small compared to the speed of light $\beta_c = v_c/c < 10^{-4}$. A high energetic charged particle scatters elastically at this magnetic field. The interaction can be treated as scattering without energy transfer in the system of the gas cloud because of the huge mass of the gas cloud. In a system not moving with the cloud the particle can loose or gain energy depending whether it is a head-on or a tail-on collision. Calculating the energy before E_1 and after E_2 the interaction using the entry angle θ_1 and leaving angle θ_2 to the cloud leads to (figure 3):

$$E_1' = \gamma E_1(1 - \beta_c \cos\theta_1) \qquad E_2 = \gamma E_2'(1 + \beta_c \cos\theta_2') \; . \tag{13}$$

This calculation is done by transformations between the different rest systems. The system of the cloud is marked with a "′". There is no change of the energy in the clouds rest system: $E_1' = E_2'$. The relative energy change is given by:

$$\frac{\Delta E}{E} = \frac{E_2 - E_1}{E_1} = \gamma^2(1 - \beta_c \cos\theta_1)(1 + \beta_c \cos\theta_2') - 1 \; . \tag{14}$$

To obtain the expectation value for the energy change, the expectation for the angles are required. In the rest system of the cloud no direction is preferred. Thus, the expectation value is $< \cos\theta_2' >= 0$. For the initial particles an isotropic distribution is assumed. More particles flying in the opposite direction interact with the cloud. The direction distribution of the particles for a solid angle element is proportional to the relative velocity between the cloud and the particle.

$$\frac{dn}{d\cos\theta_1} = \frac{c - v_c \cos\theta_1}{2c} \tag{15}$$

Here, a relativistic particle is assumed. This leads to an expectation value of $< \cos\theta_1 >= -\beta_c/3$. From this results follows:

$$\epsilon = \left\langle \frac{\Delta E}{E} \right\rangle = \frac{1+\beta_c^2/3}{1-\beta_c^2} - 1 \approx \frac{4}{3}\beta_c^2 \ . \tag{16}$$

On average a particle gets energy scattering at a magnetic field. The relative additional energy is proportional to $\beta_c^2 < 10^{-8}$. This is called "Second Order Fermi-acceleration". Here, the particle gets only a very small amount of energy ϵ. In fact, the second order Fermi-acceleration is too inefficient to produce high energetic protons in reasonable time scales.
The acceleration to the high energies are better explained by the "First Order Fermi-acceleration". This kind of acceleration appears at shock waves. E. g. shock waves are generated when a supernova shoots material into the surrounding interstellar matter. The speed is about 10^4 km/s, above the speed of sound. In the front the interstellar matter is compressed together with the inherent magnetic fields. Here, the boost has always the same direction due to the fixed propagation direction of the shock front. The energy transfers are calculated similar to the second order Fermi-acceleration. The change of the energy is:

$$\epsilon = \left\langle \frac{\Delta E}{E} \right\rangle \approx \frac{4}{3}\beta_s \ . \tag{17}$$

Compared to the first order Fermi-acceleration this mechanism is thus more effective.

Each particle passes the gas cloud or the shock front more than once. After n interactions the mean energy of these particles is:

$$E_n = E_0(1+\epsilon)^n \ . \tag{18}$$

E_0 is the initial energy. The number of interactions is estimated by the probability for the particle to leave the area of the shock front p. This probability depends on the properties of the shock, the geometry, the thermodynamic parameters and the energy of the particle. For more informations see [Pr98],[Ga90].
The probability for n interactions is $(1-p)^n$. For the energy E, n_0 encounters are required.

$$n_0 = \ln\left(\frac{E}{E_0}\right) / \ln(1+\epsilon) \tag{19}$$

The number $N(> E)$ of particles with an energy greater than E is:

$$N(> E) = \frac{(1-p)_0^n}{p} \propto \frac{1}{p}\left(\frac{E}{E_0}\right)^{-\gamma}, \gamma = \frac{\ln(1/(1-p))}{\ln(1+\epsilon)} \ . \tag{20}$$

This is the observed type of spectrum. The spectral power index γ is not universal, but depends on details of the clouds or shock fronts. For monoatomic gas γ is calculated to be $2+\delta_0$ (δ_0 is a small number). The observed spectrum of cosmic rays at the earth is steeper than this spectrum. This can be understood by the energy dependent diffusion in the galaxy. Particles with higher energies leave the galaxy easier. The spectrum steepens to $E^{-2-\delta_0-\delta}$. For $1-100$ GeV a value of $\delta \sim 0.6$ can be inferred from observed ratios

Figure 4: Picture of a part of the crab nebula, a supernova remnant

of secondary cosmic ray nuclei to their progenitor. The observed spectrum is therefore in good agreement with the prediction from Fermi-acceleration.

For secondary neutrinos the spectrum does not steepen due to the escape probability. Neutrinos travel trough the galaxy independent of their energy. For neutrinos the initial hard $\gamma \sim 2$ spectrum is expected.

2.4.2 Supernova Remnants

A supernova happens if the fusion in a massive star ends. Without thermical power released by fusion the gravitational force is not compensated anymore by the radiation pressure. The core of the star collapses to a neutron star or black hole, compressing protons and electrons to neutrons by inverse β-decay. This process produces electron-neutrinos. A region of high energy density is accumulated and only neutrinos can leave. 99% of the energy is emitted by thermic neutrinos. Their mean energy is $\sim$ 10 MeV, far below the detection limit of for example AMANDA-II. During the collapse the outer part of the shell is blown away with a speed above the sonic velocity of the surrounding interstellar medium. A shock front for Fermi-acceleration develops. Figure 4 shows the crab nebula as example of a supernova remnant.

These shock fronts may accelerate charged particles up to energies of about 100 TeV [Ga90]. The energy spectrum of the cosmic rays below the knee can be explained by supernova remnants. High energetic charged particles produce high energy neutrinos after their acceleration with a spectrum proportional to $E^{-2-\epsilon}$. These sources are expected to be located in the galactic plane.

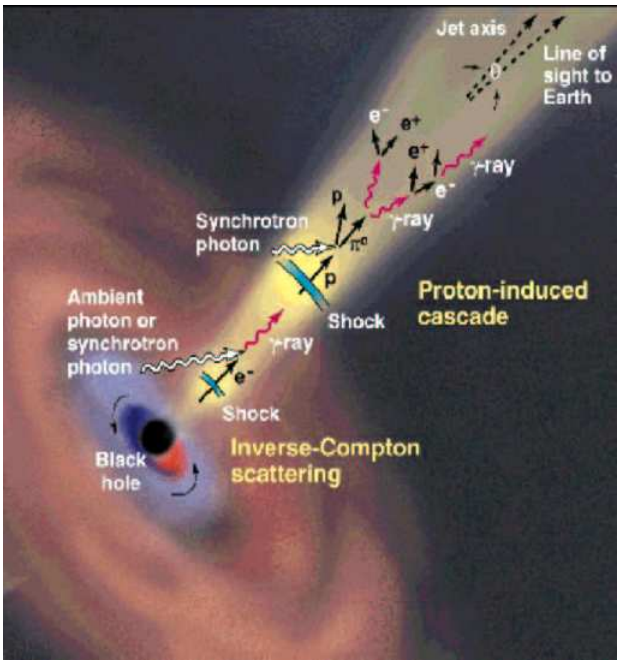

Figure 5: Schematic picture of an AGN with a jet. Different types of accelerated particles and their interaction products are shown.

2.4.3 Active Galactic Nuclei (AGN)

Galaxies can be classified according to their luminosity: One group with "normal" luminosity and the other with high luminosity, called "active". The main part of the radiation originates from the central nucleus of the galaxies.
A model for AGN[3] has to include many different components (figure 5). In the centre of the galactic nuclei is a super massive black hole with a mass of $10^6 - 10^{10}$ solar masses. It attracts mass from the surrounding galaxy. The gravitational force forms an accretion disc perpendicular to the rotation axis of the black hole due to angular momentum conservation. In the accretion disc particles loose energy due to radiation and gain energy from the transformation of potential energy. The particles ionise and the disc contains a plasma. The circular movement of the plasma around the centre induces strong magnetic fields. The stream lines of the field are described in first order by infinite lines parallel to the rotation axis. More precisely the magnetic field is distorted by the movement of the plasma and relativistic effects near the black hole.
In the accretion plane additionally a dust torus is observed at larger distances to the centre. Here, the gravitational force is not strong enough to concentrate the particles to a flat disc. A wider distributed arrangement of the massive particles with a lower temperature is characteristic.
The phenomena of so called "jets" is observed with AGN's. Jets move matter concentrations away from the black hole along the rotation axis of the disc. This matter outflow has a relativistic speed.

[3]AGN = Active Galactic Nuclei

The standard model for AGN can describe different observed phenomena. The appearance depends on the observation direction. In the plane of the accretion disc all particles have to pass the dust torus before they are observed. The spectrum is dominated by the properties of the torus: Low energy photons and narrow absorption lines due to the low speed are observed. At a small angle to the rotation axis the centre is visible. The spectral lines are broad due to the Doppler-effect. Directly along the rotation axis the jets show fluxes of high variability. Such objects are called "Blazars". The variability is at the time scale of days. From causality arguments can be derived that the origin of the jets has a size on a scale at the size of our solar system. This indicates strongly the existence of a black hole in the central region as the mass is expected to be 10^6 solar masses.
In the centre of most galaxies black holes are expected; only some of them are active at the moment. The state can change depending on the amount of absorbed mass. This again depends on the mass of the black hole itself.

An AGN could be an ideal particle accelerator. It has relativistic mass concentrations in the jets and high magnetic fields for Fermi-acceleration. Which type of particles is accelerated? There are two possibilities: a leptonic or a hadronic acceleration, both explain the observed TeV gamma rays (figure 5). The leptonic process assumes that x-rays are produced by synchrotron radiation of accelerated electrons. High energy γ-rays are then produced by inverse Compton-scattering of the electrons with the x-rays. This leptonic acceleration produces no neutrinos. This process would not be visible for a neutrino telescope.
In the case of a hadronic process protons and electrons are injected into the jet. After the acceleration the protons interact and produce pions. Neutral pions decay into high energy gamma rays and charged pions into leptons and neutrinos. For the interaction a partner is required. It can originate from the material of the jet or the interstellar medium.
The neutrino flux from the hadronic process is described by many different models. In general a steep $E^{-2-\epsilon}$ is expected. For the locations of the galaxies two arrangements are meaningful: an isotropic sky distribution or locations in the super galactic plane.
A upper limit for the flux from sources with protons accelerated by the Fermi-acceleration is given by the Waxman Bahcall limit [WB99][BW01]. This limit is derived from measured flux of cosmic ultra high energy hadrons and the assumption of optically thin sources (size not much larger than the mean free path for proton photon interactions). Assuming that the complete energy observed in ultra high energy cosmic rays is transformed into neutrinos one derives a limit $\phi E^2 < 2 \cdot 10^{-8} E^{-2}$ GeV cm^{-2}s^{-1}sr^{-1}.

2.4.4 Micro Quasars

Micro quasars are galactic objects similar to AGNs. The main difference is that they are much smaller. The gravitational object in the centre is supposed to be a neutron star or a black hole of about 10 solar masses. Jets and accretion discs can be observed as well.
Micro quasars are binary systems. The material necessary to build the disc originates from the compending star. The size of the accretion disc of a micro quasar is about 10^{13} km and the length of a jet is some lightyears. The corresponding values for the AGN are a disc of $\sim 10^{19}$ km and jets of a length of some millions of lightyears.(figure 6).
As in the AGN scenario it is possible to have "active" and "non active" phases due to

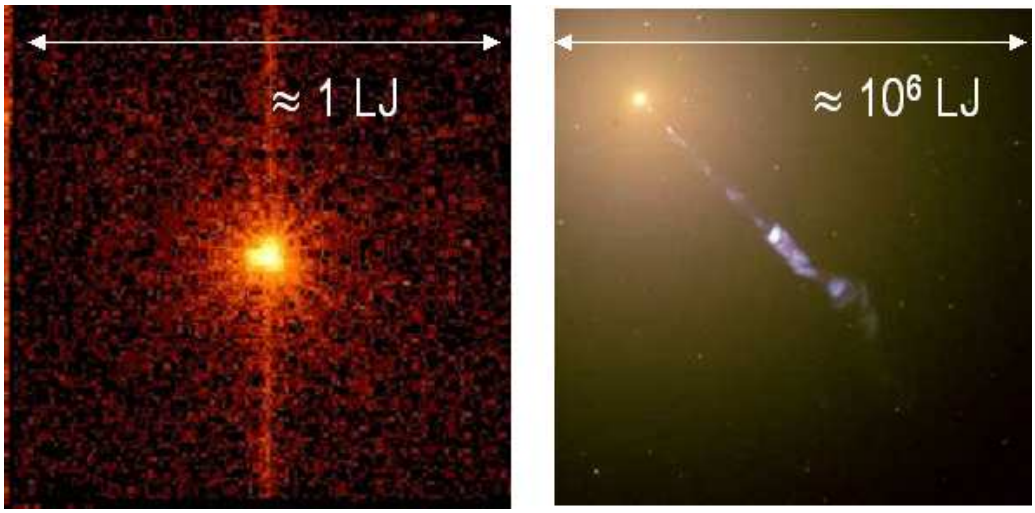

Figure 6: Scale comparison between AGN and micro quasar: Left: picture of a micro quasar. Right: Picture of a AGN

variations in the mass accretion. The changes between these phases is faster due to the smaller dimension. A change between two phases is performed in days. This leads to models for matter collection and emission which is different to the AGN.

The jets of micro quasars are candidates for sources of high energetic neutrinos. They have the initial steep energy spectrum $\sim E^{-2}$ and are located in the galactic plane.

2.4.5 Cosmic Ray Interactions in the Galactic Plane

All previously discussed objects are bottom up accelerators. Protons are accelerated and produce neutrinos in interactions. The galactic plane is not accelerating protons to high energy. It is a different source type.

Here, neutrinos are produced in the interactions of high energetic cosmic rays [Ga94] with the interstellar matter. Pions are produced decaying into neutrinos and leptons. The highest density of interstellar matter is found in the galactic plane.

The flux of this source can be estimated under the assumption of a given cosmic ray density in the galaxy. For photons produced by pions the flux is approximately [Ga94]:

$$\phi_\nu \propto \phi_{(CR)} \rho_{(IM)} \cdot \tag{21}$$

Here $\phi_{(CR)} \approx 1.8 E^{-2.7}$ cm^{-2}sr^{-1}s^{-1}GeV^{-1} is the local cosmic ray flux and $\rho_{(IM)}$ the average density of the interstellar matter. The important fact is the proportionality of the spectrum to the primary spectrum $E^{-2.7}$. It is steeper than the spectrum expected from other extra-terrestrial sources and flatter than the spectrum from atmospheric neutrinos. A limit taking into account the cosmic ray flux $\phi_{(CR)}$ finds a neutrino flux below $\phi_\nu E^{2.7} < 5 \cdot 10^{-5}$ GeV$^{1.7}$cm^{-2}sr^{-1}s^{-1}. This is a guaranteed flux from the direction of the galactic plane, but due to the small scale no observation is expected in actual neutrino-telescopes.

source	γ	μ	distribution d
supernova	2	1,2,3	galactic plane
	2.5	1,2,3	galactic plane
AGN	2	1,2,3	isotropic
	2.5	1,2,3	isotropic
	2	2,3	super galactic plane
	2.4	2,3	super galactic plane
micro quasars	2	2,3	galactic plane
	2.4	2,3	galactic plane
cosmic ray interactions	2.7	-	galactic plane, diffuse

Table 1: Hypotheses for different source types. γ is the index of the energy spectrum and μ is the number of neutrinos in the 4-year-sample per source

2.4.6 Signatures and Search Hypotheses for the Extra Terrestrial Neutrinos

The presented analysis is sensitive to in the sky distribution of the detected neutrinos. The following section summarises the signatures of the discussed source candidates and constructs hypotheses for the later analysis of the AMANDA sky-plot.

The sources discussed above can be characterised by a few relevant parameters. These are the mean source strength denoted by the number of neutrinos in the 4-year-sample from one source μ, the energy spectrum $E^{-\gamma}$ and the source distribution in the sky. The different hypotheses are listed in table 1. All objects (except the galactic plane) are treated as point like sources. For objects larger than the angular resolution of the detector (about 0.0038 sr for AMANDA-II) no separate hypothesis is discussed. This is no limitation of the analysis. The main analysis is independent of the models discussed here. The models are only used to set limits.
For the hypothesis a sources strength is defined. As simplification all sources in one hypothesis have the same strength. The point source analysis for AMANDA-II [IC05] excludes sources with more than a handful neutrinos in the data from 2000 - 2003. The mean number of neutrinos per source μ for this analysis is set to 1,2 or 3. The detector efficiency and the detection probability have to be taken into account. For a source strength μ the number of measured neutrinos follows a Poisson distribution (with mean μ).
The total efficiency depends mainly on the energy spectrum. For E^{-2} the flux (for the assumed μ) is at the scale of $\phi = 10^{-9}$ cm^{-2}s^{-1} and for steeper spectra it is at the scale of $\phi = 10^{-8}$ cm^{-2}s^{-1}.
For the energy spectrum of the point sources the initial spectrum with $\gamma \sim 2$ is used. Additionally a flatter spectrum is assumed. For the cosmic ray interactions the predicted $\gamma = 2.7$ spectrum is used.

Simulations are done for these hypotheses. They are described in chapter 5.

3 Neutrino Observation

In this chapter the detection technique for neutrinos is described. It starts with the information about the general technique in chapter 3.1.
Then the different properties of the AMANDA-II neutrino telescope are discussed in chapter 3.2. The necessary steps for the data filtering and reconstruction are described (chapter 3.3 -3.3.5), and the so called "4-year-sample" used for this analysis is explained in chapter 3.3.6. In chapter 3.4 also the production of Monte Carlo data is described.

3.1 Detection Principle of Neutrino Telescopes

Neutrinos are detected indirectly, by observing the charged leptons produced in neutrino interactions with matter. Neutrinos interact in two ways. First by neutral current interactions:

$$\nu_l + N \rightarrow \nu_l + X \ . \tag{22}$$

N is the interaction partner, a nucleon. X is a hadronic cascade. At energies of interest the nucleon usually is destroyed and a hadronic shower is generated. The second possible interaction is a charged current interaction producing the charged lepton.

$$\nu_l + N \rightarrow l + X \tag{23}$$

Due to the relativistic boost the direction of the charged lepton is closely aligned with the initial neutrino direction. The angle α between the lepton and the neutrino direction can be approximated by [Ne04]:

$$\beta \approx \frac{0.7^\circ}{(E_\nu/\mathrm{TeV})^{0.7}} \ . \tag{24}$$

Thus, the tracking of the lepton allows to reconstruct the initial direction of the neutrino. The behaviour of the three leptons is different. Electrons produce an electromagnetic cascade, muons and taus propagate straight forward depositing energy along their track. The lifetime of a tau $\tau_\tau = 0.29$ ps [PP04] is orders of magnitude shorter than the lifetime of the muon $\tau_\mu = 2.2$ μs [PP04]. A tau decays shortly after it is produced, while a muon can travel longer distance. For high energetic taus this distance is about 5 cm for 1 TeV and 50 m for 1 PeV. The tau decay is most often hadronic, such events are called "Double-Bang-Events" because of the two separate high energy cascades, one from the neutrino interaction and one from the tau decay. In ice, muons travel a typical distance of about 2.5 km at 1 TeV.
High energetic particles move through matter with almost vacuum light speed c_{vac} so they emit light due to the Cherenkov-effect. For a track a light cone is produced while for showers a nearly spherical wavefront is generated with a maximum of the amplitude in the forward direction.
By instrumenting a large detector volume with light sensitive modules it is possible to measure the Cherenkov photons. The arrival time at the modules allows tracking. Hence, the neutrino direction can be reconstructed.
Important for background rejection of muons produced by cosmic ray induced air showers is the direction of an event. Only the cross section for neutrinos is low enough that they can travel trough the earth. So events from this direction are neutrino events and are

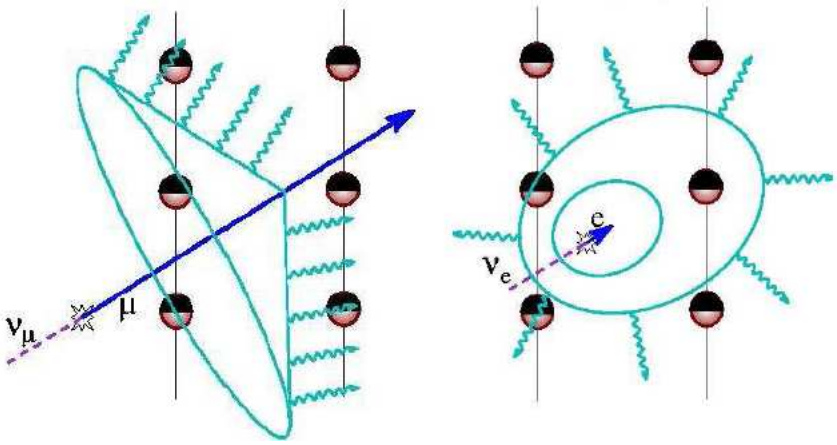

Figure 7: Track and cascade like events in the detector. Muon tracks produce tracks with a Cherenkov cone (left). Electrons induce cascades and spherical events are observed. (right)

called "up-going". At a few PeV the earth becomes opaque for neutrinos. At these energies it is possible to change the field of view upward because the background of down-going muons is smaller due to the steeper energy spectrum.

A big detector is required for the neutrino detection due to the small cross section and the steep power spectrum. Usually natural materials are used for these detectors. These materials are ice or water. Both provide good transmission properties for photons. (For ice the absorption length is about 100 m and for sea water it is about 50 m.)
For the instrumentation a compromise between the detector size and the distance between the optical sensors must be found. Larger volumes increase the number of observed neutrinos interactions while narrow distances provide a better reconstruction especially for lower energetic neutrinos. Typical distances are in the order of some ten meters.

3.1.1 Cherenkov Light

The Cherenkov-Effect occurs if a particle moves with a speed above the speed of light in the material.

$$v > c_{med} = \frac{c_{vak}}{n(\omega)} \,. \tag{25}$$

The critical energy for the Cherenkov effect is frequency dependent due to the wavelength dependence of the refraction index. A muon requires a total energy of about 160 MeV. A light cone is produced similar to a sound cone from a jet travelling with supersonic speed. This light cone is the constructive interference of infinite spherical waves originating from the track. The Cherenkov angle θ_c for the photons is (compare figure 8):

$$\cos(\theta_c) = \frac{1}{\beta n(\omega)} \,. \tag{26}$$

The index of refraction is connected to the phase velocity and thus it is connected to the observation angle. The propagation speed for the photon is given by the group velocity

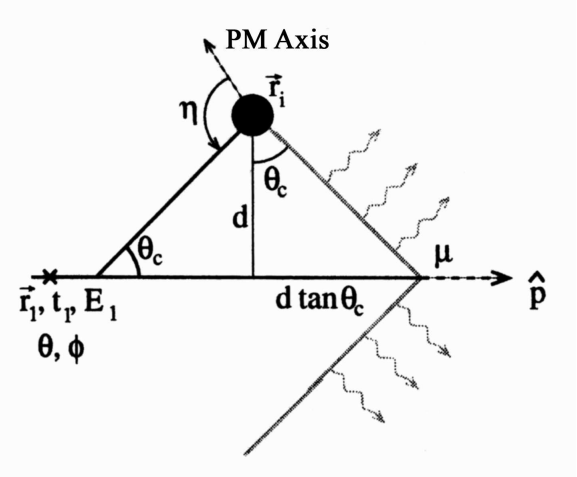

Figure 8: Cherenkov cone of a particle in the detector with a parametrisation for the track and the optical module.

in the material.
The photons from the Cherenkov effect form a cone with the half opening angle [MS53]:

$$\alpha = \pi - \theta_c = cot^{-1}\left(\sqrt{\beta^2 n^2 - 1} + \frac{dn}{d\omega}\frac{n\omega\beta^2}{\sqrt{\beta^2 n^2 - 1}}\right) . \tag{27}$$

For a constant index of refraction the propagation direction of the photons is perpendicular to the cone front.
The number of photons emitted per track length dx is given by the Frank-Tamm-Formula [Ja96].

$$\frac{d^2N}{dxd\lambda} = \frac{2\pi\alpha_f}{\lambda^2}\left(1 - \frac{1}{\beta^2 n^2}\right) \tag{28}$$

α_f is the fine structure constant. With the assumption of a wavelength between 300 nm and 500 nm about 250 photons/cm are emitted under a Cherenkov angle of 41° in ice. The corresponding energy loss is:

$$\frac{dE_\mu}{dx} = \frac{dN}{dx} < E_\gamma >= \frac{dN}{dx}\frac{hc_{vac}}{< \lambda >} \approx 850\frac{eV}{cm} . \tag{29}$$

The emission of Cherenkov photons is not the dominant process for the energy loss of the muon. For muons the main processes are instead: ionisation, bremsstrahlung, photonuclear reactions and pair production (chapter 3.1.2). In these processes other charged particles occur, they have the same flight direction due to the large Lorentz boost. They also emit Cherenkov light.

3.1.2 Muon Energy Loss

The different processes of energy loss for muons will be briefly discussed in the following:

Ionisation: The energy of the muon E_{kin} is large compared to the mean energy required to ionise an atom I. The muon knocks an electron out of the atomic shell. The energy loss of the muon is then described by the Bethe-Bloch-Formula [PP04]:

$$\frac{dE_\mu}{dx} \propto \frac{Z}{A}\frac{1}{\beta^2}\left(\frac{1}{2}\ln\left(\frac{2m_e c^2\beta^2\gamma^2 T_{max}}{I^2}\right) - \beta^2 - \frac{\delta}{2}\right) . \tag{30}$$

Here, T_{max} is the maximum kinetic energy which can be imparted to a free electron in a single collision and δ is a density effect correction.

Bremsstrahlung: In the electromagnetic field of the nucleus the muon is deflected and emits bremsstrahlung photons.

Pair production: The energy of the muons is high enough to produce virtual photons for pair production. The minimum energy is about 1 MeV for electron positron pairs and about 210 MeV for μ^- μ^+ pairs. Here also a third charged particle must exist to take the recoil.

Photo nuclear reactions: Similar to the ionisation a particle from the nucleus can be knocked out. These are rare interactions compared to pair production or Bremsstrahlung. Energy is transferred to the nucleus by a virtual photon. Usually the core is destroyed.

The total energy loss of a high energetic muon in matter can be approximated by [PP04]:

$$\frac{dE_\nu}{dx} = a + bE_\nu \qquad a \approx 2 \text{ MeV/cm} \qquad b \approx 3.6 \cdot 10^{-6}/\text{cm} . \tag{31}$$

In first order the values of a and b are independent of the energy. The constant part of the energy loss is the result of ionisation. Below a critical energy of about $E_\nu \approx 600$ GeV the ionisation is dominant while above pair production and photonuclear reactions dominate. Here the stochastic character has to be taken into account, while the ionisation can be treated as continuous energy loss.

3.2 The AMANDA Detector

The "Antarctic Muon And Neutrino Detection Array" (AMANDA) is installed in the ice near to the geographic South Pole. Between the year 1995 and 2000, 678 optical modules were deployed. An optical module consists of a photomultiplier for the light detection in a pressure housing. The modules are attached to cables in vertical holes in the ice. These holes are melted with a special drill. One cable including all attached modules is called a "string". Most optical modules are placed at a depth between about 1500 m to 2000 m.
A test installation called "AMANDA-A" in shallow depth was deployed in 1993. Then the initial installation of the first part of the detector finished in 1996 was called "AMANDA-B4". These are the first four strings in the centre of the detector. One string is placed in the centre and the other three are placed on a circle of ~ 30 m around it. The first upgrade is a next ring (radius ~ 60 m) with six strings commissioned in 1997. Together they are called "AMANDA-B10". A third ring completes the detector with nine additional strings

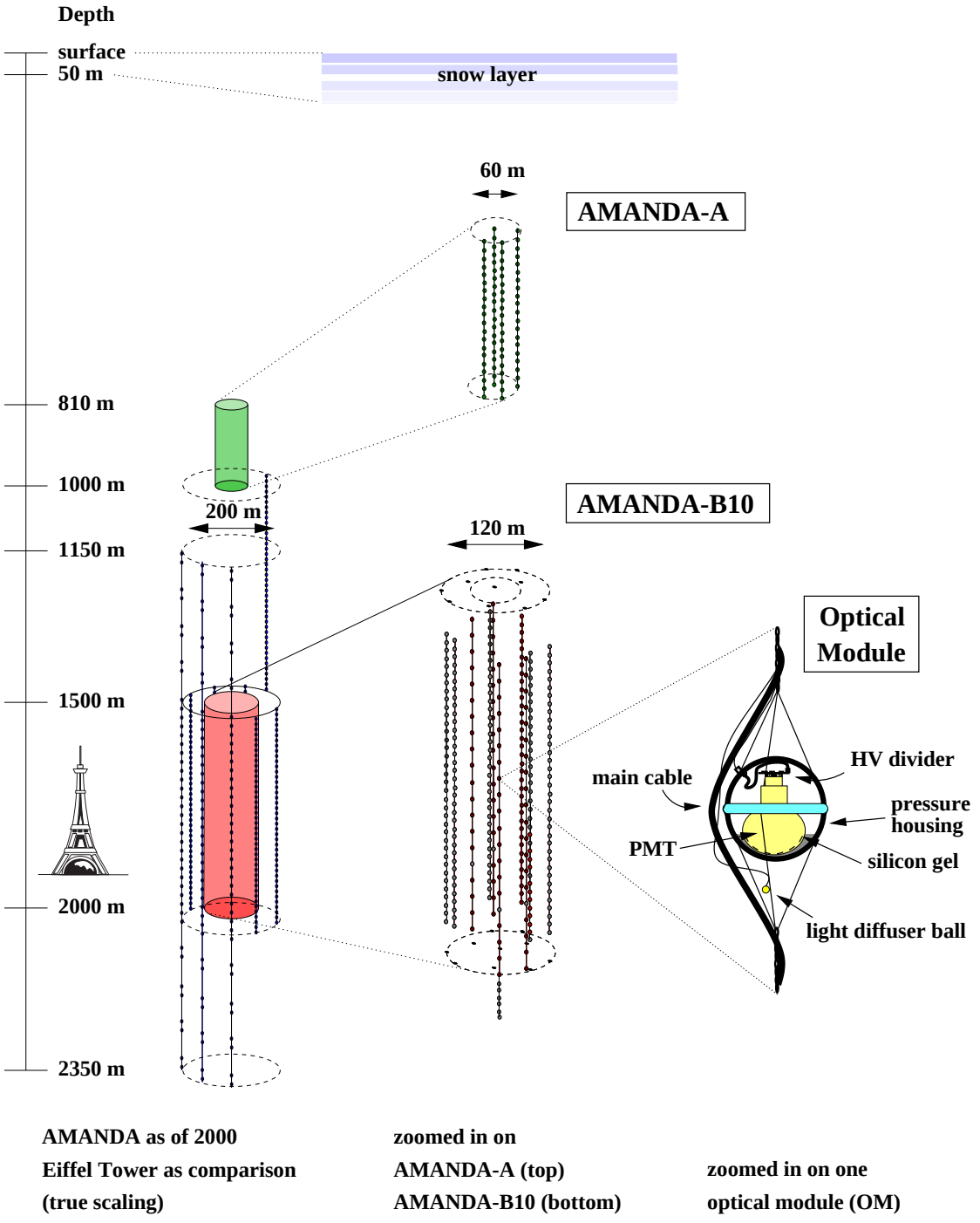

Figure 9: The layout of the AMANDA-II detector. The main part of the detector is between 1500 m and 2000 m. Strings with optical modules placed in the ice. The inner part was deployed first and is called AMANDA-B10. AMANDA-A is an older test installation from 1993 at shallow depth. The dots represent optical modules. A sketch of an optical module is drawn for illustration.

at a radius of $\sim$ 100 m. This configuration is taking data since 2000 and is referred to as "AMANDA-II". Figure 9 shows an overview of the detector.
The optical modules are arranged in a cylindrical form with a diameter of about 200 m and a height of 500 m. This corresponds to an enclosed detector volume of about 0.015 km^3. The vertical distance between two optical modules is between 10 m and 20 m. Each optical module contains a hemispherical photo multiplier (PMT) with a diameter of 8 inch[4] of the photocathode. A PMT is coupled with an optical gel to the glass of the surrounding sphere. The sensitive wavelength region is from green to ultra violet light.
The technical details of the modules and strings depend on the date of deployment. The data of each PMT is transmitted to the surface for processing. The single hit-rate is between 0.3 kHz and 1.5 kHz. Only a small fraction is from muon tracks. Data from a 32 μs interval is stored if 24 PMTs show a hit within a time window of 2.5 μs. This is called a multiplicity trigger. With the given distance of the optical modules this results in a lower energy threshold of some 10 GeV. Additional triggers are produced by the air-shower experiment SPASE-2. It is located near the AMANDA detector on the surface of the ice.
The data from each trigger is moved to one event with the information about the photon arrival time (LE[5]) and the time over threshold (TOT). The LE is defined by the time when the amplitude of the PMT signal rises above the threshold. This is stored up to eight times per event and per optical module. Additionally the maximum peak height around the trigger (2 μs before and 7.8 μs after) is stored. These are called ADC[6]-values. The storage of the data takes about 2.2 ms. During this time AMANDA cannot measure new data. With a typical trigger rate of 150 Hz this leads to a dead time fraction of about 17%.
From the beginning of the year 2003 waveform-recorders (TWR[7]) are additionally used for almost all optical modules. They allow the storage of the full PMT signal. This is important to increase the acceptance at high energies.

AMANDA-II is the largest completed neutrino telescope on Earth. The successor experiment IceCube will have a 50 times larger detector volume of 1 km^3. The first strings are already deployed in the ice. Compared to the other neutrino telescopes in water, ice has the advantage of fixed positions of the optical modules and a static installation platform. Also the solid state is a advantage compared to other telescopes; no permanent pressure on the optical modules exist. Additionally, the noise by ^{4}0K decay in the PMTs is low because the ice contains no ^{40}K. A disadvantages is that it is not possible to repair the modules in the ice.
A further difference are the optical properties of ice and water and that AMANDA observes the full northern sky with constant exposure.

3.2.1 The Antarctic Ice

An important aspect of the detector are the optical properties of the ice around the optical modules which affect the propagation of the Cherenkov light.

[4] 1 inch $\approx$ 2.54 cm
[5] LE = Leading Edge
[6] ADC = Analog to Digital Converter
[7] TWR = Transient Waveform Recorder

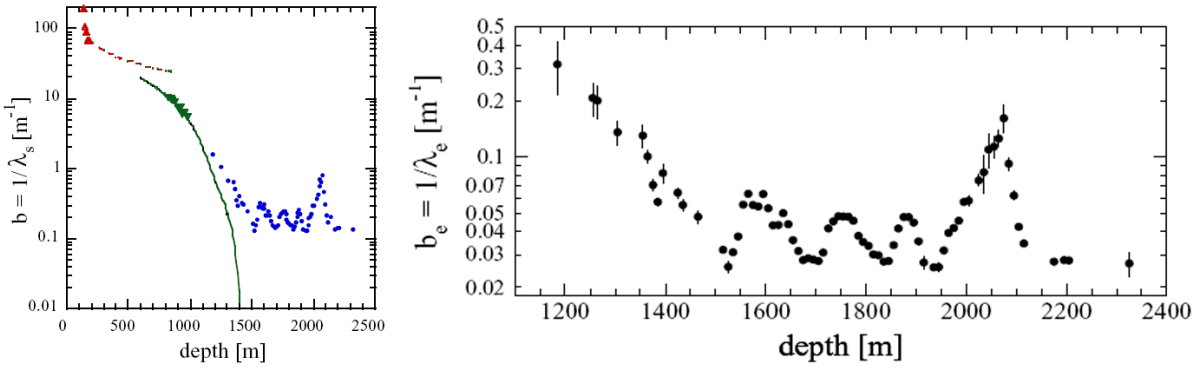

Figure 10: Left: Scattering coefficient as function of depth. Right: Scattering coefficient between 1200m and 2400m depth in more details. [PW00]

The ice properties are correlated to the time when the ice was formed. These properties of the different ice layers depend on the climatic situation at that time (different amounts of acids, salts, minerals and dust inclusions). In the South Pole ice there is only a small amount of inclusions compared to water, but they still change the scattering and absorption appreciably. Figure 10 shows the scattering length as function of the depth.
At varying depth different effects dominate. Above about 1000 m icebound gas bubbles increase the scattering; below there is less gas. Here, the properties are dominated by embedded solid materials. Four peaks corresponding to dust layers are seen (figure 10). Typical sizes of the absorption length λ_{abs} and the scattering length λ_{scat} in ice are:

$$\lambda_{abs} = 90 \text{ m} - 120 \text{ m} \qquad \lambda_{scat} \sim 25 \text{ m} \, . \tag{32}$$

These values determine the detector size given above.
The water in the holes from deployment re-freeze with special properties. Gas bubbles and impurities from drilling raise scattering. More information about the ice properties can be found in [PW00][Wo99].

3.2.2 Calibration

The number of calibration parameters is small: the position of the optical modules, time and height of the PMT signal.
These parameters are calibrated by in situ light sources. The light produced by these sources is observed in the modules.

The arrival time t_a differs from the measured time t_{LE}. The propagation of the signal in the cables and the PMTs is denoted to t_0. Also the time to reach the detection threshold has to be considered. The delays are measured with a surface laser. The time a light pulse needs to reach the modules can be calculated taking into account scattering. The difference between this and the detection time in the control station is an estimation for the delay. The time until the threshold is reached depends on the maximum hight of the pulse A. All together the arrival time t_a is:

$$t_a = t_{LE} - \frac{\alpha}{\sqrt{A}} - t_0 \, . \tag{33}$$

t_0 and α are determined for each module. The achieved precision is better than 7 ns for t_0 and 30% for α. [Bi00]
The geometric calibration is done by the relative time differences of the various light pulses in the optical modules. In a global fit for all modules a precision of 1 m in the position of each optical module is achieved. The absolute precision of the detector orientation with respect to sky coordinates is better than 0.2°. This has been verified by cross calibration with the air shower experiment SPASE-2.
In the range of interest the PMT signal increases linear with the light signal. Most pulses correspond to single photons. Their amplitudes are used to determine the proportionality constant between photon number and pulse height (taking the background into account). The precision is determined by the width of a fit with a Gaussian. It is about 35%. [Bi01]

3.3 From the Raw Data to Final Directions

In the previous chapters the raw data taken with the AMANDA-II detector is described. For this data an event selection has to be applied to reduce background events. Afterwards a track reconstruction is performed. Only muon neutrinos are used for the analysis.
The detector samples data with a rate of about 100 Hz. Only 15 events per day are muon-neutrinos, the major part is from muons produced in the atmosphere.
By fast pre-filtering of the neutrino events from the atmospheric events (chapter 3.3.3) the data is reduced. A full track reconstruction is done for the smaller data sample (chapter 3.3.4). This is done by a maximum likelihood method. Finally quality parameters are defined to separate the remaining background from the data. (chapter 3.3.5).

3.3.1 Different Background Types

The detector records many different signals which are not all induced by leptons from neutrinos. The huge number of atmospheric muons induces many different types of background events. These signals can be separated in different classes:

- **Well reconstructed, down going muons:** This is the biggest part of the background. Filtering is performed by a zenith cut.
- **Muon bundles:** Air showers also produce bundles of muons. They travel together through the detector producing an ambiguous signal which can be mis-interpreted as up-going neutrino.
- **Cascades:** Catastrophic energy losses (e.g. pair production) of high energetic muons in the ice lead to cascade like light depositions. They can mimic an "up-going" muon signature.
- **Stopping muons:** No track through the full detector is produced. The reconstruction is more challenging. Especially horizontal events can be mis-reconstructed as up-going.
- **Scattering layers:** The scattering rate in the polar ice has a layered structure. An up-going event can be imitated by bright events particularly when the light traverses layers with a high scattering rate.

- **Corner Clippers:** A muon travels diagonal below the detector. The Cherenkov light reaches the detector from below and mimics a "up-going" event.
- **Uncorrelated coincident muons:** During one event two muons from different showers in the atmosphere deposit light in the detector. An "up-going" event is reconstructed if the light deposition of one muon in the upper detector part is taking place later.
- **Electronic artefacts:** Crosstalk between the optical modules of one string creates electronic artefacts. These signals should be excluded from the reconstruction.

All these effects have to be taken into account in the reconstruction and event selection.

3.3.2 Hit-Cleaning

Before calculating a track hypothesis a hit-cleaning is done. For the reconstruction only hits corresponding to the track should be used. Hits from PMT noise, cross talk or other sources are removed. Optical modules with too low ("dead"), too high or variable noise level are removed. A stable noise level indicates a proper functionality of a module.
Additionally hits are removed from events by the following selection:

1 **Isolated hits:** A hit is isolated if no other hits are found in a distance of $60-100$ m and a time difference of ± 300 ns to ± 600 ns. Such a hit is expected to be produced by noise and is discarded.

2 Hits with a **too large time difference:** Hits with -2 μs to $+4.5$ μs around the trigger are selected. Other hits are expected to be noise or have no information due to after-pulsing.

3 **Hits from crosstalk:** A comparison between the ADC-values and the length of the pulse (TOT) is used. Large ADC-values with short pulses are a clear indication for crosstalk due to the dispersive widening of the signal in the cable. These hits are removed.

These criteria depend on the individual event configuration. Modules with a skipped hit in one event can contribute to other events.

3.3.3 Initial Track Reconstruction

For the initial selection of "up-going" event candidates and for the full track reconstruction a first track estimation is required.
For the calculation of this initial track several methods are available. The "Direct Walk" and the "JAMS[8]" method are discussed here, although other first guess track reconstructions based on a "line-fit" or a "dipole algorithm" exist. They are not used for the data sample on which this analysis is based on and thus they are not discussed here.

Direct Walk [St00]:

[8] JAMS = Just Another Muon Search

This method has four steps. First a search for track segments is performed. A track segment are two optical modules with a distance greater than 50 m and a time difference $\Delta t < d/c_{vac} + 30$ ns for the hits. The track segment is the connection line between these two modules.
The number of associated hits $N_{ass,i}$ is determined for each track segment i. Therefore, for each hit the time residuum t_{res} is calculated. This is the difference between the expected time from geometry t_{geo} and the observed time t_{hit}.

$$t_{res} = t_{hit} - t_{geo} \qquad \text{with} \qquad t_{geo} \equiv t_1 + \frac{\hat{p}(\vec{r}_i - \vec{r}_1) + d\tan\theta_c}{c_{vac}} \; . \tag{34}$$

t_{res} is the delay from scattering. The other parameters describe the track and the position of the optical module. They are given in figure 8. $\hat{p}$ is the track direction, t_1 is the track time and $\vec{r}_1$ is the position of the track. $\vec{r}_i$ is the position of the optical module and θ_c is the Cherenkov angle. Together with the perpendicular distance to the track segment d, t_{res} is used as discriminant. A hit is associated with a track segment i if:

$$-30 \text{ ns} < t_{res} < 300 \text{ ns} \; , \tag{35}$$

$$d < 25 \text{ m}(t_{res}/\text{ns} + 30)^{1/4} \; . \tag{36}$$

For each module j the projection of its position to the track is calculated. This is called "lever arm" L_j. The mean "lever" quantifies the length of the track in the detector. The track segments fulfilling the requirements below are chosen as track candidates.

$$N_{ass,i} > 9 \qquad \sigma_{L,i} \geq 29m \qquad \text{with} \qquad \sigma_{L,i} \equiv \sqrt{\frac{1}{N_{ass,i}} \sum_j (L_j - < L >)^2} \tag{37}$$

In general, more than one candidate exists and a further selection is required. First the two values $N_{ass,i}$ and $\sigma_{L,i}$ are combined in one quality parameter.

$$Q_i = \min\left(N_{ass,i}, \frac{0.3}{\text{m}}\sigma_{L,i} + 7\right) \qquad Q_{max} = \max Q_i \tag{38}$$

Candidates require a quality Q larger 70% of Q_{max}. Finally; for each track segment the number of segments with a difference less than 15° in the direction is counted. The ensemble with the highest number is chosen. The vertex of the central track segment and the average of all directions of the ensemble is the first guess track.

JAMS [St02]:
JAMS reconstructs the track by a complementary technique. Here, a search for clusters in time and transverse position to specific cones is performed. For a hit the signals from the PMTs cluster in both criteria.
To perform this search, the hit topologies are investigated in different directions. For this, 26 equally distributed cones with a opening angle of ±25° are used. In these cones a distance is given by:

$$(\Delta_t c_{vac}, X, Y), \qquad \Delta_t = t_{hit} - t_0 - l/c_{vac} \; . \tag{39}$$

X, Y are the transverse coordinates to the cone direction and Δ_t is the time difference between a hit and the reference hit (t_0). For each hit the number of close neighbour hits is counted, called multiplicity $m_{hit,i}$. A hit with a distance $|(\Delta_t c_{vac}, X, Y)| < 70$ m is "close". The hit with the largest multiplicity $m_{hit,i}$ is chosen. The average over $(\Delta_t c_{vac}, X, Y)$ for all neighbours is used as start value for the reconstruction together with the cone direction. The reconstructed direction of the muon deviates from the original direction in 94% less than 30° for simulated data.

Both methods provide good first estimations for the track direction but do not achieve a high precision.

3.3.4 Maximum Likelihood Reconstruction

A more precise way of reconstructing a muon track is a maximum likelihood method. Here, the probability to obtain the measured hits for a track is maximised for different track hypotheses. This takes more computing time, so it is done for the smaller data sample of "up-going" candidates selected.
With a probability density function $p(x_i|a)$ for measuring the observed value x_i for a fixed track a the Likelihood function can be written as:

$$\mathcal{L}(x|a) = \prod_i p(x_i|a) \; . \tag{40}$$

x is the full experimental information (the ensemble of all x_i) and the x_i are assumed as independent.
Here, a track is specified by the vertex, the time, the direction and the energy. The experimental data x_i are times $\vec{T}_{LE,i}$, durations $\vec{T}_{TOT,i}$ and the peak amplitudes $\vec{A}_i$ for each module i. (Each module stores up to eight sets of time, duration and amplitude per event.) For the simplest likelihood only the arrival times are used. The time likelihood function can be written as:

$$\mathcal{L}_{time} = \prod_{i=1}^{N_{hits}} P(t_{res,i}|a) \; . \tag{41}$$

The probability density for a time likelihood depends on t_{res} (defined by equation (34)). In the ideal case the distribution $p(t_{res}|a)$ is a delta function. This is different in a real experiment. The distribution is broadened and distorted by the PMT jitter, the PMT noise and by scattering in the ice. Additionally, the orientation between the PMT and the muon track must be considered due to a non uniform PMT response. A PMT looking away from the track can observe only scattered photons with a larger time residual t_{res} than direct photons.
The distribution of the time differences can be described approximately by a so called Pandel [Pa96] function.

$$p(t_{res}, d) = \frac{1}{N(d)\Gamma(d/\lambda)t_{res}} \left(\frac{t_{res}}{\tau}\right)^{d/\lambda} \exp\left(t_{res}\left(\frac{1}{\tau} + \frac{c_{ice}}{\lambda_a}\right) + \frac{d}{\lambda_a}\right) \tag{42}$$

$$N(d) = e^{-d/\lambda_a}\left(1 + \frac{\tau c_{med}}{\lambda_a}\right)^{-d/\lambda} \tag{43}$$

$N(d)$ is a normalisation constant, λ_a is the attenuation length in ice, λ and τ are free parameters and Γ is the Gamma function. The free parameters of the Pandel function are determined by simulations including the ice model. The used values are effective values for the corresponding parameters. Also the distance d is replaced by an effective distance d_{eff}.

$$\tau = 557 \text{ ns} \qquad d_{eff} = a_0 + a_1 d \qquad \lambda = 33.3 \text{ m} \qquad \lambda_a = 98 \text{ m} \tag{44}$$

$$a_1 = 0.84 \qquad a_0 = 3.1 \text{ m} - 3.9 \text{ m}\cos(\eta) + 4.6 \text{ m}\cos^2(\eta) \tag{45}$$

η is the angle between the orientation of the Cherenkov-cone and the orientation of the PMT (see figure 8). The Pandel function is not defined for negative t_{res}, has a pole at $t_{res} = 0$ (for small distances d) and does not include the PMT jitter. A convolution with a Gaussian solves this but takes more computing time. Instead a composed function is used: A (half) Gaussian with width σ_g for $t_{res} < 0$ and the Pandel function for $t_{res} \geq \sqrt{2\pi}\sigma_g$. The parts are connected with a spline (3rd order polynomial). This is a meaningful definition since the jitter is relevant for small t_{res}. Good reconstructions are achieved for $\sigma_g = 10 - 20$ ns.
Additionally a "hit likelihood", a "Amplitude likelihood" and a "Zenith weighted (Bayesian) likelihood"[Ah04] can be used. They are not used to filter the 4-year-sample and they are not discussed here. A description is in [Ah04].

3.3.5 Quality Parameters

Quality parameters are defined to clean the data from background events (chapter 3.3.1), additionally to the zenith angle cut. They are related to information in the detector that is not used or not fully used by the reconstruction.

- The **number of direct hits** : $N_{dir}(t_1, t_2)$. A direct hit has a small time residual. Good choices are $-15 \text{ ns} \simeq t_1 < t_{res} < t_2 = 25 - 150$ ns. These photons provide the best information about the track. A large number of N_{dir} indicates a high quality information.
- The **length of the event** L: The length of an event is the biggest difference of two projections of the position of the optical modules on the track. A large length indicates a long track in the detector. This value is especially useful to exclude corner clippers, stopping muons and cascades. The length can be calculated using direct hits, only. Obviously, the length of the event depends on the chosen range of t_{res}.
- The **absolute value of the likelihood** : The likelihood parameter is:

  $$L = -\log(\mathcal{L})/N_{free} \, . \tag{46}$$

  The degrees of freedom are $N_{free} = N_{hit} - 5$ for a track reconstruction. Smaller values for L correspond to higher qualities.
- **Comparing likelihood parameters** for different reconstructions: High probabilities for a cascade reconstruction compared to the track reconstruction imply other event interpretations. It is not sure that the event is generated by an "up-going" neutrino.

- The **spacial distribution of the hits** is not included in the reconstruction. An equal distribution of the hits along the muon track fits better to the approximation of a constant light emission than a cluster at the end. This is described by the **smoothness parameter** S. A simple definition is:

$$S = \max(S_j) \qquad \text{with} \qquad S_j = (j-1)/(N-1) - l_j/l_N \; . \tag{47}$$

  l_j is the distance between the points of closest approach of the reconstructed track to the first and the j^{th} module. The hits are ordered by the position of the projection of their position to the track. N is the total number of hits. Small absolute values of S correspond to smooth distributions. Values close to ± 1 describe clustered events.

- For interesting events in AMANDA more than one reconstruction algorithm is performed. Each reconstruction provides a flight direction $\vec{e}_i$. **Comparing** these **directions** for several reconstructions is a good consistency check. The following value is defined:

$$\Psi_w = \left(\sum_i [\arccos(\vec{e}_i \vec{E})]^w \right)^{1/w} \; . \tag{48}$$

  E is the mean direction from all reconstructions. Ψ_1 and Ψ_2 are used as discriminants. These are good discriminants against horizontal muons and wide muon bundles.

These are the most general quality parameters. Others related to some of the first guess methods or to the intrinsic stability of the observed hits are available, too. For example, in one approach the width of a minimum of $-\log(\mathcal{L})$ is estimated by a parabola fit and another approach splits the data into two sup samples. The reconstruction is than done separately and the results are compared.
For each analysis the used quality parameters must be chosen separately because different criteria can be important. The selection for this analysis is presented in the next chapter.

3.3.6 The 4-Year-Sample

The data sample for this analysis is based on the AMANDA-II data of the years 2000-2003. The lifetime of the detector is 807 days. Each year of the data is filtered individually by the same procedure. Afterwards they are combined to one data sample. Differences in the procedure for the different years concern the lists of operating optical modules, the calibration constants, the crosstalk cleaning constants and the TOT ranges. Finally events from stable detector periods are selected. These are evaluated for each year individually.
The filtering procedure is shown in table 2. Hit-cleaning is done in the first level. Afterwards a first track estimation by the "Direct Walk" method is used to remove the down-going events. ($\theta < 70°$). A second first guess reconstruction is made (JAMS). Now all events below 80° are discarded. In the second level cross talk is removed and a reconstruction by the Pandel likelihood is done. Again all events below 80° are removed. The third filter level includes a smoothness calculation, a paraboloid fit and a Bayesian Likelihood Fit [Ah04].
This procedure delivers a sample of 3369 events 40 of those are below the horizon. All events in the sample are considered to be neutrino events. Figure 11 shows a sky map

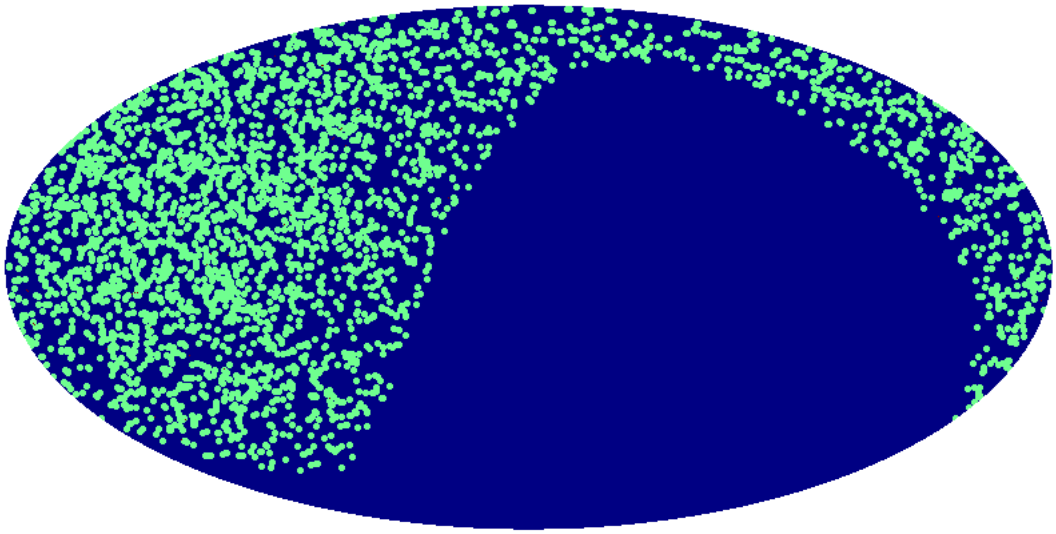

Figure 11: Map of the detected neutrino events in galactic coordinates with the galactic centre in the middle. Each dot corresponds to one neutrino. All events ($N_{tot} = 3329$) are on the northern hemisphere.

of these events. The fraction of mis-reconstructed events from background is expected to be less than 5%. This background is treated separately in chapter 8. More information about the filtering and the data sample can be found in [IC05]

3.4 The Monte Carlo Data

For the interpretation of the measured data, simulations are important. They describe the detector response and the expected fluxes from different sources.
In the following the simulation for the AMANDA-II detector is described. This is performed by the programs:

1 NUSIM for event generation

2 MMC for muon propagation

3 PTD for photon propagation depending on the ice model (MAM)

4 AMASIM for the detector response

The first step of the simulation is the event generation. For this purpose NUSIM[9] [Hi96] was developed by the AMANDA collaboration. Neutrinos with an zenith angle $80° < \theta < 180°$ are generated. These neutrinos are forced to propagate through the earth and to interact near the detector. Statistical weights are included according to the probability of these events. These constraints speed up the simulation.
The propagation through the earth and the interaction cross section for the neutrinos are taken into account. Not included are neutrino oscillations.

[9]NUSIM: NeUtrino SIMulation

Level	Filtering/ Fit
1	Hit and optical module cleaning
	Low TOT/amplitude filter
	Direct walk Reconstruction
	JAMS Reconstruction
2	X-talk cleaning
	Pandel Likelihood Fit (JAMS seeded)
3	Smoothness calculation
	Paraboloid Fit
	Bayesian Likelihood Fit (Pandel seeded)
	Flare Checker

Table 2: Filtering steps for the 4-year-sample

The simulation is independent of the initial sky distribution of the neutrinos and the same simulated data can be used for different energy spectra and distributions by re-weighting.

After the interaction of the neutrino a muon is propagated through the detector. The processes of energy loss are described in chapter 3.1.2. The statistical character of the different processes are taken into account. In the AMANDA collaboration the package MMC[10] [CR01] has been developed for this part.

The muons produce photons by the Cherenkov-effect. These photons are detected by the PMTs of the detector. The propagation of the photons in the ice is simulated with a tool named PTD[11] [Ka99]. The wavelength dependencies and the changed ice properties around a PMT due to re-freezing and dust layers are included.
In the simulation the local properties of the ice around the detecting module are used as reference. The vertical properties of the ice on the way is ignored. It is better than an homogenous ice model but still does not include the whole information about the ice. The parameters of the ice are taken from the MAM[12] Ice-Model [Wo03].
The simulation creates a table with the statistical distributions of all data. These values depend on the distance and the relative orientation between the PMT and the photon direction. The optical module, the deposited energy and the arrival time are taken into account.

Finally the detector response is simulated with a program developed by the AMANDA collaboration, named AMASIM[13] [Hu99]. The probability for a hit in an optical module is determined depending on the photon propagation and the ice model. It depends on the sensitivity of the PMT and the relative direction of the photon and the PMT. For a signal the individual gains, the corresponding pulse shapes, the data transport and the procedures in the surface electronics are simulated.

[10] MMC: Muon-Monte-Carlo
[11] PTD: Photon Transport and Detection
[12] MAM: Muon Absorption Model
[13] AMASIM = AMAnda SIMulation

A precise information about the system components is required for an accurate simulation. PMTs and high voltage supplies are devices, with time dependent failures. "Dead" channels simply can be skipped while "hyperactive" channels must be taken into account.

After the event generation these events are analysed in the same way as the measured data. This is described in chapter 3.3.6. After all selections the Monte Carlo data used for this analysis has 821339 neutrino events with corresponding weights w_i. For the simulation the number of equivalent events $\hat{n}$ is important. This is the number of unweighed events with the same relative error as the weighted events.

$$\hat{n} = \frac{(\sum w_i)^2}{\sum w_i^2} \tag{49}$$

In the Monte Carlo the number of events is proportional to E^{-1}. Steeper spectra have less equivalent events. The steepest spectrum used in this analysis is the spectrum of atmospheric neutrinos ($\gamma \sim 3.7$). Here the number of equivalent events is 21440. For the hypotheses with $\gamma = 2$ the number of equivalent events is above 100000. Compared to the number of events from the experiment $N_{tot} = 3329$ the statistics of the Monte Carlo is better by a factor 6.4 compared to the atmospheric spectrum of data. More information about the used Monte Carlo data can be found in [Ac06].
This Monte Carlo data is used for all simulations described in chapter 5.

4 Principle of the Analysis

The idea of this analysis is to compare the angular power spectrum of the measured data with the background expectation. This background is dominated by atmospheric neutrinos (chapter 2.3). For this background and different source hypotheses, sky distributions of source directions are simulated (chapter 5.1 and 5). The different hypotheses are given in chapter 2.4 and 5. Figure 12 shows a diagram with the analysis procedure. From the neutrino distributions the neutrino sky maps are generated including the acceptance and the angular smearing of the detector. Each hypothesis is simulated 1000 times in order to calculate the statistical variations. The measured data is also arranged to a sky-map. For each sky-map the multipole C_l moments (chapter 4.1) are calculated for $l = 1$ to 100.
In order to compare the different multipole spectra the quantity D^2 is defined by:

$$D^2 = \sum_{range} \frac{(< C_{l,atms} > - C_l)^2}{\sigma^2_{l,atms}} \; . \tag{50}$$

Here $< C_{l,atms} >$ is the mean multipole moment for the atmospheric neutrinos with the corresponding standard deviation $\sigma_{l,atms}$ (denoted by $< C_l >$ and σ_l in figure 12). C_l is the obtained spectrum of multipole moments from the simulations of the signal hypotheses or the measured spectrum, respectively. The range of the sum is determined by an optimisation of the sensitivity. Therefore, D^2 is used to compare the power spectra of the simulations to the mean and standard deviation of the atmospheric spectra with a range from 1 to l_{max} (described in chapter 6). The optimum range is determined by the probability for these $D^2(l_{max})$ to be not a fluctuation of the background. For these ranges the final D^2 values from the simulations and the measured multipole moments are calculated. The values from the simulations are combined to a confidence belt according to Feldman & Cousins "Unified Approach" [FC99] (chapter 6.5). This allows to determine a limit on the hypothesis for the D^2 of the experimental data.

4.1 The Angular Power Spectrum

The analysis of the angular power spectrum is based on the mathematical expansion of the distribution of the arrival directions in spherical harmonics. The spherical harmonics are a normalised orthogonal set of functions, defined by:

$$Y_l^m = \sqrt{\frac{2l+1}{4\pi}} \sqrt{\frac{(l-m)!}{(l+m)!}} P_l^m(\cos\theta) e^{-im\phi} \; . \tag{51}$$

l is the multipole index, m is the orientation of the multipole on the sphere, θ and ϕ correspond to spherical coordinates. Figure 13 shows the real- and imaginary-part of the spherical harmonics[14]. P_l^m are the extended Legendre Polynomes defined by:

$$P_l^m(x) = (-)^m (1-x^2)^{m/2} \frac{d^m}{dx^m} P_l(x) \; , \tag{52}$$

$$P_l^{-m}(x) = (-)^m \frac{(l-m)!}{(l+m)!} P_l^m(x) \; , \tag{53}$$

[14]The charts are created with an interactive online tool from [Ri06].

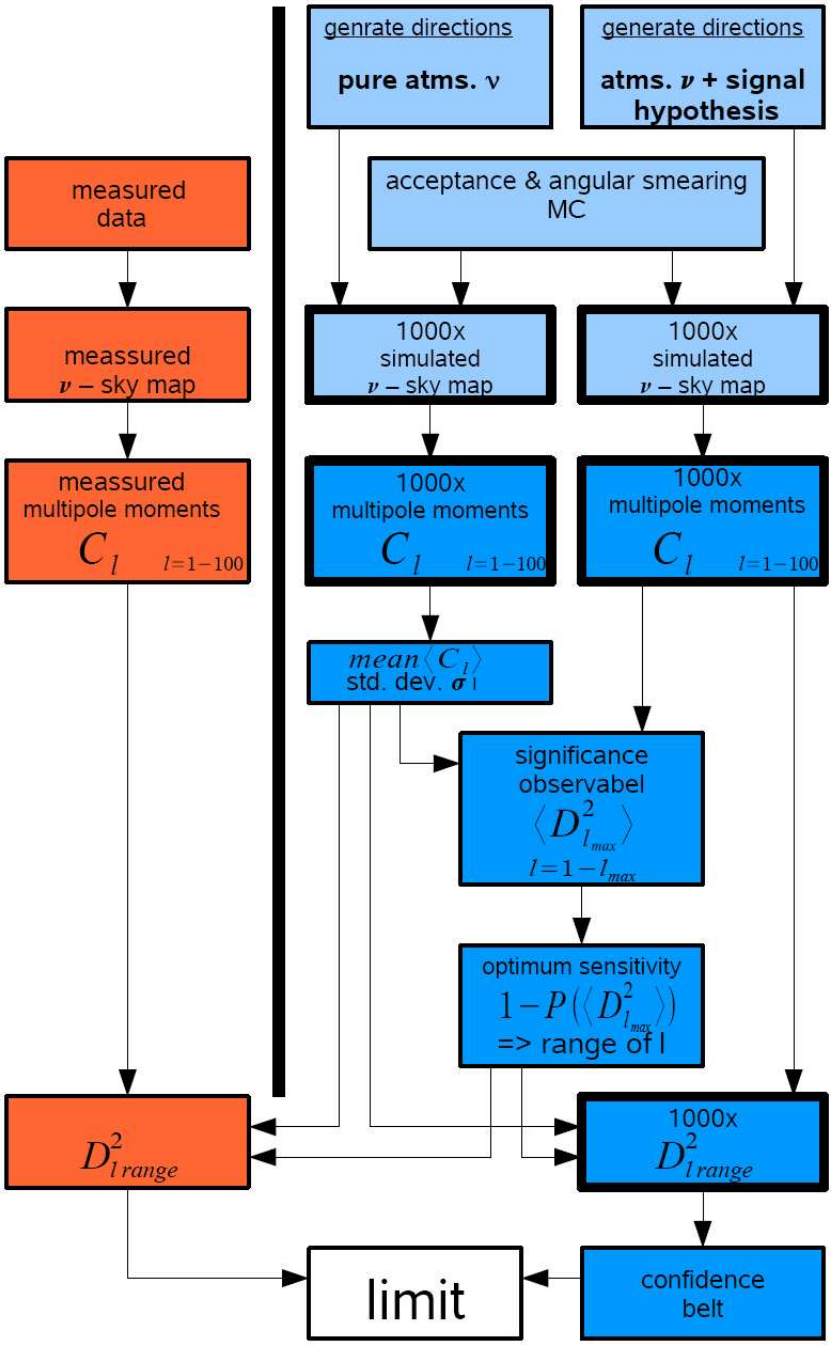

Figure 12: Scheme of the analysis. The red boxes (left) show the different steps for the measured data while the blue boxes (right) show the corresponding steps for the simulated data samples. Additionally the upright black line separates the measured and the simulated data. The light blue boxes (top left) separate the simulation steps from the analysis steps. Some boxes have a thick border to represent that this step is done 1000 times.

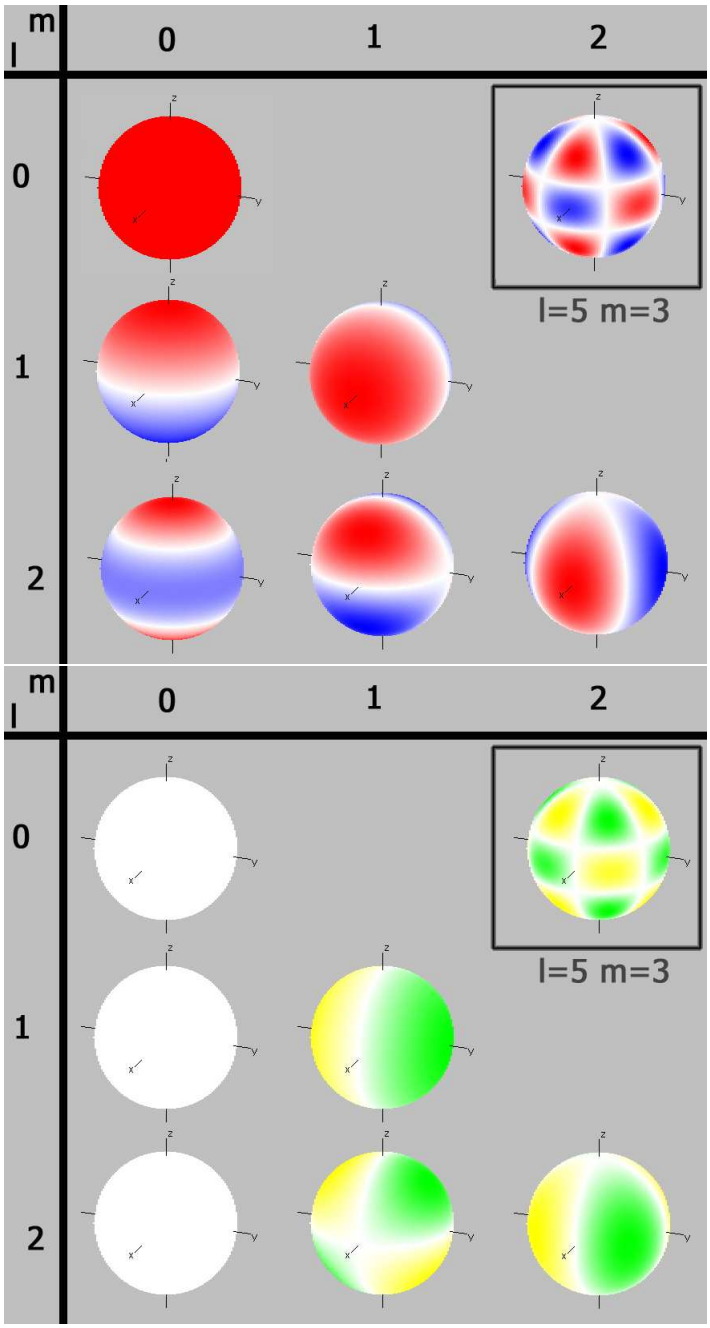

Figure 13: The spherical harmonics for small multipoles l and different orientations m. The top (blue, red) shows the real parts and the bottom (green, yellow) the imaginary parts of the Y_l^m. The charts are taken from [Ri06].

$$P_l(x) = 2^{-l} \sum_{j=0}^{[l/2]} (-)^j \frac{[2(l-j)]!}{j!(l-j)!(l-2j)} x^{l-2j} \ . \tag{54}$$

With the orthogonality relation:

$$\int_\Omega Y_l^m(\theta,\phi)\bar{Y}_{l'}^{m'}(\theta,\phi)d\Omega = \delta_{ll'}\delta_{mm'} \ . \tag{55}$$

It is possible to expand a function $f(\theta,\phi)$ (θ,ϕ corresponding to spherical coordinates) to spherical harmonics, if $\int |f(\theta,\phi)|^2 d\Omega < \infty$:

$$f(\theta,\phi) = \sum_{l=0}^{\infty} \sum_{m=-l}^{l} a_{lm} Y_l^m(\theta,\phi) \ , \tag{56}$$

$$a_{lm} = \int_\Omega f(\theta,\phi)\bar{Y}_l^m(\theta,\phi)d\Omega \ . \tag{57}$$

The multipole moments are defined as:

$$C_l = \frac{1}{2l+1} \sum_{m=-l}^{l} |a_{lm}|^2 \ . \tag{58}$$

Each C_l describes the strength of structures at a fixed angular scale. This angular scale is roughly approximated by:

$$\psi \approx \frac{180^\circ}{l} \ . \tag{59}$$

The ensemble of all $C_l(2l+1)$ is the angular power spectrum of the inserted function $f(\theta,\phi)$.

Solving the integrals in equation (57) is the main task when calculating the angular power spectrum. The integration is numerically difficult because the spherical harmonics oscillate strongly for large l. It is performed by the software "GLESP[15]" [Do05]; "GLESP" is discussed further in chapter 6.1.

4.2 Sky-Map for an Ensemble of Points

The data-sample contains discrete neutrino arrival directions and not a continuous map defined on the sphere (described by a function $f(\theta,\phi)$). However, this is required for the expansion in spherical harmonics.
A direction in the sky can be described by $\vec{\omega}_i = (\theta_i, \phi_i)$ in spherical coordinates. Such a direction is interpreted as point on an unit sphere. A meaningful map is:

$$f(\vec{\omega}) = \sum_{i=1}^{N_{tot}} b_i \delta(\vec{\omega} - \vec{\omega}_i) \ . \tag{60}$$

$\vec{\omega}$ is a point on the sphere and $\delta(\vec{\omega})$ is the 2 dimensional delta function on the half sphere ($\int \delta(\vec{\omega})d\Omega = 1$). The b_i are normalisation and weight factors for each neutrino direction.

[15] GLESP = Gauss Legendre Sky Pixelation

The angular resolution is not included into the sky-map. Instead it is taken into account in the simulations.
In this analysis a sky-map with equal weights is used i.e. $b_i = b$, $\forall i$. Note, that the angular acceptance of the detector is not taken into account here. The final sky-map is:

$$f(\vec{\omega}) = b \sum_{i=1}^{N_{tot}} \delta(\vec{\omega} - \vec{\omega}_i) \; . \tag{61}$$

b is fixed by the normalisation of $C_0 = |a_{00}|^2 = \pi$. The value for $b = \sqrt{\pi}/N_{tot}$. (Compare equation (57) and (58)).

4.3 Limitations by Statistics

The 4-year-sample consists of only $N_{tot} = 3329$ events in the northern hemisphere. This is a relatively small number for a multipole analysis. Thus, statistical effects have to be taken into account. For a rough estimation of the angular resolution the solid angle per neutrino direction on a half sphere is:

$$\Omega = \frac{2\pi}{N_{tot}} \approx 1.9 \cdot 10^{-3} \text{ sr} \; . \tag{62}$$

The mean angular distance of two neutrino directions is the opening angle *delta* of a cone corresponding this solid angle Ω:

$$\delta = 2\sqrt{\frac{\Omega}{\pi}} = 2\sqrt{\frac{2}{N_{tot}}} \approx 4.9 \cdot 10^{-2} \text{ rad} \hat{=} 2.8^\circ \; . \tag{63}$$

With equation (59) a maximum multipole index of $l_{max}^{angular} \approx 64$ is obtained. This is only a rough approximation of an upper limit because effects on smaller angular scales may still exist. (For example: groups of clustered neutrino directions would lead to effects on smaller scales.) This $l_{max}^{angular}$ is the size of the limit, above which the statistical uncertainties becomes too large to extract informations from the multipole moments.
Another effect limits the information of higher multipole moments. Each multipole moment C_l has $2l+1$ degrees of freedom (compare equation (58)). For the full expansion the degrees of freedom are:

$$dof = \sum_{l=0}^{l_{max}} (2l+1) = l_{max} \cdot (l_{max} + 2) + 1 \; . \tag{64}$$

The degrees of freedom should not exceed the number of neutrino directions. This restricts the maximum number of independent multipole moments:

$$.l_{max}^{dof} < \sqrt{N_{tot}} - 1 \approx 57. \tag{65}$$

Above l_{max}^{dof} the multipole moments C_l are correlated with the moments with $l < l_{max}^{dof}$. Only these multipole moments are used in the analysis.
The optimisation in chapter 6.4 shows that a maximum multipole moment $l_{max} < 40$ is meaningful. Which is sufficiently smaller than the limits calculated here.

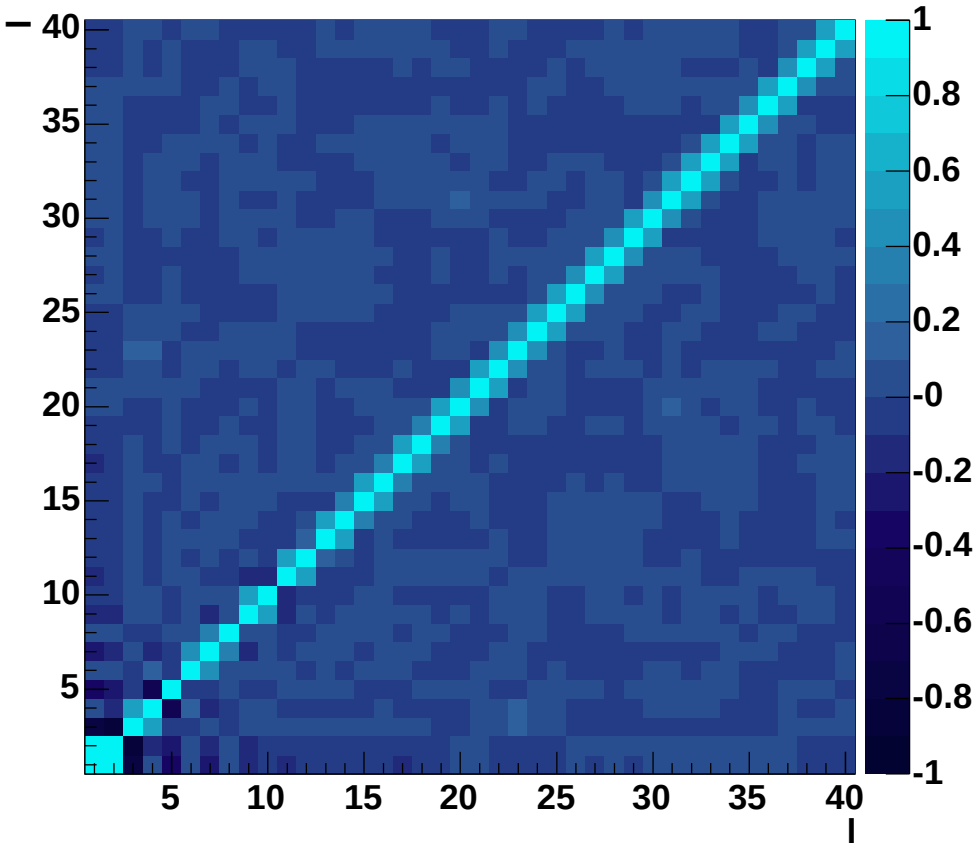

Figure 14: Correlation coefficients between the multi pole moments. The x-axis and the y-axis give the multipole index l. The colours indicates the values of the correlation coefficients.

4.4 Effects According to the Partial Sky Coverage

Effects according to the partial sky coverage and the zenith dependent detector acceptance have to be taken into account as well.

The AMANDA-II detector covers only the northern hemisphere. Correlations in the multipole moments occur because the spherical harmonics are not orthogonal on the half sphere, In particular when concerning the non-isotropic detector acceptance and the angular distribution of atmospheric neutrinos. The correlation coefficient for the first 40 multipole moments are shown in figure 14. They are calculated from the 1000 atmospheric simulations. The coefficients for the signal hypotheses are similar because all neutrino distributions are dominated by atmospheric neutrinos.
Mainly weak next neighbour correlations (correlation coefficient 0.5) are observed. This is not surprising, since Y_l^m and Y_{l+2}^m are orthogonal on a half sphere. This can be seen from the equations 51 to 55. At small multipole moments the non-uniform acceptance induces

additional (anti-) correlations. Obviously the correlations are small but will be considered in the later analysis procedure.

The second important effect is the dependence of the multipole moments on the non uniform detector acceptance. The "true" unbiased multipole moments can be obtained by unfolding:

$$C_l^{obs} = \sum_{k=0}^{\infty} M_l^k C_k^{true} \ . \tag{66}$$

C_l^{obs} are the multipole moments calculated from the map of the partial sky, C_k^{true} are the multipole moments of the full sky and M is the folding matrix. The C_l^{true} also extend the structures from the half to the full sphere. M depends only on the sky coverage and the detector acceptance [D204]:

$$M_l^k = \frac{2k+1}{4\pi} \sum_m (2m+1) W_m \begin{pmatrix} l & k & m \\ 0 & 0 & 0 \end{pmatrix} \ . \tag{67}$$

Here, the W_m are the multipole moments of the function describing the sky coverage and the acceptance. $(\cdots)$ is the Wigner 3j-Symbol. To calculate the C_l^{true} the matrix M is inverted.
The unfolding is particularly important for the interpretation of the multipole moments C_l in terms of the angular scale. Strictly speaking, the approximation in equation (59) holds only for the true moments C_l^{true}. The observed moments are biased by the sky coverage and the acceptance. Thus, an unbiased interpretation is not possible.
The main aim of this analysis is the search for deviations from the atmospheric expectation. In order to detect these deviations it is not required to unfold the observed C_l spectrum. This can be done with the folded spectrum. Therefore the unfolding is only relevant, after a signal is detected and it is not discussed here further. More information is found in [D204].

5 Simulation of the Background and Signal Hypotheses

The influence of different signal hypotheses on the multipole moments is evaluated by simulations. The different hypotheses for deviations from the atmospheric neutrino distribution are: (See chapter 2.4 for a description of the hypotheses.)

1 neutrinos from micro & mini sources

2 neutrinos from mini sources in the (super) galactic plane

3 neutrinos from cosmic ray interactions in the galactic plane

4 oscillation of the atmospheric neutrinos

5 background from mis-reconstructed muons

The simulation is done similarly for all hypotheses, as explained in the following subsections.

All Monte Carlo sky-maps are generated from the Monte Carlo sample described in chapter 3.4. The total number of neutrinos is fixed to the number in the 4-year-sample. Due to different uncertainties it is not sufficient to perform each simulation only once. Instead, all simulations are done 1000 times for each hypothesis in order to evaluate the statistical uncertainties.
The equator is chosen as boundary for the acceptance. The simulation, however, is done for the full sky to avoid boundary effects.
All Monte Carlo sky-maps consist of atmospheric neutrinos and neutrinos from additional contributions.

5.1 Atmospheric Background Neutrinos

The dominant neutrino signal in AMANDA-II is from atmospheric neutrinos. In order to simulate atmospheric neutrinos their zenith distribution (described in chapter 2.3) has to be combined with the relative detector efficiency. The detector efficiency describes all losses due to reconstruction efficiency or event selection at different angles. These efficiencies also depend on the energy. This information is already included in the Monte Carlo sample which corresponds to the 4-year-sample.
Figure 15 shows the effective zenith distribution after selections corresponding to the 4-year-sample. The event selection changes at $\cos(180^\circ - \theta) = 0.15$ and $\cos(180^\circ - \theta) = 0.45$ [Ac06][Ac+6]. Therfore a binning of 0.05 is chosen for the histogram. The distribution is parameterised with a spline (3rd order polynomial). As we are only interested in the relative angular acceptance, the normalisation is arbitrary.

In order to generate a random sky-map of atmospheric neutrinos, a direction is chosen uniformly distributed in the sky for each event. A random number according to the parametrised detector efficiency decides if the event is kept or discarded. This is repeated until $N_{tot} = 3329$ events are reached.
Two types of uncertainties exist: Systematic deviations in the atmospheric neutrino distribution due to different models of the cosmic ray interactions and statistical uncertainties in

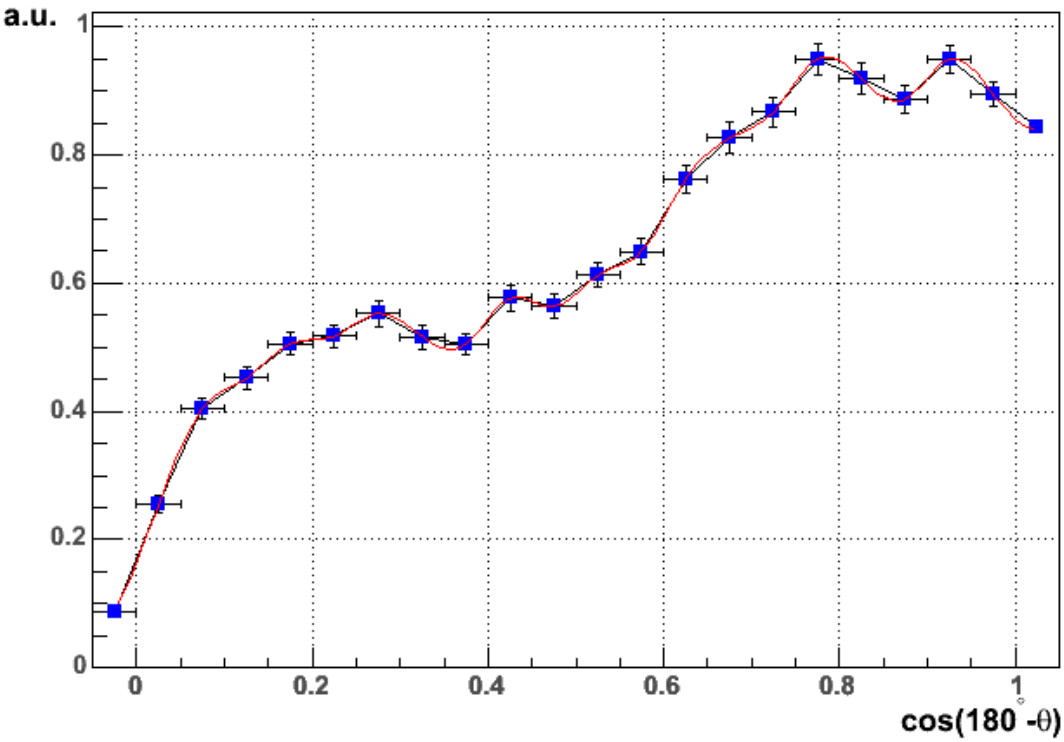

Figure 15: Zenith angle distribution of atmospheric neutrinos after detection (blue boxes) with statistical errors. The red line is a spline (3rd order polynomials) associated to this distribution. The normalisation is arbitrary and set to a maximum of 0.95.

the Monte Carlo data set. In order to quantify these effects the zenith angles distribution is varied in each of the 1000 simulations.
The systematic uncertainties in the atmospheric neutrino distribution are included by a linear 5% change in the shape. The efficiencies in each bin e_i of the histogram are correspondingly modified. The size of the modification s is given by a Gaussian distribution (mean zero and width 0.05) with a linear change from the pole to equator. It can be parametrised by:

$$e_i^{dist} = s \cdot e_i \cdot (180^\circ - \theta)/90^\circ \ . \tag{68}$$

The statistical Monte Carlo error is included by simulating the efficiency in each bin e_i with its statistical uncertainty, using a Gaussian distribution. This is done for each of the 3329 neutrino events separately.
After all modifications the distribution is renormalised to a maximum of 0.95. A spline (3rd order polynomial) is calculated to parametrise each of the simulated distributions. The values of the spline must be strictly smaller than one, because they are used as probabilities during simulation. For the southern hemisphere the probability is set to zero. As an example figure 16 shows one simulated data sample.

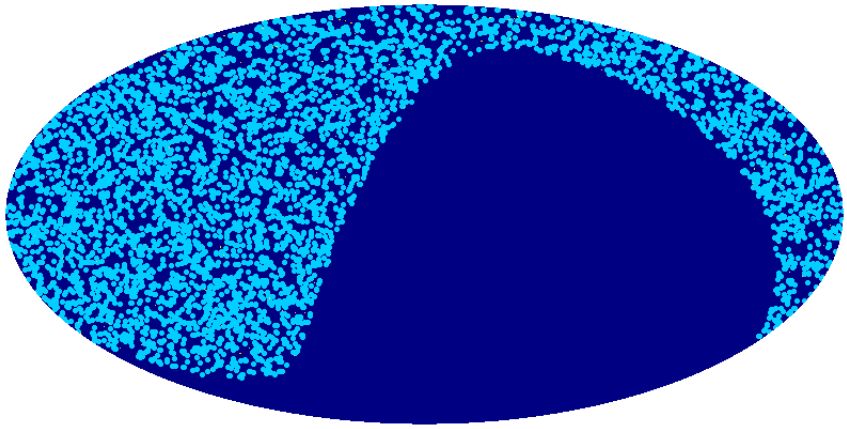

Figure 16: Sky map of atmospheric neutrinos distributed as given by the spline in figure 15 (in galactic coordinates with the galactic centre in the middle).

type	μ	γ	N_s
mini sources	1	2,2.5	10-1000
micro sources	2,3	2,2.5	10-1000

Table 3: Values for μ, γ and N_s for isotropic point sources.

5.2 Neutrinos from Isotropic Point Sources

One hypothesis for extra-terrestrial neutrinos are isotropically distributed weak point sources (described in 2.4.6). The simulation procedure is similar to the atmospheric neutrinos and is shown in figure 17. A difference is the clustering of neutrinos from the same source and the sky distribution. These hypotheses are parameterised by:

- the number of neutrino sources N_s
- the mean number of neutrinos per source μ
- the energy spectrum $E^{-\gamma}$
- the sky distribution d

The values used for this parameters in the simulation are given in table 3.
An isotropically distributed source direction $\vec{\omega}_s$ and a Poisson distributed (mean μ) number n_ν of neutrinos are generated for the full sky. For the neutrino directions the reconstruction error is taken into account by a point spread function. It is estimated by the difference between the true and the reconstructed direction in the Monte Carlo data (shown in figure 18).
The errors are typically of the size of a few degrees, but a small tail of the probability density reaches up to 180°. By simulating directions on the full sky, neutrinos can appear from or disappear to the upper sky.

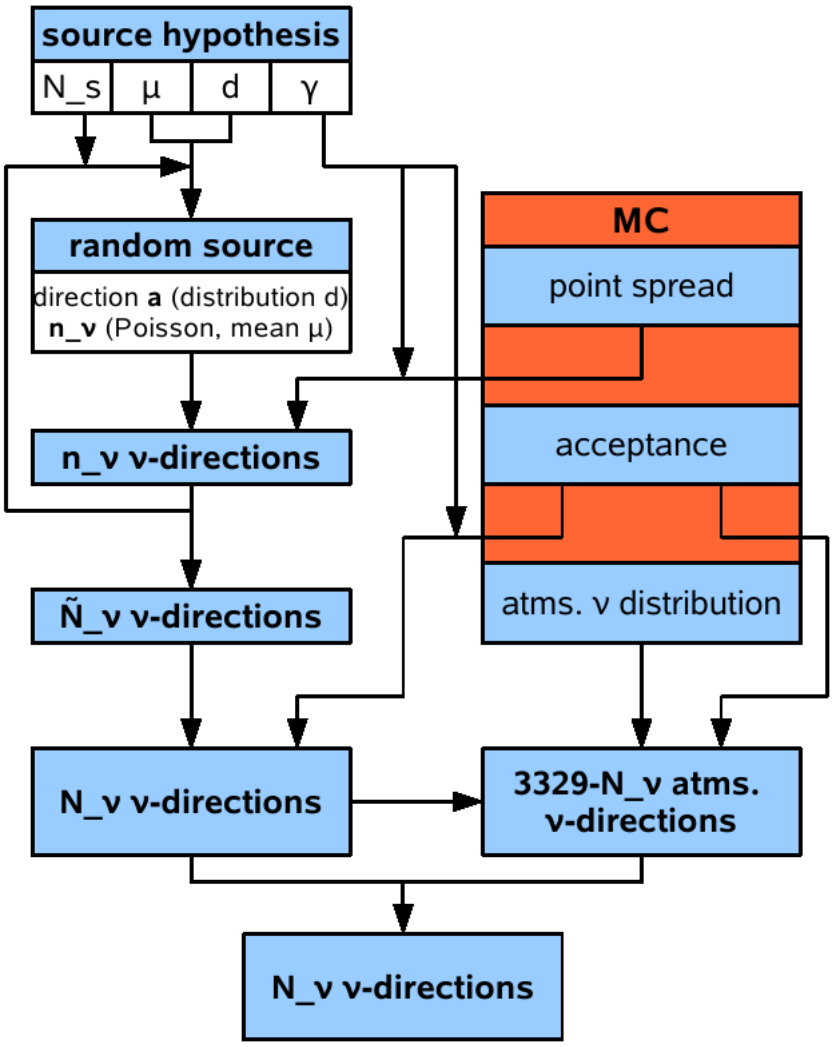

Figure 17: Simulation procedure. Main simulation steps are presented in blue boxes. The white boxes show important parameters of the simulation steps. On the right side three blue boxes are included by one red box titled "MC" to express that this information is taken from the Monte Carlo data set.

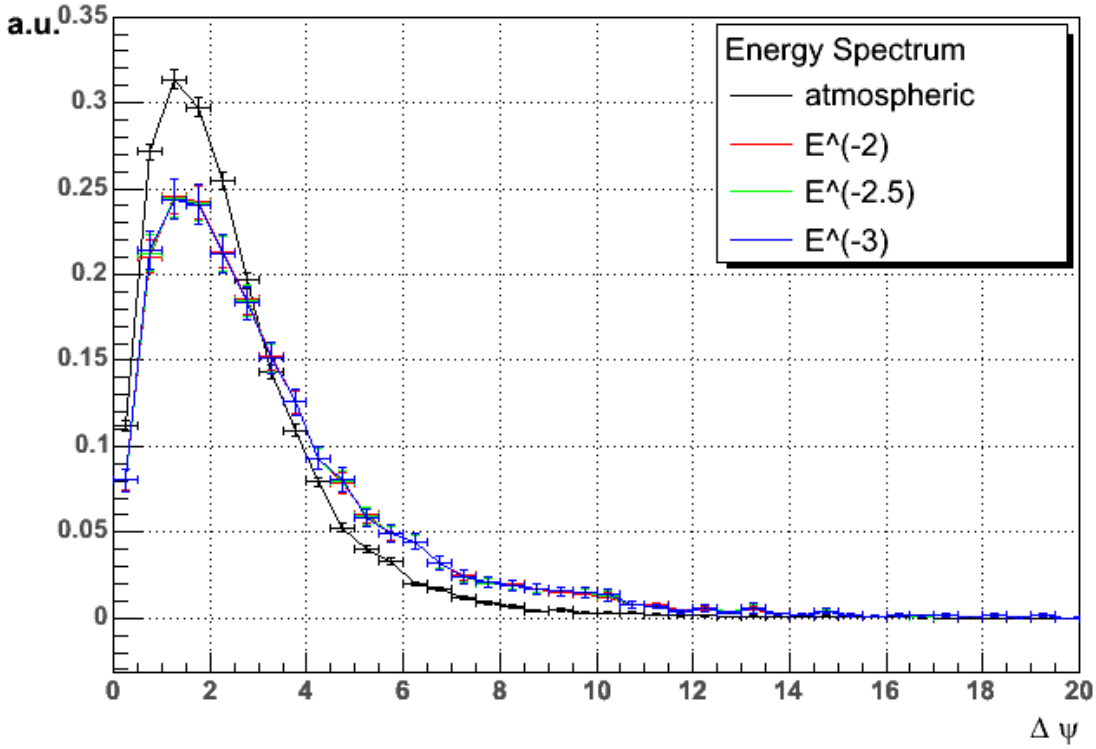

Figure 18: Probability density of the difference between the reconstructed and true directions, for different energy spectra from Monte-Carlo data.

For each neutrino a direction is generated with an angle to the source direction corresponding to this probability density. This is repeated for all N_s sources. By this a total number of $\tilde{N}_\nu$ neutrino directions is generated.
In the next step, the detector efficiency is applied. Similarly to the atmospheric neutrinos it is taken from the Monte Carlo data. Due to the changed energy spectrum also the efficiency changes. The angular distribution is renormalised to a maximum of 0.95 and a spline (3rd order polynomial) is applied. Figure 19 and 20 show the zenith dependence of the efficiency for the spectral indices of $\gamma = 2$ and 2.5.
The final data sample contains neutrino directions according to this angular distribution. The effective number of neutrinos N_ν by all sources in the sample is smaller by a factor ϵ. The mean of ϵ is the integral over the efficiency. For $\gamma = 2$ this factor is $\epsilon = 0.8230$ and for $\gamma = 2.5$ the factor is $\epsilon = 0,6988$ (More values for ϵ are given in appendix C). Atmospheric neutrinos are used to fill the simulated number of neutrino directions up to $N_{tot} = 3329$. They are generated as described in the chapter 5.1. Figure 21 shows an example map.

5.3 Neutrinos from Point Sources in the (Super-) Galactic Plane

Another possible event distribution are neutrino sources located in the (super-) galactic plane (described in chapter 2.4.6).

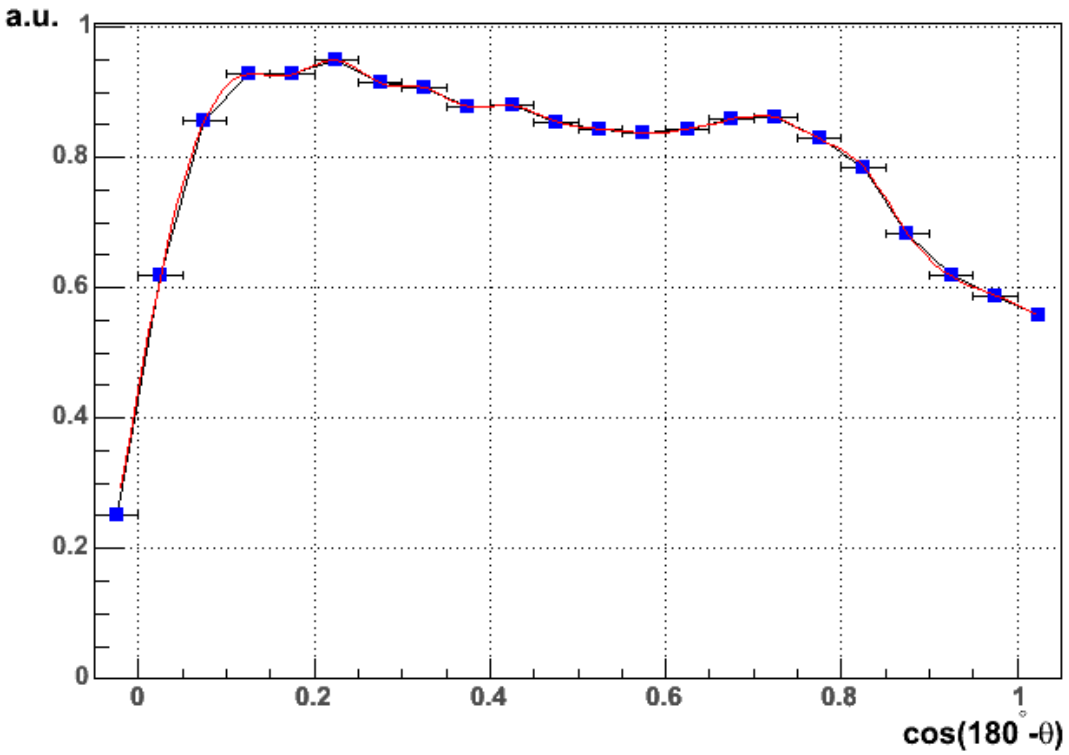

Figure 19: The angular acceptance of the detector including the selection efficiency, as a function of zenith angle, for isotropic neutrinos with a power index $\gamma = 2$. Data from Monte-Carlo is used (blue dots) and a spline (red line) is applied. The maximum is normalised to 0.95.

The simulation is done similarly to the simulation of the isotropically distributed point sources. (The simulation procedure is shown in figure 17.) Here not an isotropic event distribution is used but a distribution d according to the (super-) galactic plane. This distribution follows the description in [IC05].

The expected distribution is flat in (super-) galactic longitude and Gaussian distributed perpendicular to the (super-) galactic equator with a width of 2.1°. For the simulations the Monte Carlo is re-weighted (described in appendix B). The expected energy spectrum is the same as for point sources. Here, an index γ of 2 and 2.4 is used for the simulations. The zenith angle dependent detector acceptance (figures 19 and 22) and the angular resolution (figure 18) are taken into account in the same way as for the isotropically distributed sources. The two factors for the detector efficiency ϵ are: $\epsilon = 0.8230$ for $\gamma = 2$ and $\epsilon = 0.7329$ for $\gamma = 2.4$. (More values for ϵ are listed in appendix C.) These factors do not include the location of the (super-) galactic plane in the sky. This is considered separately for the final results.

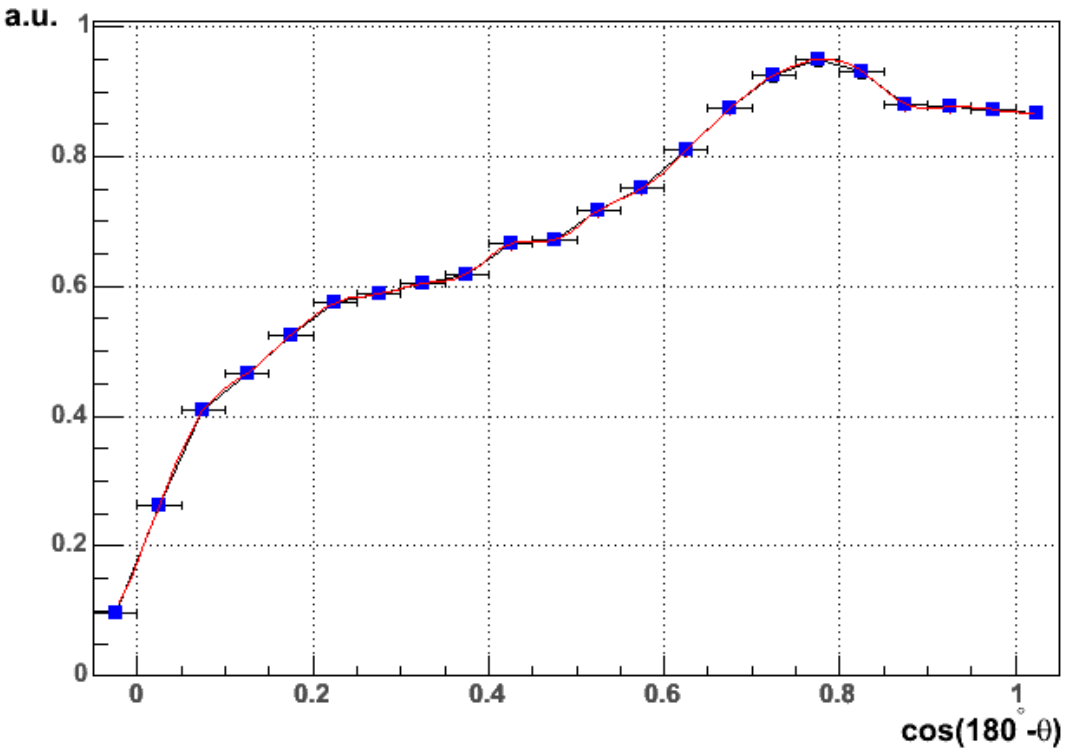

Figure 20: The angular acceptance of the detector including the selection efficiency, as a function of zenith angle, for isotropic neutrinos with a power index $\gamma = 2.5$. Data from Monte-Carlo is used (blue dots) and a spline (red line) is applied. The maximum is normalised to 0.95.

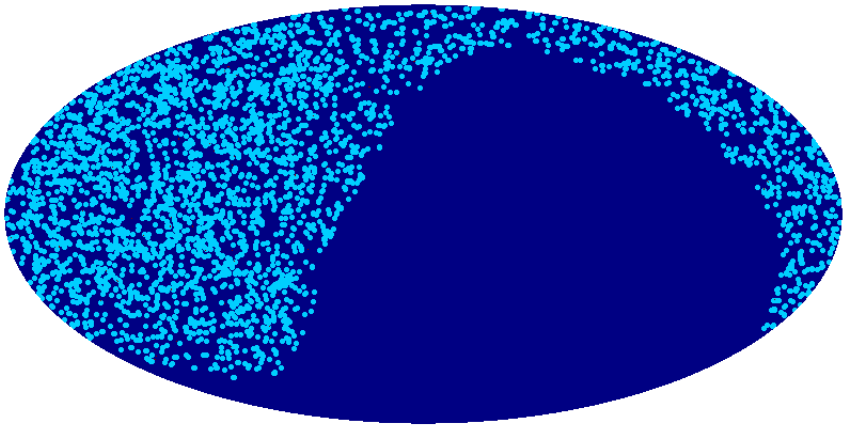

Figure 21: Sky-map of 3329 neutrinos generated with 600 neutrino sources in the full sky ($\mu = 3$ and $\gamma = 2$).

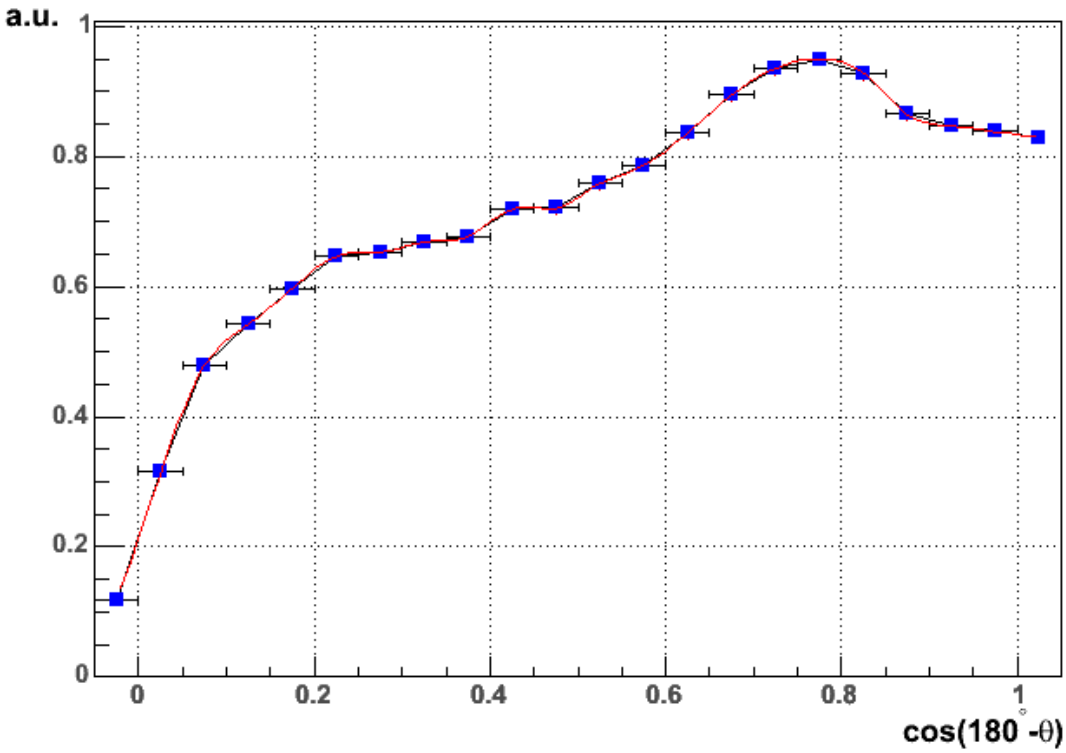

Figure 22: The angular acceptance of the detector including the selection cuts, as a function of zenith angle, for isotropic neutrinos with a power index $\gamma = 2.4$. Data from Monte-Carlo is used (blue dots) and a spline (red line) is applied. The maximum is normalised to 0.95.

5.4 Neutrinos from Cosmic Ray Interactions in the Galactic Plane

Neutrinos from cosmic ray interactions in the galactic plane (described in chapter 2.4.6) are simulated analogous to point sources in the galactic plane. Here, the neutrino directions are not correlated as no discrete sources exist.

For cosmic rays an energy spectrum with $\gamma = 2.7$ is expected for the neutrinos. The strength of this signal is given by a fraction f of neutrinos in the whole sample which originate from the galactic plane. f is varied in the simulations between 0.5% and 20%. Figure 23 shows the corresponding zenith angle dependent detector acceptance. It has a mean efficiency of $\epsilon = 0.6449$. The sky distribution is the same as for the point sources in the galactic plane.

This simulation of an event takes the reconstruction error in the direction into account. (The same procedure as for point sources is used.) The reconstruction errors are taken from the difference between true and reconstructed direction in the Monte Carlo (figure 18). The result of the point spread function is a broadening of the (super-) galactic plane. An example sky-map is shown in figure 24.

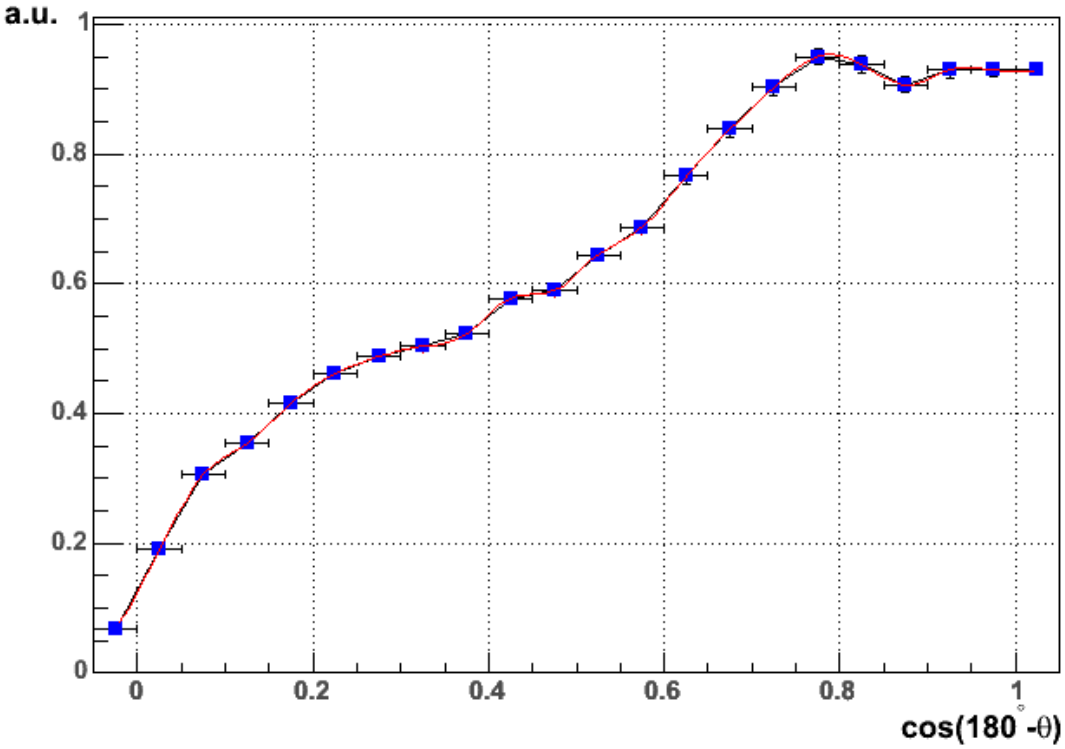

Figure 23: The angular acceptance of the detector including the selection efficiency, as a function of zenith angle, for isotropic neutrinos with a power index $\gamma = 2.7$. Data from Monte-Carlo is used (blue dots) and a spline (red line). The maximum is normalised to 0.95.

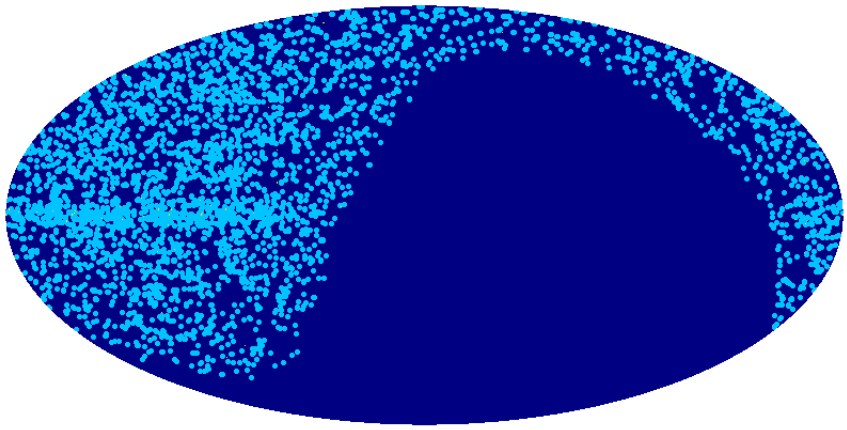

Figure 24: Sky-map of 3329 neutrinos with a fraction of 20% from the galactic plane.

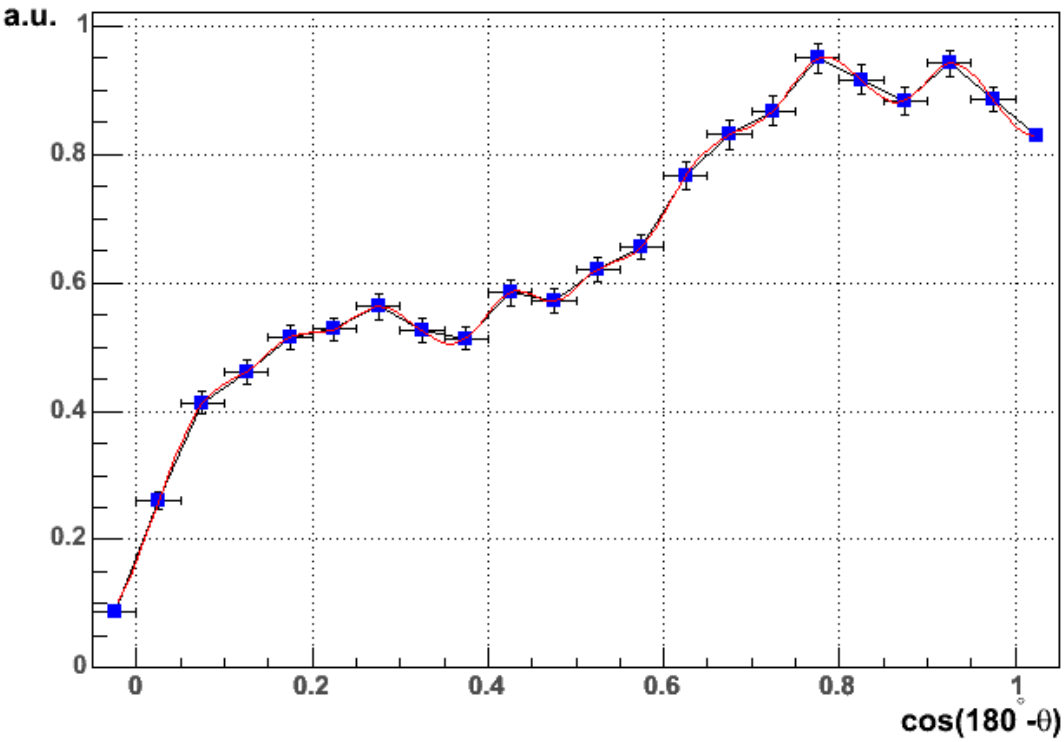

Figure 25: The angular acceptance of the detector combined with the zenith angle distribution of the atmospheric neutrinos and oscillations ($\Delta m^2 = 5$ meV^2). Data from Monte-Carlo (blue dots) is used and a spline (red line) is applied. The maximum is normalised to 0.95.

5.5 Oscillation of the Atmospheric Neutrinos

Neutrinos can change their flavour while travelling through the earth as described in chapter 2.3.1. This induces a zenith angle dependent disappearance of atmospheric muon-neutrinos.
The simulation uses equation (4) as additional weight. The other steps are the same as described for atmospheric neutrinos. The parameter Δm^2 is varied between values of 1 meV^2 and 10 meV^2.
As an example figure 25 shows the zenith angle dependent detector efficiency including this effect for $\Delta m^2 = 5$ meV^2. No obvious differences to the angular distribution of the atmospheric neutrinos occur.

5.6 Mis-Reconstructed Down-Going Muons

As described in chapter 3.3.6 the fraction of mis-reconstructed down-going muons is estimated to be less than 5%. This must be taken into account for this analysis.
No predictions for the sky distribution of these mis-reconstructed muons exist. Thus, it is not possible to a priori include them into the atmospheric neutrino simulation. Instead

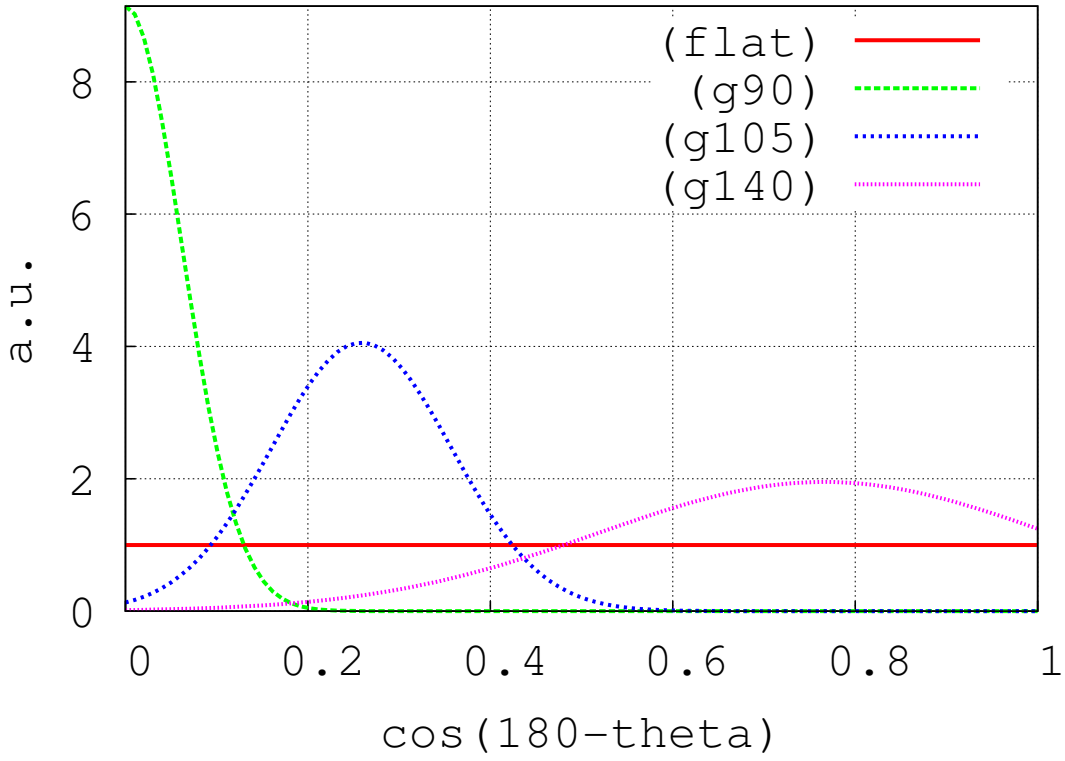

Figure 26: Hypotheses for the zenith distribution of down-going muons. All hypotheses are normalised to an integral of one.

mis-reconstructed down-going muons are simulated similarly to the signal hypotheses. Various hypotheses for this background are defined in chapter 5.6.1. An additional test is performed to chose the most probable of these background hypotheses in chapter 8.1 and 8.2.

5.6.1 Hypotheses for Down-Going Muons

For reasonable hypotheses of the sky distribution of the mis-reconstructed down-going muons the initial muon distribution and the probability for such a mis-reconstruction (angle dependent) have to be taken into account. Down-going muons are generated in showers from cosmic particles interacting in the atmosphere. These particles hit the atmosphere isotropically distributed over the sky. No azimuth angle dependence is expected.
The probability for mis-reconstruction is different. Almost no information is available[16]. We assume a flat distribution in right ascension, due to the rotation of the detector with the axis through the poles of the Earth. Different models for the zenith angle distribution are used. The hypotheses for this distribution are (figure 26):

[16] Otherwise these events would have been rejected earlier.

(flat) 5% flat distribution in $\cos\theta$

(g90) 4% Gaussian distributed (width 5°) at the horizon (90° zenith angle) and 1% flat distributed in $\cos\theta$

(g105) 3% Gaussian distributed (width 8°) at 105° zenith angle and 2% flat distributed in $\cos\theta$

(g140) 5% Gaussian distributed (width 20°) at 140° zenith angle $\cos\theta$

Percentages refer to the fraction of events in the 4-year-sample.
A flat distribution is the most naive expectation of such a background. The peak at the equator (g90) is motivated by the difficulties in discriminating between up- and down-going events in this region. The excess at 105° (g105) is motivated by [Gr06]. It describes a possible small excess at this angle. The hypothesis (g140) corresponds to a "ghost peak" due to detector symmetries,observed without cuts.

The simulation is done similarly to the atmospheric neutrinos. The angular detector response is modified by adding events according to the different background distributions to include the described hypotheses. The strength of the contribution is varied between 0.05% and 20%.

6 Analysis of Monte Carlo Data

An overview of the analysis procedure was presented in chapter 4 (figure 12). The first part of this chapter discusses how the angular spectrum for each simulated sample is calculated by the "GLESP" software (chapter 6.1 and 6.2). From these spectra the multipole moments for the analysis are selected and optimised (chapter 6.4). The last part of this chapter summarises the creation of confidence belts and the calculation of upper limits (chapter 6.5).

6.1 Determination of the Angular Power Spectrum

The calculation of the angular power spectrum requires integrating over the unit sphere (equation 57). Implementing a stable integration algorithm with small errors is difficult due to the strong oscillations of the spherical harmonics Y_l^m (equation 51); for the zenith angle the number of oscillations is proportional to l and for the azimuth angle it is proportional to m (figure 13). So, the integration is difficult particularly for large multipole moments.
In this analysis the calculation of the angular power spectrum is done by the "GLESP" software [Do05], which was developed for cosmic microwave background maps. The algorithm covers the sphere with pixels. The positions in the zenith coordinate of the centre of these pixels are the so-called Gauss-Legendre quadrature zeros. Additionally the pixels have equal size and nearly equal shape when using "GLESP". More information about "GLESP" can be found in [Do05].
Important for the optimisation in chapter 6 is the maximum multipole index l_{max}^{glesp} for which "GLESP" can calculate the multipole moment. Simulations with different numbers of neutrino events are made for atmospheric neutrinos; figure 27 shows the result. The mean of 1000 simulations is used to reduce fluctuations due to the limited numbers of neutrinos.
The calculated multipole moments depend on the number of events. For a larger number of events the moments get smaller. At small l the reduction varies for different multipole moments. For large l the decrease is similar for all moments. Furthermore, at large l the moments have about the same values for a constant number of events. At the index $l = 27$ and 29 two peaks are visible at high statistics.
The constant values for large moments show that the calculation of the multipole moments is stable even if the event statistic is too low to determine the actual value of the multipole moment (equation 65).
It is useful to analyse this value of the multipole moments C_{min}, as function of the event statistics. These values correspond to the maximum sensitivity that this analysis can achieve as function of the available statistics. The angular power spectra in figure 27 obey approximately the relationship:

$$C_{min}(N_{tot}) \propto \frac{1}{N_{tot}} \, . \tag{69}$$

For a hypothetical power spectrum moments $C_l < C_{min}(N_{tot})$ are indistinguishable from the atmospheric background. No maximum multipole index l_{max}^{glesp} can be set because the C_l that exceed the limit of C_{min} depend on the distribution of the events. This can be

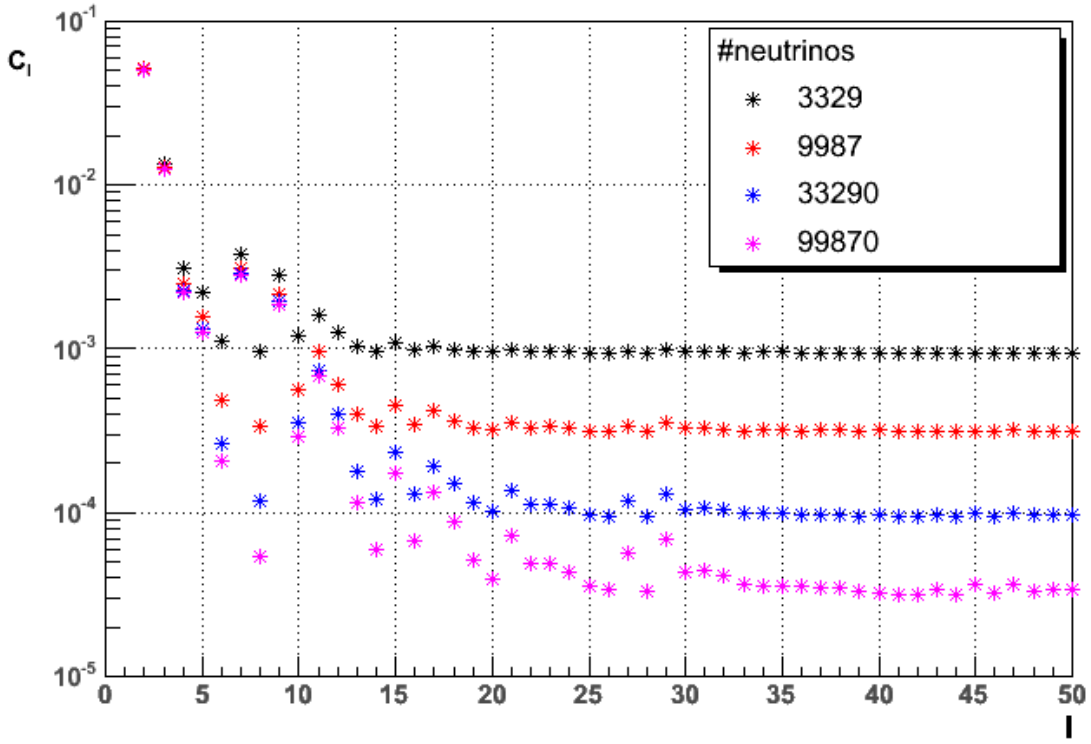

Figure 27: Angular power spectrum of atmospheric neutrinos calculated by "GLESP" for different numbers of neutrino events.

seen at the two peaks at $l = 27$ and 29 for the atmospheric spectrum used here. Both exceed C_{min} and for smaller multipole indices already values similar to C_{min} are seen. The decreases of the C_l at small l with rising N_{tot} can be explained by smaller summands when averaging due to the lowered limit. This effect is bigger for moments with a value near the lower limit $C_{min}(N_\nu)$.

6.2 Resulting Angular Power Spectrum

Using the information in chapter 6.1 the power spectra can be readily calculated. The results for the different hypotheses are discussed in the following sub-chapters. The power spectra for mis-reconstructed down-going muons are discussed separately in chapter 8.

6.2.1 Atmospheric Neutrinos

Figure 28 shows the simulated angular power spectrum for atmospheric neutrinos. The spectrum drops with increasing l at small multipole moments (about two orders of magnitude). Above $l = 13$ the values rise steadily. Between $l = 6$ and $l = 10$ high values are observed for even l and small values for odd l.
The relative errors due to the statistical uncertainty from the Monte Carlo data set and

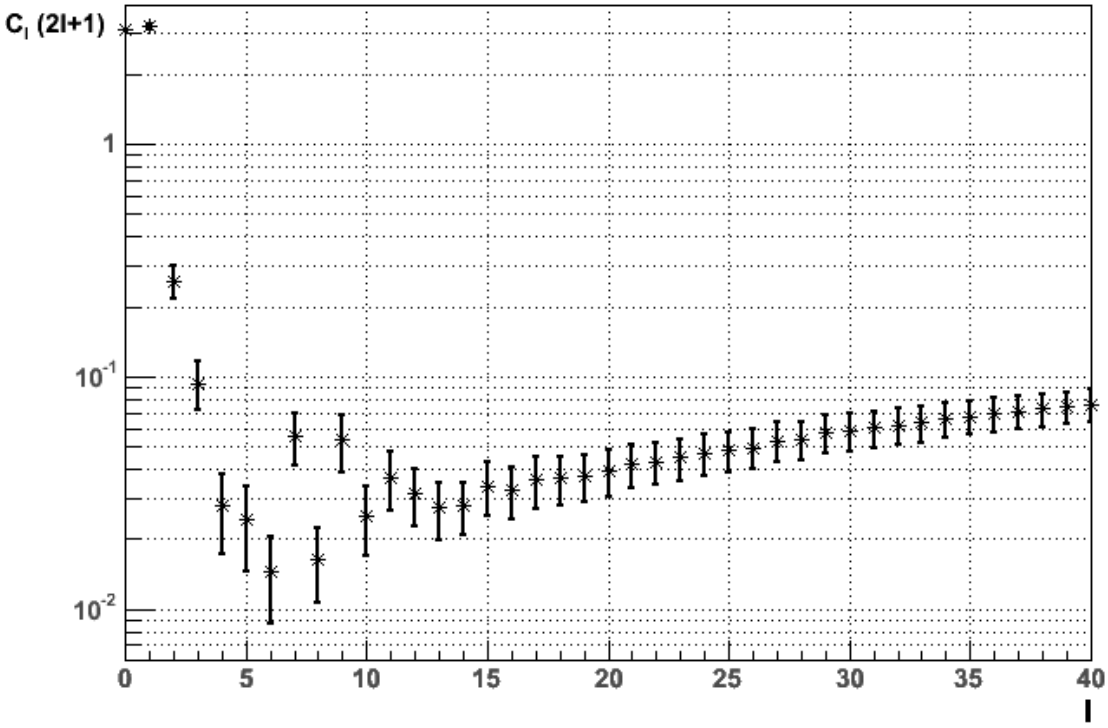

Figure 28: Angular power spectrum for atmospheric neutrinos. The error bars show the 1σ spread of 1000 simulations due to statistical uncertainties from the Monte Carlo and uncertainties in the atmospheric neutrino distribution.

due to the uncertainty in the atmospheric neutrino distribution have about the same size for most moments. For $l = 0$ no error is plotted because the spectrum is normalised to $C_l = \pi$ (chapter 4.2). The relative error for C_1 is smaller than the other ones.
The steady increase at large multipole moments is explained by the factor $(2l + 1)$ for the calculation of the power spectrum. The minimum C_l calculated by "GLESP" is constant (chapter 6.1). A linear growth with l is expected for moments $C_l = C_{min}(N_\nu)$.
Further investigations of this angular power spectrum must be compared to the spectrum of the half sphere (calculated in appendix A) because this is the dominant contribution. Most of the properties of the power spectrum for the atmospheric neutrinos are explained by this.
The dipole moment C_1 (describing the half sphere structure) is large in both spectra. This structure has small uncertainties due to event statistics and different angular distributions of the atmospheric neutrinos.
In the angular power spectrum of the half sphere all multipole moments with even l ($l \neq 0$) are zero and the odd moments are decreasing with l. This explains the steeply falling spectrum and the odd-even fluctuations in the angular power spectrum of the atmospheric neutrinos.
It is also worth noting that these fluctuations do not appear at the moments with $l = 1$ to

5. Here, the moments $l = 2$ and 4 are larger than for the half sphere and 5 is smaller. These effects result from the non-uniform angular distribution of the atmospheric neutrinos and of the zenith angle dependent detector efficiency.
In the following, all angular power spectra will be compared to the spectrum of the atmospheric neutrino distribution because it is the dominant contribution.

6.2.2 Isotropic Mini and Micro Sources

The isotropic mini and micro sources are described by the number of neutrinos per source μ, the energy spectrum $E^{-\gamma}$ and the number of sources N_s. To understand the dependencies of the angular power spectra, spectra for different parameters have to be considered. Figures 29 to 31 show mean angular spectra with two values of μ and γ. The number of sources N_s is varied for all of these spectra. Here, the mean of the 1000 simulations is shown to get rid of statistic uncertainties.
The corresponding angular power spectra for the other hypotheses are shown in appendix D.
The angular power spectrum for the mini sources with $\mu = 1$ (figure 29) is similar to the power spectrum of the atmospheric neutrinos, especially for multipole moments with $l > 10$. The deviations increase with the number of sources.
For $l > 10$ all moments increase with the number of sources but even for 864 neutrinos, from these sources in the data sample, the deviations are smaller than the error in the atmospheric expectation. For the multipole moments with $l = 2, 3, 5$ large deviations are observed. The changes in C_4 are exceptionally small.
The angular power spectrum for mini sources with $\gamma = 2$ and $\mu = 3$ (figure 30) behaves similar to the spectrum from micro sources ($\mu = 1$). For $l = 2, 3, 5$ large deviations in different directions are observed, while for $l = 4$ only small deviations occur. Above $l = 10$ all moments grow with a rising number of sources N_s.
Compared to the mini sources the multipole moments for $l > 10$ grow faster while the moments from $l = 1 - 5$ show approximately the same dependencies on the neutrino number.
The angular power spectrum for mini sources with $\gamma = 2.5$ and $\mu = 3$ (figure 31) has only distinguishable deviations from the atmospheric expectation for multipole moments with $l > 10$. Here, all moments grow with the number of sources N_s. For $l = 1$ to 5 all moments have about the value as those expected by the power spectrum of the atmospheric neutrinos.
The behaviour of the angular power spectra for mini and micro sources can be separated into two effects. The multipole moments with $l > 10$ change with the number of neutrinos per source μ, while the moments with $l \leq 5$ depend on the energy spectrum.
Neutrinos from one source have differences in their directions due to the finite detector resolution; this is described by the point spread function (chapter 5.2). The difference in the direction is at the scale of $\sim 3^\circ$. For weak sources there are less neutrinos with this angular difference than for strong sources. The deviations at the high multipole moments $l > 10$ can be explained by the dependency on the source strength μ.
To explain the different behaviours at small multipole moments, $l = 2, 3, 5$, effects at larger scales are required. Here the changes depend on the power index of the energy spectrum. For $\gamma = 2$ large deviations exist, which vanish for $\gamma = 2.5$. This can be explained by the

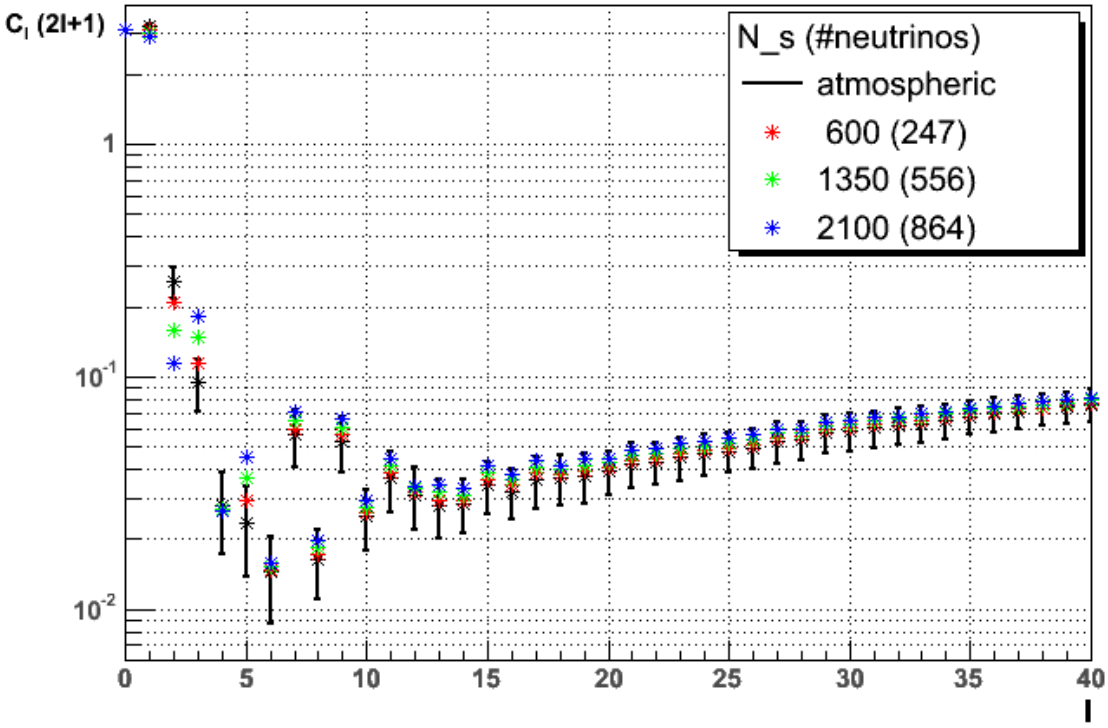

Figure 29: The mean angular power spectrum for micro sources with $\gamma = 2$ and $\mu = 1$ for different source numbers compared to the expectation from the atmospheric neutrinos. The black stars are the mean values for the atmospheric expectation $< C_{l\_atms} >$ with 1σ spread as error bars. The coloured stars are the mean multipole moments for the micro source hypothesis. They have a statistical spread of similar size which is not plotted here. In the legend the number of sources on the whole sphere and the mean number of neutrinos from these sources in the data sample (in brackets) are given.

change in the detector efficiency as a function of γ. The detector efficiency for a spectral index of $\gamma = 2.5$ (figure 20) is similar to the zenith angle distributions of atmospheric neutrinos including the detector efficiency (figure 15 and 20). For $\gamma = 2$ the distributions differ (figure 19).
Finally the behaviour of C_4 has to be explained. For all simulations of the isotropic mini and micro sources almost no changes are observed. C_4 is the multipole moment with the lowest l which is completely symmetric to the equator (compare figure 13). Only effects on both hemispheres or radical changes in the shape for the (super-) galactic plane lead to changes of C_4.

6.2.3 Neutrinos from the (Super-) Galactic Plane

For hypotheses of neutrinos from the (super-) galactic plane there exist only weak dependencies of the angular power spectrum on different parameters (γ, μ). Figure 32 shows

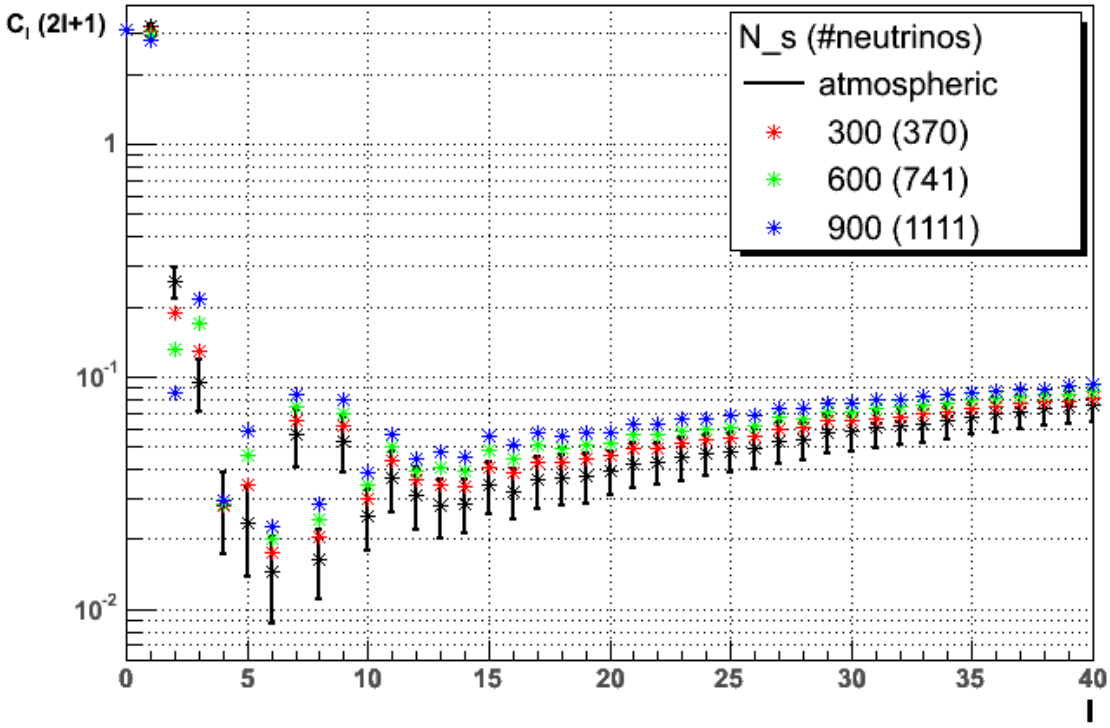

Figure 30: The mean angular power spectrum for mini sources with $\gamma = 2$ and $\mu = 3$ for different source numbers compared to the expectation from the atmospheric neutrinos. The black stars are the mean values for the atmospheric expectation $< C_{l\_atms} >$ with 1σ spread as error bars. The coloured stars are the mean multipole moments for the mini source hypothesis. They have a statistical spread of similar size which is not plotted here. In the legend the number of sources on the whole sphere and the mean number of neutrinos from these sources in the data sample (in brackets) are given.

examples of the spectra for mini sources in the galactic plane with $\gamma = 2$ and $\mu = 3$. For examples of spectra for neutrinos from cosmic-ray interactions in the galactic plane see figure 33.

The corresponding angular power spectra for other hypotheses are shown in appendix D.

The angular power spectrum for mini sources in the galactic plane shows deviations from the atmospheric expectation at the multipole moments with $l = 3$ to $l \approx 17$. All multipole moments grow with the fraction of neutrinos from the plane, especially the moments with $l = 4, 5, 6, 8$, which have low values for the atmospheric expectation. In addition, the odd-even oscillations are reduced and the decrease of the spectrum for the first moments is less steep.

The Angular power spectrum for the cosmic ray interactions in the galactic plane is similar to the spectrum of the mini sources in the plane (figure 32 and 33). The multipole moments between $l = 3$ and 17 increase with rising source number N_s. The largest changes are observed for $l = 4, 5, 6, 8$.

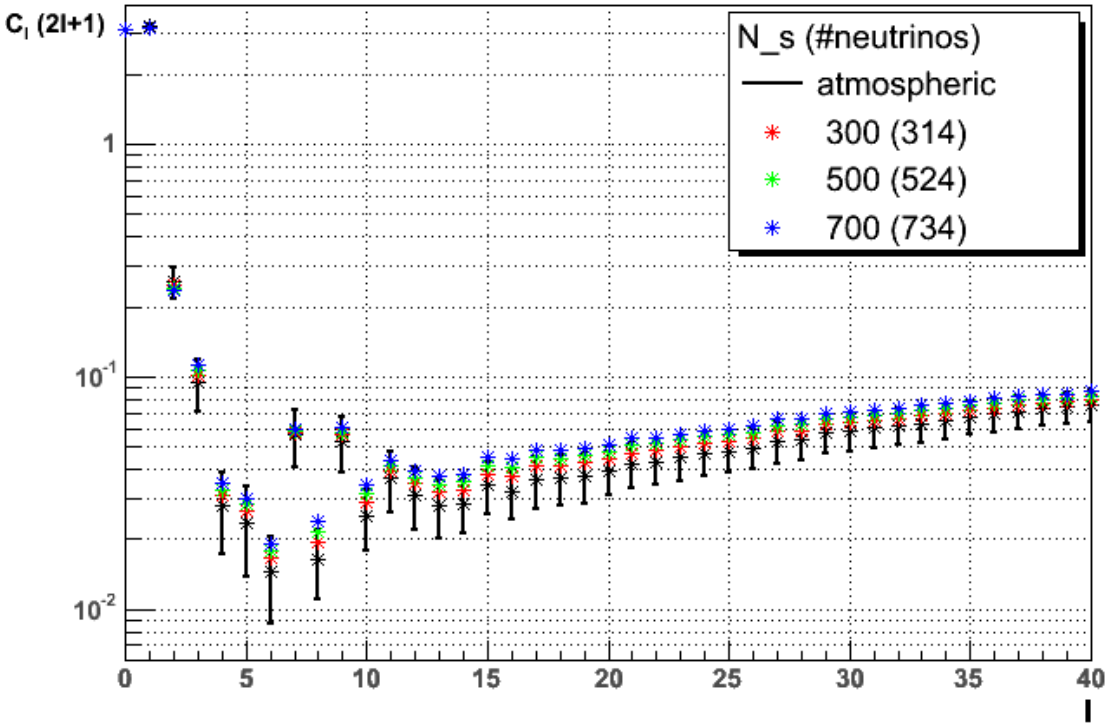

Figure 31: The mean angular power spectrum for mini sources with $\gamma = 2.5$ and $\mu = 3$ for different source numbers compared to the expectation from the atmospheric neutrinos. The black stars are the mean values for the atmospheric expectation $< C_{l\_atms} >$ with 1σ spread as error bars. The coloured stars are the mean multipole moments for the mini source hypothesis. They have a statistical spread of similar size which is not plotted here. In the legend the number of sources on the whole sphere and the mean number of neutrinos from these sources in the data sample (in brackets) are given.

The changes in the angular power spectra are similar for all hypotheses with the (super-) galactic plane. The differences are an effect of the description of the plane. The dependencies on the additional parameters are weak compared to this. A half ring (this is how the galactic plane approximately appears on a half sphere) is described by different multipole moments to a half sphere. For a ring with a width at a scale of $\sim 6°$ large moments have bigger contributions than for the half sphere, so the C_l decrease slower with l and the odd-even effects are reduced.

6.2.4 Neutrino Oscillations

The angular power spectrum for neutrino oscillations shows almost no significant difference to the expected spectrum for atmospheric neutrinos. Only the multipole moments C_2, C_3 and C_5 differ; the difference for C_5 is small (see figure 34).
The power spectra are similar because there is no big difference in the sky distribution of

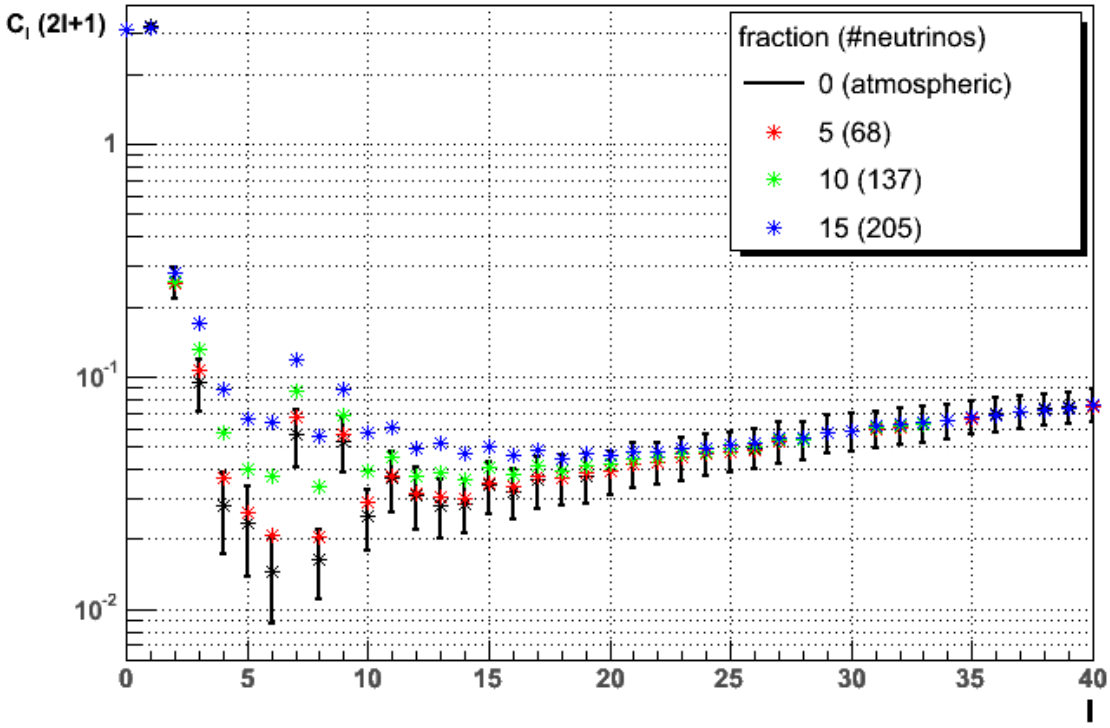

Figure 32: Angular power spectrum for mini sources ($\gamma = 2$,$\mu = 3$) in the galactic plane compared to the expectation from the atmospheric neutrinos. The black stars are the mean values for the atmospheric expectation $< C_{l\_atms} >$ with 1σ spread as error bars. The coloured stars are the mean multipole moments for the signal hypothesis. They have a statistical spread of similar size which is not plotted here. In the legend the fraction of neutrinos from sources in the galactic plane and the mean number of neutrinos from these sources in the data sample (in brackets) are given.

the atmospheric neutrinos with and without oscillation. The oscillation causes the largest loss at the pole and the smallest loss at the equator. The zenith angle distribution of the neutrino directions gets flatter with the additional weight. This corresponds to a lower C_2 as it is observed because C_2 is sensitive to the difference of the signal strength between the pole and the equator (compare figure 13).

6.3 Statistical Properties of the Fluctuations

For the analysis it is important to understand the statistical properties of the angular power spectra. A second independent set of 1000 atmospheric background samples is simulated and the corresponding 1000 angular power spectra are calculated. The spectra of the samples are compared to the mean spectrum of the first set by a χ^2-test. From these χ^2-values a probability p is calculated for the additional spectra to be identical to the original one. The distribution of these probabilities is shown in figure 35.

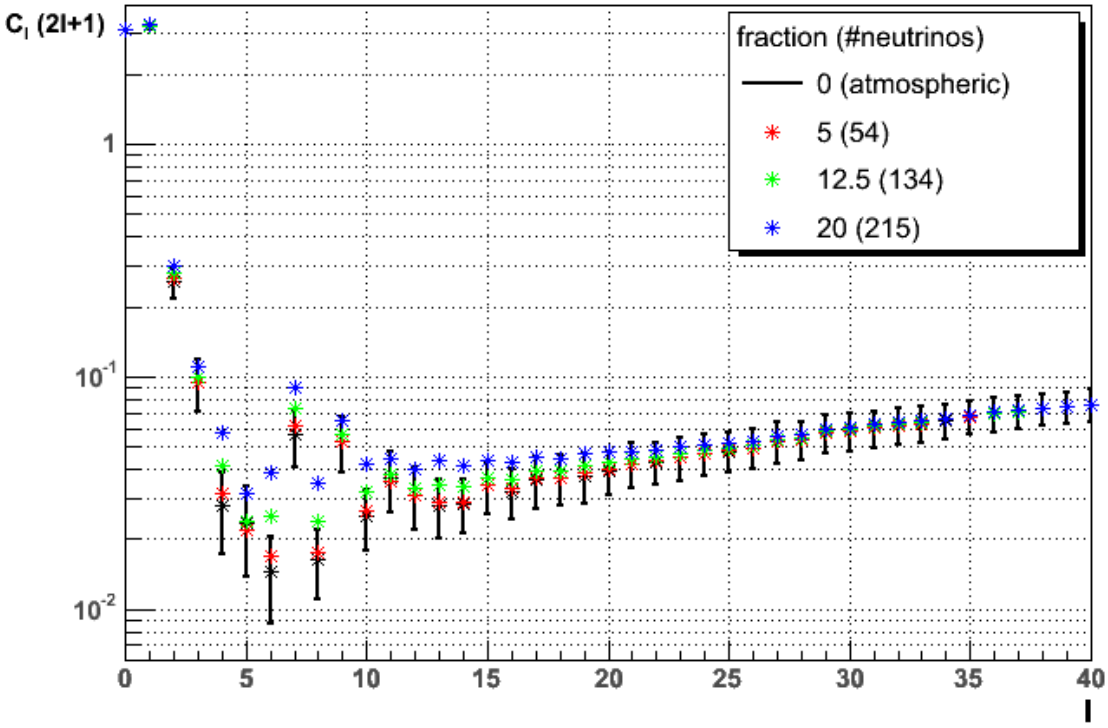

Figure 33: Mean angular power spectrum for neutrinos from cosmic ray interactions in the galactic plane compared to the expectation from the atmospheric neutrinos. The black stars are the mean values for the atmospheric expectation $< C_{l\_atms} >$ with 1σ spread as error bars. The coloured stars are the mean multipole moments for the signal hypothesis. They have a statistical spread of similar size which is not plotted here. In the legend the fraction of 3329 events of neutrinos from the galactic plane and the mean number of neutrinos from these sources in the data sample (in brackets) are given.

The figure shows a line for the expectation from independent Gaussian distributed moments in the power spectrum. The calculated distribution has two peaks, one for small ($p < 0.05$) and one for large probabilities ($p > 0.95$). In between the distribution is nearly constant with a small minimum at about 0.5.

The deviations from the Gaussian expectation show that the different moments are not independent and Gaussian distributed. Because of this the observable in chapter 4 is called D^2 instead of χ^2. Correlations between the moments were observed in chapter 4.4. The deviation from the Gaussian expectation is not big. Thus, for the optimisation of the sensitive region in the following chapter the χ^2 distribution is used. In the final analysis the distributions of the moments and the correlations are correctly taken into account by calculating confidence belts (chapter 6.5).

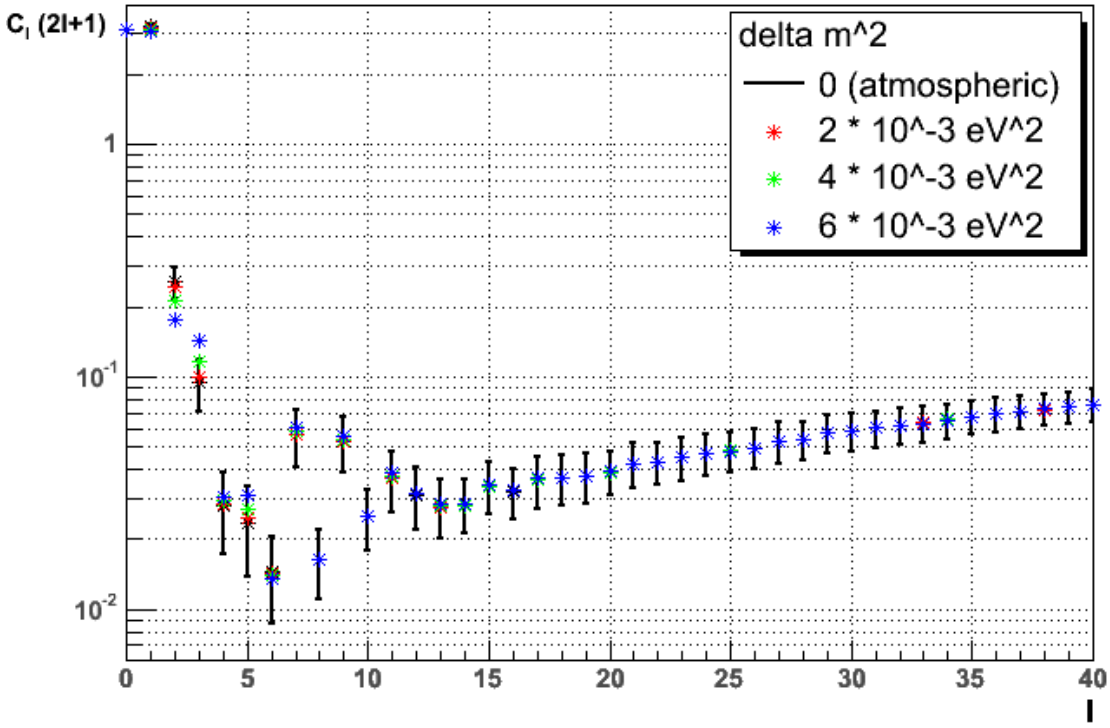

Figure 34: Angular power spectrum for neutrino oscillation compared to the expectation from the atmospheric neutrinos. The black stars are the mean values for the atmospheric expectation $< C_{l\_atms} >$ with 1σ spread as error bars. The coloured stars are the mean multipole moments for the signal hypothesis. They have a statistical spread of similar size which is not plotted here.

6.4 Optimisation of the Sensitive Region

For the selection of the multipole moments for the analysis the statistical and systematic characteristics are important. These are:

- $l_{max}^{angular} < 64$ due to angular resolution [chapter 4.3]
- $l_{max}^{dof} \leq 57$ due to the number of events [chapter 4.3]
- correlations for small multipole indices l and next neighbour correlations for all indices [chapter 4.4]
- $C_{min} \propto N_{tot}^{-1}$, the minimum value calculated by GLESP [chapter 6.1]

These values are not strict upper bounds for the multipole moments used. Instead they only provide a hint at the maximum multipole index. For this reason the moments used for each signal hypothesis are optimised to maximise the sensitivity.

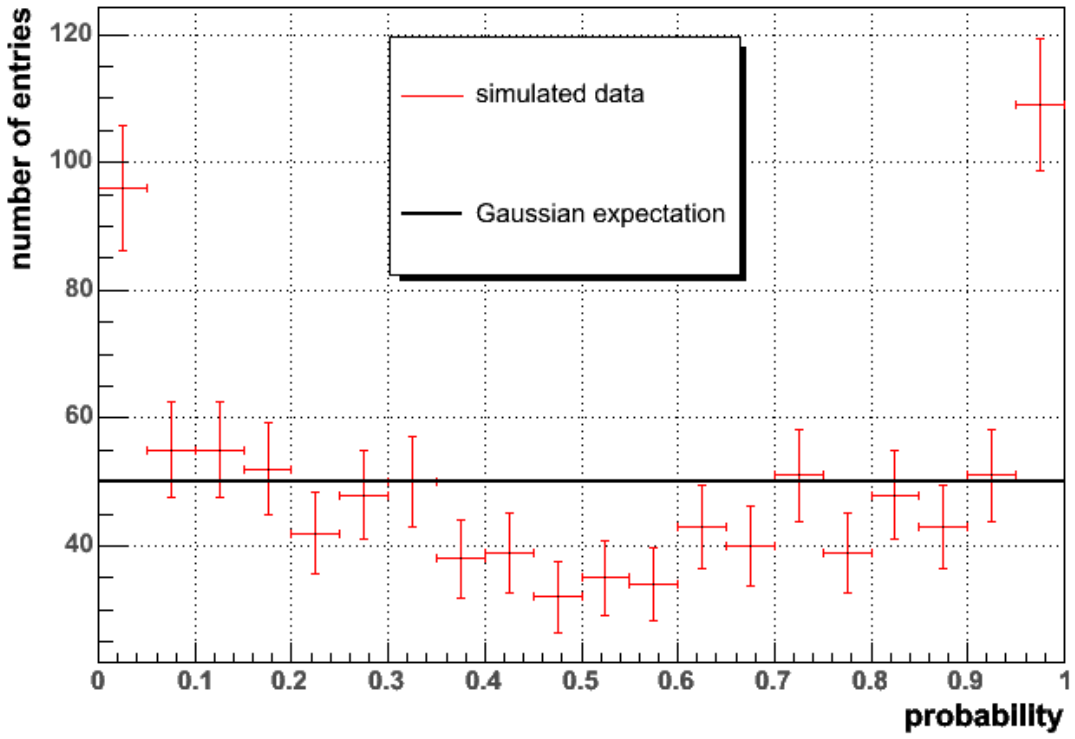

Figure 35: Distribution of the probabilities comparing two sets of 1000 atmospheric samples. The red crosses are the obtained numbers of the probabilities with the statistic spread as errors.

To find the multipole moments with the best sensitivity a χ^2-test is used:

$$\chi^2(l_{max}) = \sum_{l=0}^{l_{max}} \frac{(< C_{l,atms} > - C_l)^2}{\sigma^2_{l,atms}} \tag{70}$$

where l_{max} is the maximum used multipole moment, $< C_{l,atms} >$ is the mean of the 1000 atmospheric neutrinos simulations with the corresponding errors $\sigma_{l,atms}$ and C_l are the multipole moments of the test angular power spectrum.
The χ^2 are calculated for the mean of all 1000 simulated samples for each hypothesis. They show the systematic changes in the angular power spectrum free of statistical uncertainties. For the optimisation of the range of the multipole moments the probability that the χ^2 fits to the atmospheric spectrum is used. A high probability corresponds to a low sensitivity and a low probability to a high sensitivity.
The probabilities for the χ^2 values are cumulative for rising l_{max}. Falling probability for the step from l_{max} to $(l_{max} + 1)$ shows an increased sensitivity achieved by adding the multipole moment $(l_{max} + 1)$ to D^2 (and vice versa for rising probability). The intervals with falling probability should be used for the analysis.
These probabilities for $\chi^2(l_{max})$ are shown in figure 36 and 37. The corresponding figures for the other hypotheses can be found in appendix E.

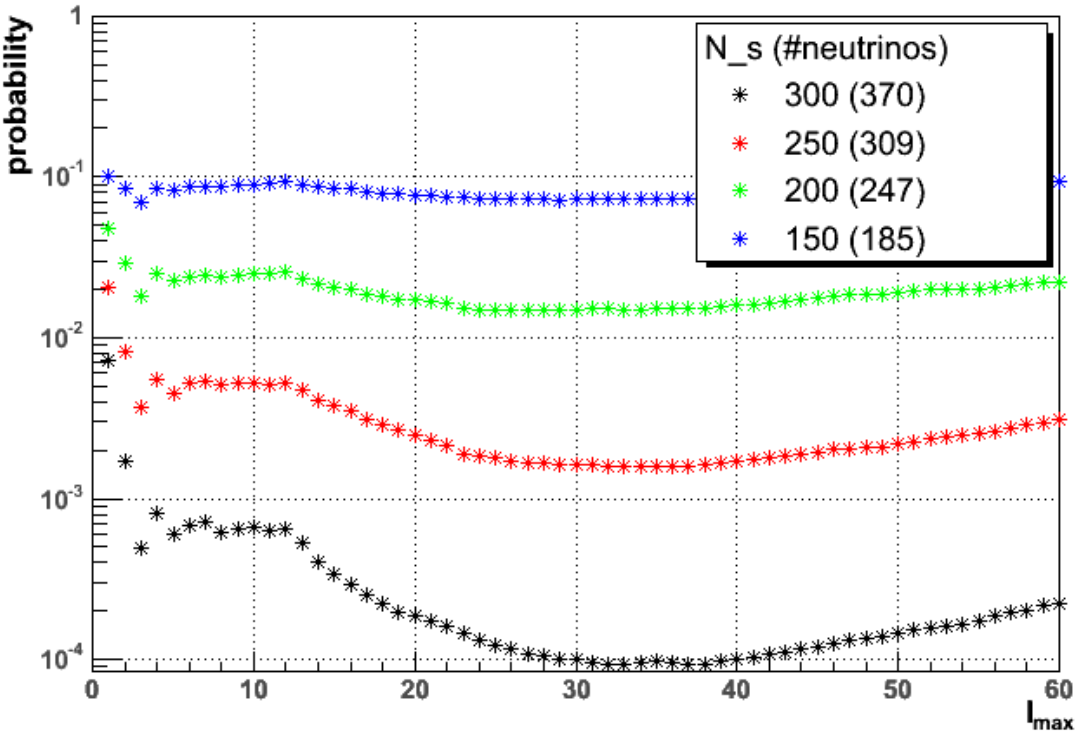

Figure 36: χ^2-probability for an angular power spectrum of mini sources ($\gamma = 2$ and $\mu = 3$) to appear as atmospheric background signal depending on the used multipole moments.

Figure 36 shows the probabilities for a signal from mini sources ($\gamma = 2$ and $\mu = 3$) to appear as background fluctuation for different numbers of events. The diagrams for the other isotropic sources are similar. The probabilities get smaller with rising signal strength. For a fixed strength the probabilities have three minima, two at $l_{max} = 3$ and 5 and a broad one is at $l_{max} = 30 - 40$. All remain stable with changing signal strength. Between $l_{max} = 4$ and 12 the probability does not change significantly.

Here, two optimum regions of the multipole index l are chosen. The first is at small multipole moments $l = 2, 3, 5$ and the second region is at $l = 13 - 40$.

From the angular power spectra (chapter 6.2) we know that the effect for large moments depend on the number of neutrinos per source μ. They are sensitive to strong mini sources independent of the energy spectrum. For the moments $2, 3$ and 5 the changes depend on the energy spectrum independent of the source strength μ. These moments show a good sensitivity for $\gamma = 2$ but not for $\gamma = 2.5$. The here defined regions separate these effects.

Additionally, for all mini and micro sources the interval from $l = 1 - 40$ is used, so no information gets lost. An unexpected phenomenon giving deviations in $l = 6 - 12$ would be included here.

Figure 37 shows probabilities for the sources in the galactic plane ($\gamma = 2$ and $\mu = 3$). The probabilities for the other simulations of the galactic plane and the super galactic plane

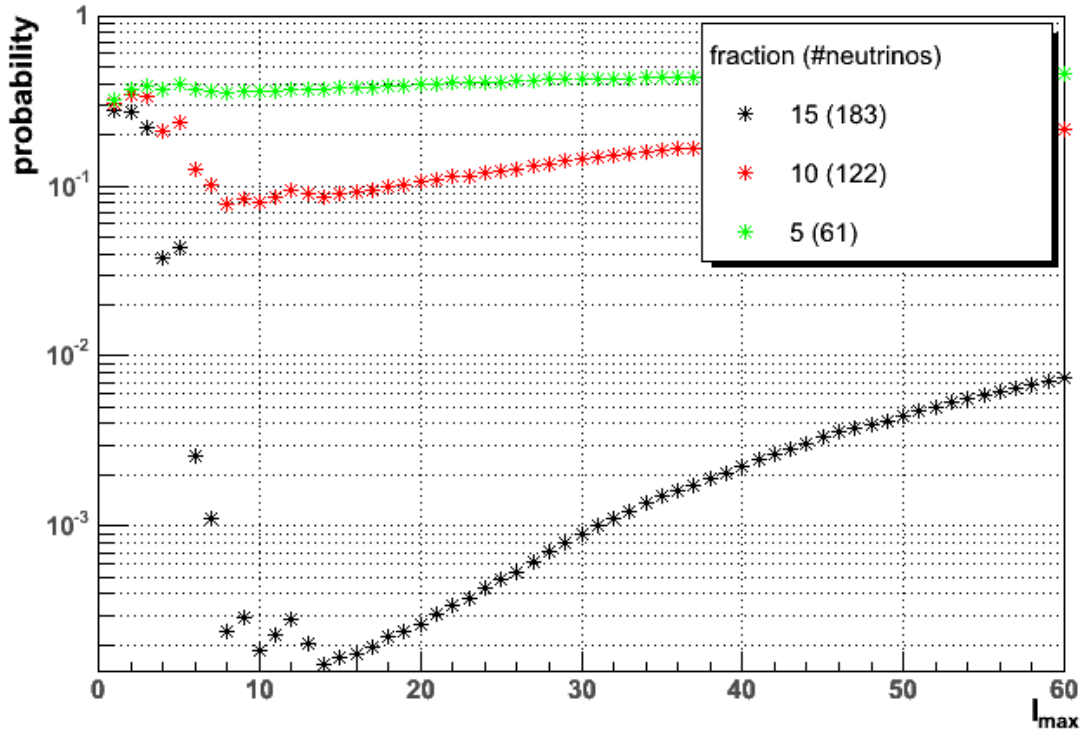

Figure 37: χ^2-probability for an angular power spectrum of the galactic plane with mini sources ($\gamma = 2$ and $\mu = 3$) to appear as atmospheric background depending on the used multipole moments.

are similar. For larger fractions the probability for the spectrum to be from atmospheric neutrinos decreases. A minimum is observed between $l_{max} = 10$ and 15, this minimum is stable with changing fractions of events from the plane.
Here, the optimum region is $l = 1 - 15$ the region of falling probability. The other parts of the spectrum are not used.
Finally, the region for neutrino oscillations has to be chosen. Here, no χ^2 values are calculated. By diagram 34 (with the multipole moments) a choice is obvious, $l = 2$ and 3. Only these two multipole moments change strongly due to oscillations. Other moments are not taken into account.
The defined ranges for the different hypotheses are listed in table 4.

6.5 Construction of Confidence Belts

The multipole moments are not distributed independently and Gaussian like(chapter 4.4 and 6.3). Thus, it is not possible to calculate limits for the different hypotheses directly. To determine these limits, confidence belts are calculated according to Feldman and Cousins unified approach [FC99].
For each hypothesis there exists one parameter that determines the signal strength. This

signal hypothesis	γ	μ	l range		
isotropic point sources	2	1	2,3,5		1-40
	2	2	2,3,5	13-40	1-40
	2	3	2,3,5	13-40	1-40
	2.5	1			
	2.5	2		13-40	1-40
	2.5	3		13-40	1-40
galactic plane with sources	2	2			1-15
	2	3			1-15
	2.4	2			1-15
	2.4	3			1-15
super galactic plane with sources	2	2			1-15
	2	3			1-15
	2.4	2			1-15
	2.4	3			1-15
galactic plane with cmbr	2.7	-			1-15
neutrino oscillation	-	-	2,3		

Table 4: Multipole moments with the optimum sensitivity for different hypotheses

is the number of sources N_s for the hypothesis with sources. For the galactic plane and the background it is the fraction f and for atmospheric neutrino oscillations parameter Δm^2 that determines the signal strength. N_s and f correspond to the number of neutrinos from extra-terrestrial sources used as observable. These are the values determined by the confidence belt.

After defining the intervals for the analysis, the D^2/dof[17] (equation 50) are calculated for all hypotheses (all parameters except N_s, f or Δm^2 fixed) and all ranges. The probability density function for the D^2/dof for each hypothesis is determined from the 1000 samples for each signal strength. Therefore, the number of D^2/dof values in different bins n is counted and the probability $P = n/1000$ is calculated. For one hypothesis and different signal strengths the same bins are chosen. The different signal strengths are taken into account by a ranking of the bins for different signal strength and the same D^2/dof. The bins with a high probability P get the highest priority. Afterwards, bins are collected for fixed signal strength (and variable D^2/dof) corresponding to this priorities until $\sum P = 0.9$. This procedure is described in [FC99].

As one example the confidence belt for mini sources (with $\mu = 3$ and $\gamma = 2$) for the range $l = 2, 3, 5$ is shown in figure 43. The other confidence belts are shown in appendix F.

Combining the D^2/dof from the measurement with the confidence belts yields the limit on the number of neutrinos from a hypothesis in the 4-year sample (or for Δm^2). The measured D^2/dof is drawn as line in the diagram with the confidence belt. The intersection with the borders of the 90% confidence region define the upper and lower limit. These limits have a 90% confidence. Included are the statistical uncertainties, the reconstruction error and the uncertainties in the atmospheric neutrino spectrum. Other systematic

[17] dof = degrees of freedom. Here, the number of multipole moments included in D^2

uncertainties are not included.
No limit is observed if the line does not cross the boundary. For each hypothesis and each multipole interval an upper limit is obtained for the number of neutrinos from sources with the given parameters.

7 Experimental Result

For the 4-year-sample (chapter 3.3.6) the same analysis steps are performed as for the simulated data samples. Note that a completely blind analysis has been performed; i.e. the full analysis has been exclusively developed with Monte Carlo. No change to the analysis has been applied after the "un-blinding" of the experimental data. Figure 38 shows the angular power spectrum compared to the atmospheric expectation.

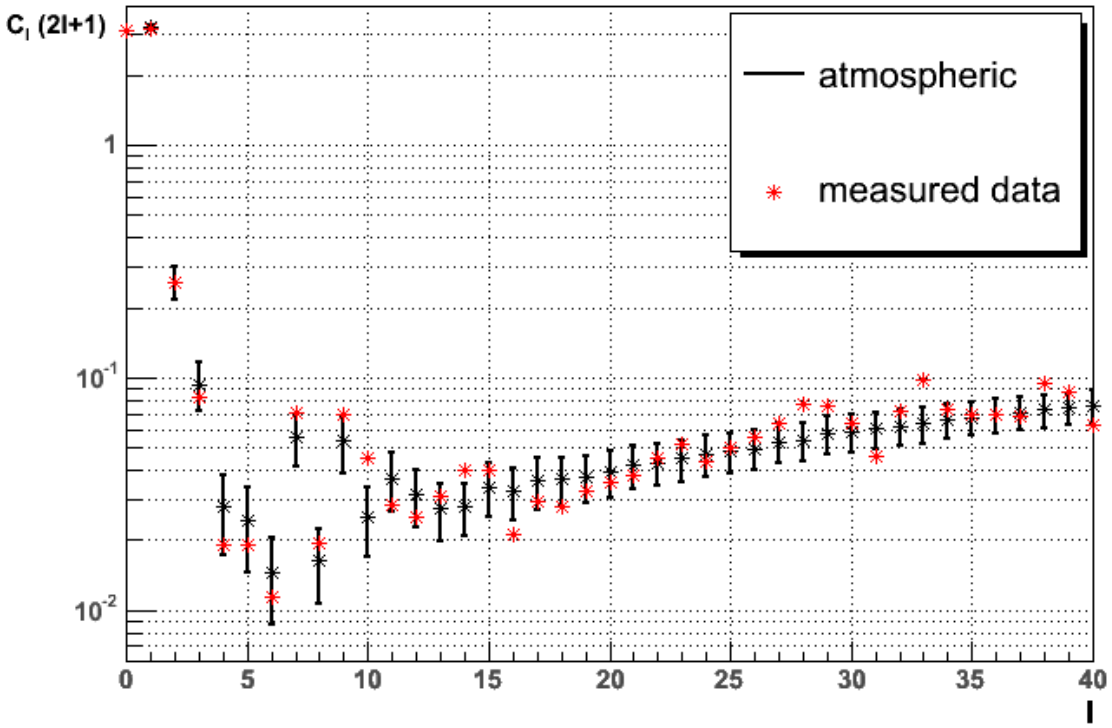

Figure 38: Angular power spectrum for the data Measured by AMANDA-II. The red stars are the measured power spectrum. The black stars are the expectation from the atmospheric neutrinos with error bars.

The power spectrum calculated from the 4-year sample fits well to the expectation of the atmospheric background. Deviations in many of the multipole moments exist. All of these deviations are consistent with the errors in the atmospheric expectation.
Another check of the statistical behaviour is done, a histogram for the size of the deviations in units of the corresponding error is created (figure 39) using the multipole moments from 1 to 50. The expected distribution is only approximately Gaussian because the multipole moments are weakly correlated and the distribution of the C_l has non-Gaussian tails (see figure 35).
The mode of the calculated distribution is below zero and the tail for a positive deviation is longer. The mean of the distribution is 0.2 ± 0.14 and the RMS is 1 ± 0.26.

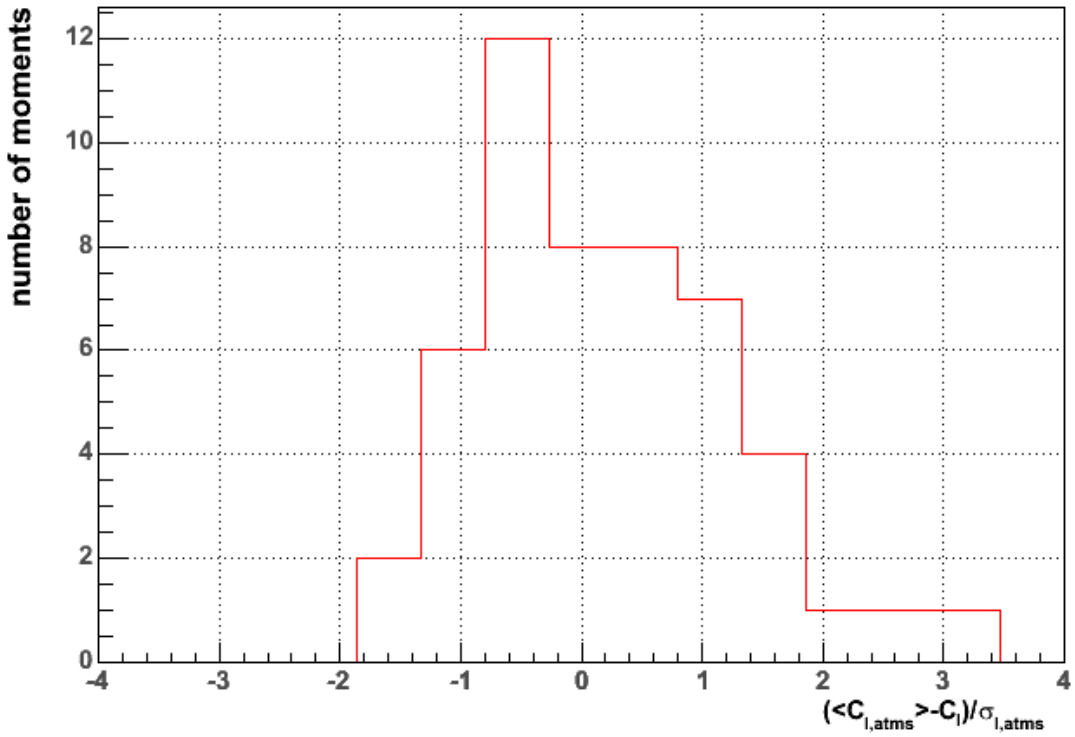

Figure 39: Distribution of deviations from the atmospheric expectation for the measured data for the multipole moments with $l = 1$ to 50.

The measured angular power spectrum fits well to that expected spectrum from the atmospheric background. No hint of a strong contribution from other sources is observed. Thus, the Monte Carlo provides a good description of the detector.
Applying the pre-defined ranges in l yields the D^2/dof values as given in table 4. The expectation for theses values is approximately 1.
In the following chapters the measured values for D^2/dof are used to set limits on the

range	D^2/dof
2,3	0.14
2,3,5	0.19
6-12	1.43
13-40	1.32
1-40	1.21
1-15	0.78

Table 5: D^2/dof for the 4-year-sample dependent on the ranges given for the different hypotheses (table 4)

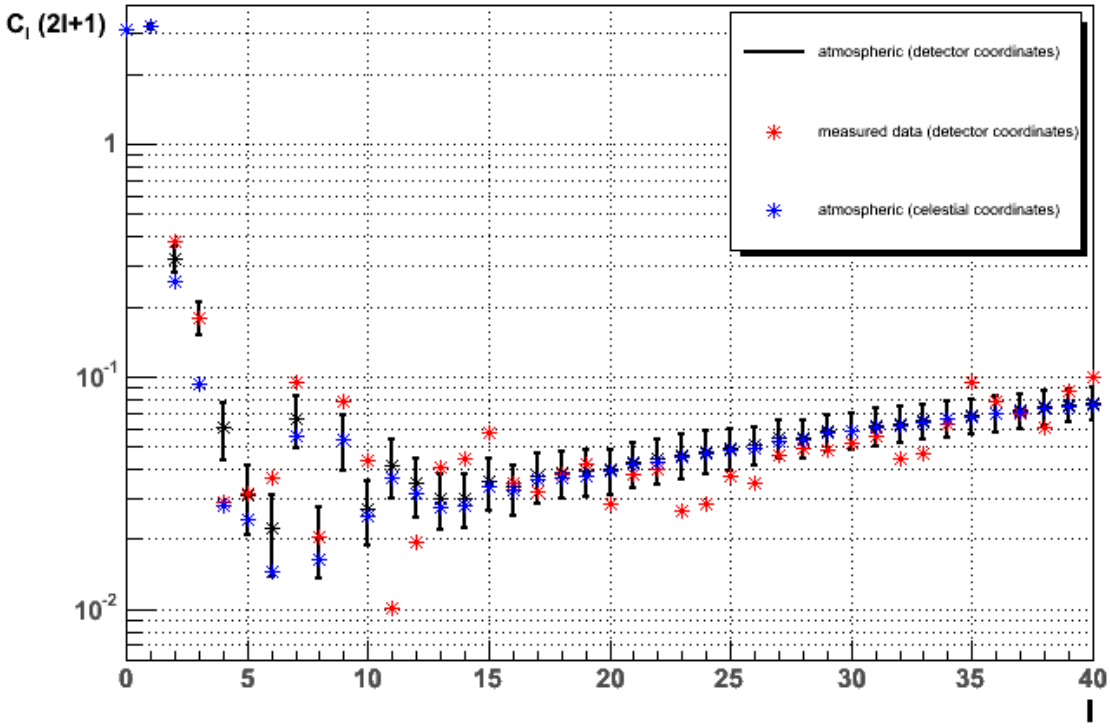

Figure 40: Angular power spectrum of the measured data in terrestrial coordinates. In black the expectation for atmospheric neutrinos is shown with the 1σ spread as error bars. The red dots show the spectrum from the experiment and the blue dots are the simulated spectrum for the atmospheric background in equatorial coordinates.

source hypotheses defined in chapter 2.4.

7.1 Analysis in Detector Coordinates

The comparison above is done in celestial coordinates. In this system extra-terrestrial objects have fixed positions. In order to test for detector effects terrestrial coordinates of fixed orientation with respect to the detector are used. In this system the extra-terrestrial objects are circulating while the detector is fixed. Therefore systematic effects according to the azimuth angle of the detector can be tested.
The same analysis as for celestial coordinates is performed. A simulation of the angular power spectrum for the atmospheric neutrinos in terrestrial coordinates is required. The relative detector acceptance is taken from the Monte Carlo and is applied in the same way to the simulated data sample as the zenith acceptance.
Figure 40 shows the mean angular power spectra for atmospheric neutrinos in terrestrial and celestial coordinates and the power spectrum calculated from the experimental data. The two simulated power spectra in terrestrial and celestial coordinates show large deviations in the multipole moments between $l = 2$ and 8. The other moments have nearly the

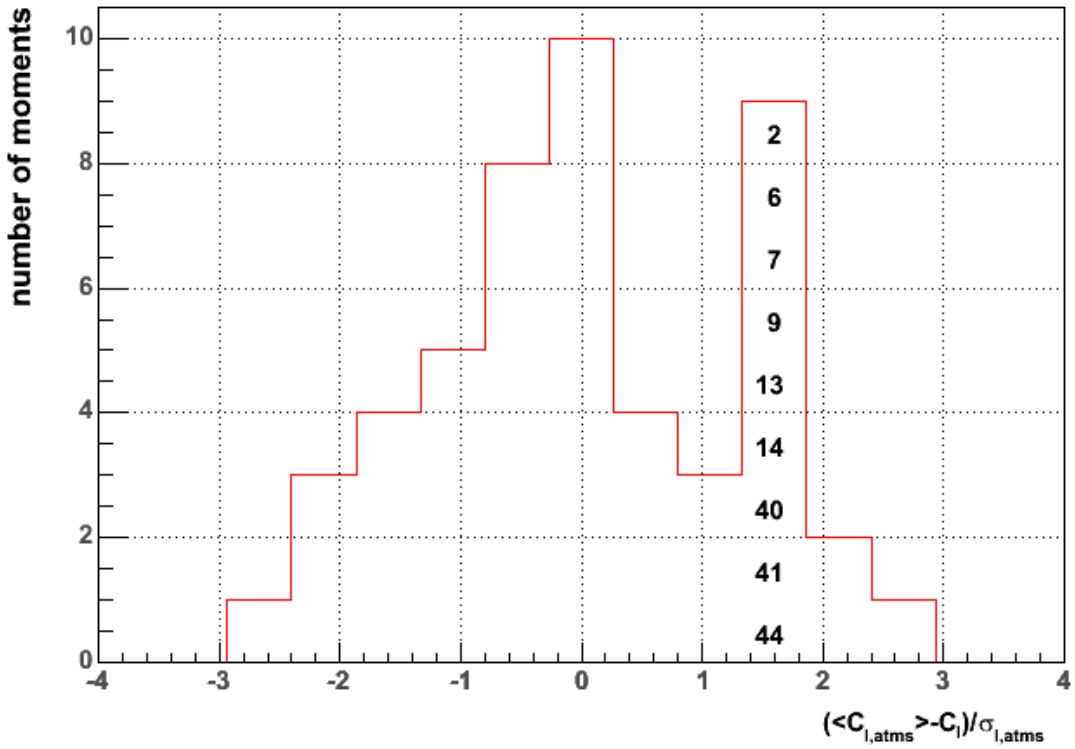

Figure 41: Distribution of deviations from the atmospheric expectation in celestial coordinates. The measured data for the multipole moments between 1 and 50 are used. The numbers in the peak give the included multipole moments in this bin.

same values. Most of the multipole moments are rising in terrestrial coordinates. This can be explained by the π-periodic structure in the azimuth angle acceptance of the detector, the spherical harmonics Y_l^m show such kind of structure for $m = 2$. The first affected multipole moment is $l = 2$ (due to $m \leq l$). Increasing l only changes the number of oscillations from the equator to the pole. Multipole moments with $l > 2$ also change because the detector acceptance depends on the zenith angle.
The spectrum of the experimental data in terrestrial coordinates fits well to the expectation from atmospheric neutrinos in this coordinates. (Note, in figure 40 the dots for the spectrum from the experimental data (red) correspond to one data sample, while the dots for the atmospheric spectrum in celestial coordinates (blue) represent the mean of 1000 data sets. A bigger spread is expected for the experimental data.) Figure 41 shows the histogram of the deviations.
A mean of about 0.04 ± 0.18 and a RMS of 1.3 ± 0.25 are observed. These values fit well to the expected statistical deviations. A further inspection of the error distribution shows an unexpected peak at about 1.6 standard deviations. 2/3 of the entries in this bin are from the first 15 multipole moments. For an estimation of about 3 entries and an observed number of 9 events, there is no significant difference. This can be explained by statistics but hints at a small azimuth angle dependent artefact.

In celestial coordinates deviations between the spectrum of the experimental data and the Monte Carlo data exist. The source of these deviations is the asymmetry of the detector acceptance in azimuth, however, more detail is not known. This effect has no influence on the analysis because it does not appear in the celestial coordinates.

8 Background from Mis-Reconstructed Muons

This chapter presents the results for events from mis-reconstructed down-going muons. The results provide a quality check for the data sample, because the fraction of mis-reconstructed events is an indication of the purity of the data set. The hypotheses from chapter 5.6 are listed here again:

(flat) 5% flat distribution in $\cos\theta$

(g90) 4% Gaussian distributed (width 5°) at the horizon (90° zenith angle) and 1% flat distributed in $\cos\theta$

(g105) 3% Gaussian distributed (width 8°) at 105° zenith angle and 2% flat distributed in $\cos\theta$

(g140) 5% Gaussian distributed (width 20°) at 140° zenith angle in $\cos\theta$

The limits from the confidence belts are finally given in numbers of background events or as fraction of the measured data set; 5% correspond to 166 events. Figure 42 shows the mean angular power spectra for the different hypotheses, the averaging is done over 1000 simulations.
For the flat distribution only small deviations from the atmospheric expectation are observed. However, this is not the case for the other hypotheses. The largest deviations occur for (g90), here deviations for multipole moments with an index smaller than $l = 21$ are observed. The multipole moments above $l = 9$ show an odd-even effect. For odd l the C_l are larger than expected from the atmospheric background while at even l no deviations or deviations to the other direction can be seen. For (g105) and (g140) large deviations for the multipole moments between $l = 1$ and 7 are seen. For larger l the deviations are small.
Also the directions of the deviations are interesting. While at large l all C_l from the hypotheses are equal or larger than the expectation, deviations at small multipole moments occur in different directions. This is explained by the minimum value $C_{min}(N_{tot})$ that GLESP can calculate (chapter 6.1). For the large l this minimum is already reached by the atmospheric expectation so the spectrum with the hypothesis cannot have a lower value. At small l the strongest deviations for (g140) are in the opposite direction to the deviations for the other hypotheses. This shows a principle difference in the zenith distributions. The hypotheses (flat), (g90) and (g105) produce an increase in the relative number of neutrinos near the equator. Here, the atmospheric expectation has the fewest events. The hypothesis (g140) increases the relative number of events closer to the pole with a corresponding loss in the region of the equator.
The analysis of the power spectra is expected to have a low sensitivity to a (flat) distribution of the mis-reconstructed down-going muons. The sensitivity is better for the distributions (g105) and (g140), where the first moments show deviations. The largest sensitive range is observed for (g90). This sensitivity also means that contributions from

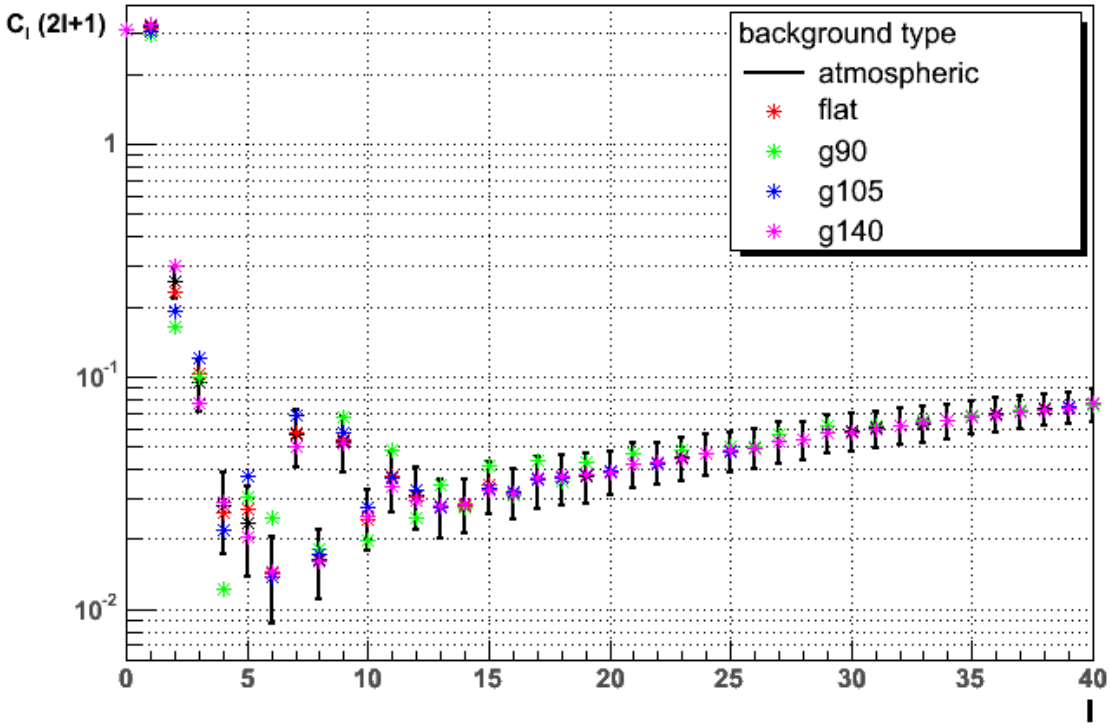

Figure 42: Angular power spectra for mis-reconstructed muons (5%). The black stars are the expectation from the atmospheric neutrinos with error bars and the coloured stars correspond to the different background hypotheses.

these backgrounds may influence the limits for the astrophysical hypotheses in these regions. Turning this argument around it is observed that for a contribution of less than 5% of background only angular distributions like (g90) can affect the search for extra-terrestrial signals.
Due to the differences in the sensitivity an optimisation of the range of used moments would have to be done for each hypothesis separately, but for comparison unified ranges are useful. The ranges from the isotropic point sources (chapter 6.4) include the largest number of multipole moments. Additionally, they nearly separate the range sensitive to all background hypotheses ($l = 1$ to 7) from the rest. It is useful to add the range $l = 6$ to 12 because it could be sensitive here. The ranges used are:

$$l = 2, 3, 5 \qquad l = 6 - 12 \qquad l = 13 - 40 \qquad l = 1 - 40\ . \tag{71}$$

For these ranges the confidence belts are calculated and the corresponding values from the experimental data are inserted to obtain the limits (appendix F). These are listed in table 6.
The result for the limits fits to the expectation from the sensitivity. For $l = 2, 3, 5$ limits are obtained for all hypotheses. The ranges $l = 6 - 12$ and $l = 13 - 40$ provide only a limit for the hypothesis with the peak at the horizon (g90). For the full range $l = 1 - 40$

	N_{tot}^{limit} (90% CL) for				N_{tot}^{limit}/N_{tot}
	$l = 2, 3, 5$	$l = 6 - 12$	$l = 13 - 40$	$l = 1 - 40$	best range
flat	440	-	-	-	0.13
g90	100	265	370	185	0.03
g105	167	-	-	320	0.05
g140	290	-	-	570	0.09

Table 6: Maximum numbers of events from mis-reconstructed down-going muons for different ranges with 90% CL. A "-" means that there no limit can be given. In the last colum the maximum fraction of events from the specified hypothesis is given.

limits are obtained for (g90), (g105) and (g140). These limits are less restrictive than the limits for the multipole moments with $l = 2, 3, 5$. If no limit is obtained in a range this shows that the sensitivity of this range (for a special hypothesis) is low and that the limit is above 20%[18] of the data sample (666 events). For each selected l-range (g90) has the smallest limit.
The upper limits on the event number of the complete range are higher than the results from the small moments. This can be understood by considering the combination of sensitive and insensitive multipole moments in the full range. For (flat) the limit at $l = 1 - 40$ exceeds the 20% and is not relevant.
The limits are small fractions of the 4-year-sample. For the flat distribution a fraction of 13% and for (g140) a fraction of 9% are observed. For the other hypotheses the results are even smaller. The peak at 105° (g105) is smaller than 5% of the data sample and for (g90) there are less than 3%.
A low event limit for a hypothesis does not imply a low probability. A calculation of the most probable background is done in the following sub-chapters.

Here, all results for the background hypotheses are zero and additionally upper limits are observed. The analysis has a low sensitivity to the hypotheses with limits larger than 5% (166 events). In the case of (g90) the background can be restricted to less than 3%.
At the regions, where no limit is obtained, this background has no influence on the results of the physics analysis in chapter 9. The region with the biggest influence is for the moments with $l = 2, 3, 5$.

8.1 Discrimination between the Hypotheses using D^2

In order to determine the preferred hypothesis for the mis-reconstructed down-going muons the measured data is compared with the hypotheses from mis-reconstructed down-going muons in simulations instead of the pure atmospheric neutrino spectrum. D^2 is calculated with the corresponding mean angular power spectrum. Small D^2 values represent a good consistency. Large values for D^2 correspond to a poor agreement, which can however still be due to statistical fluctuations.
For this calculation an assumption of the strength of the hypotheses has to be made. Two possible choices exist. One choice is to assume the same strength for all hypotheses (A),

[18] 20% is the maximum fraction simulated.

	D^2/dof for 5% (A)				N_{tot}^{limit}/N_{tot}	D^2/dof for N_{tot}^{limit}/N_{tot} (B)			
$l =$	$2,3,5$	$6-12$	$13-40$	$1-40$	best range	$2,3,5$	$6-12$	$13-40$	$1-40$
flat	0.59	1.63	1.35	1.29	0.13	2.60	1.75	1.31	1.51
g90	3.39	3.17	1.27	2.02	0.03	0.36	1.59	1.34	1.26
g105	2.66	0.94	1.35	1.38	0.05	2.66	0.94	1.35	1.38
g140	0.40	1.65	1.34	1.32	0.08	1.12	1.72	1.29	1.40
atms	0.19	1.43	1.32	1.21					

Table 7: Comparison of the different hypotheses for down-going muons. For the different models the D^2 values comparing the measured data to the mean of 1000 simulations are given for the different ranges. This is done for equal background strength and for the upper limit of the specific hypothesis.

ignoring the upper limits. In a second approach the upper limits are used for the strength (B). Both results are listed in table 7.

For D^2/dof with the equal strength assumption (A) the result fits the expectation; the range $l = 13-40$ has about the same value of D^2 for all hypotheses. The range $l = 1-12$ discriminates between the hypotheses. The hypothesis with the peak at the horizon (g90) is disfavoured, in agreement with the upper limit. The first multipole moments ($l = 2,3,5$) are most consistency with (flat) and (g140). For $l = 6-12$ the peak at 105° has the smallest limit. The complete range ($l = 1-40$) can be used to compare this first ranges ($l = 2,3,5$ and $l = 6-12$) due to the similar values in the last part $l = 13-40$. The (flat) hypothesis is most probable followed by (g140) and (g105). (g90) is strongly disfavoured.

With a background strength set by the upper limits (B) the results change. The values do not vary as much as the results for the equal strength. The region from $l = 13-40$ is also insensitive, as above. For the small multipole moments $l = 2,3,5$, the peak at the horizon (g90) is the most probable and for $l = 6-12$ the peak at 105° provides the best agreement. The flat distribution is disfavoured. For the full range $l = 1-40$ the peak at 90° has a small preference, followed by (g105) and (g140). The flat distribution has the lowest probability.
Comparing the D^2 values for the hypotheses (flat), (g90), (g105) and (g140) to the D^2 values from the pure atmospheric background (chapter 7 and again listed in table 7) indicates that only in one range $l = 6-12$ the hypothesis (g105) is preferred. At all other ranges the pure atmospheric background provides the best agreement.

From both assumptions ((A) and (B)) is the preferred hypothesis that no additional background contribution exists. The values for the different hypotheses (flat), (g90), (g105) and (g140) are too similar to prefer one of them.

8.2 Discrimination using the Predicted Signs of the Deviations

Another estimation of the favoured hypothesis can be provided by including the signs of the deviations $s_{l\ hypo}$. These $s_{l\ hypo}$ are given by the direction of the deviations of the hypotheses from the atmospheric expectation for each l (compare figure 38 and 42). The

	D^2/dof	$\widehat{D}^2/dof$				$(D^2-\widehat{D}^2)/dof$			
range		flat	g90	g105	g140	flat	g90	g105	g140
2,3,5	0.19	-0.19	-0.19	-0.19	0.19	0.38	0.38	0.38	0
6-12	1.43	1.03	-0.5	1.11	0.52	0.40	1.93	0.32	0.91
13-40	1.32	0.8	0.82	0.8	0.8	0.52	0.50	0.52	0.52
1-40	1.21	0.75	0.49	0.76	0.65	0.46	0.72	0.45	0.56

Table 8: Comparison values $\hat{D}^2/dof$ for the 4-year-sample to the signs of the background hypotheses (5%) dependent of the ranges given for the different hypotheses (table 4). The values for D^2/dof are taken from table 5.

new quantity $\hat{D}^2$ is defined by:

$$\widehat{D}^2 = \sum_{range} s_{l\ hypo} \frac{(< C_{l\ atms} > - C_l)^2}{\sigma^2_{l\ atms}} \text{signum}(< C_{l\ atms} > - C_l)\ . \tag{72}$$

The other symbols are the same as for D^2 (equation 50). $\widehat{D}^2$ is smaller than D^2 for data fitting to the prediction poorly. $\hat{D}^2$ remains nearly equal to D^2 for data fitting the hypothesis well. Numerically the agreement between each hypothesis and the data can be represented using the quantity $(D^2 - \widehat{D}^2)/dof$ (the degrees of freedom are the same for D^2 and $\widehat{D}^2$). A small value corresponds to a good fit. Table 8 shows the values for $\widehat{D}^2/dof$ for the measured data in comparison to the atmospheric neutrino prediction.
For the small multipole moments $l = 2, 3, 5$ the predicted signs are the same for the hypotheses with a flat distribution (flat), the peak at the equator (g90) and the peak at 105° (g105). It is not surprising to find identical values since for these multipole moments the predicted signs (in this region) are different to the deviations in the data. Only the hypothesis with the peak at 140° (g140) predicts the correct signs. For the larger multipole moments the values for (g140) are worse compared to the flat distribution (flat) and the peak at 105° (g105). The range between $l = 13 - 40$ has nearly the same values for all hypotheses, it has no distinguishing character. However, the value for the peak at the equator (g90) is the worst ($l = 1 - 40$). The best fit is achieved for (flat) and (g015).
The results are similar to the results for assumption (A) in the previous chapter. This is not surprising because backgrounds with the same strength are assumed here. This test gives no result for hypotheses with different strengths.
Also by this test it is not possible to give a preferred hypothesis for the additional background from mis-reconstructed down-going muons because the values are to similar to each other.

9 Extra-Terrestrial Fluxes

The measured deviations in the angular power spectrum (chapter 7) were found to be consistent with the hypothesis of atmospheric neutrinos and no additional contribution from extra-terrestrial sources.
In this section upper limits on the contribution from extra-terrestrial fluxes are calculated with a confidence level of 90%. This confidence includes the statistical and systematic uncertainties due to the atmospheric neutrino distribution and direction reconstruction. Effects from other possible sources are not included. These are mis-reconstructed down-going muons, other source hypotheses or neutrino flavour oscillations and systematic errors in the acceptance.
The value for each hypothesis is obtained independently from the other hypotheses. The results for the different hypotheses are discussed in the following sections.

9.1 Limits on Isotropic Mini and Micro Sources

For the hypotheses of isotropic mini and micro sources 90% limits are obtained from the confidence belts. These confidence belts are constructed according to the procedure described in chapter 6.5. An example confidence belt is shown in figure 43. (The other confidence belts are shown in appendix F.)
The results (table 9) for the different hypotheses show the expected behaviour (see chapter 6.2). Small multipole moments (range $l = 2, 3, 5$) are sensitive to the energy spectrum. For all hypotheses with $\gamma = 2$ approximately the same value is obtained, while for $\gamma = 2.5$ no limit can be set for this range (table 9). The small limits for the first multipole moments are a result of the small value of the measured D^2.
For the multipole range $l = 13-40$ the sensitivity depends on the number of neutrinos per source. For both spectral indices ($\gamma = 2, 2.5$) the upper limit gets lower with increasing number of neutrinos per source.
The complete range $l = 1 - 40$ has a dependence on both effects, the size of the limits changes with the spectral index γ and the number of neutrinos per source μ.

γ	μ	$N_{\nu\ tot}^{limit}$ (90% CL) for		
		$l = 2, 3, 5$	$l = 13 - 40$	$l = 1 - 40$
2	1	300	-	660
	2	345	785	560
	3	318	620	460
2.5	1	-	-	-
	2	-	825	775
	3	-	672	625

Table 9: Limits on neutrino numbers for isotropic mini and micro sources.
The parameter γ for the energy spectrum and μ for the source strength define the different hypotheses. $N_{\nu\ tot}^{limit}$ is the upper limit for the total number of neutrinos from one hypothesis in the full data sample of $N_\nu = 3329$ neutrinos at the given l ranges.

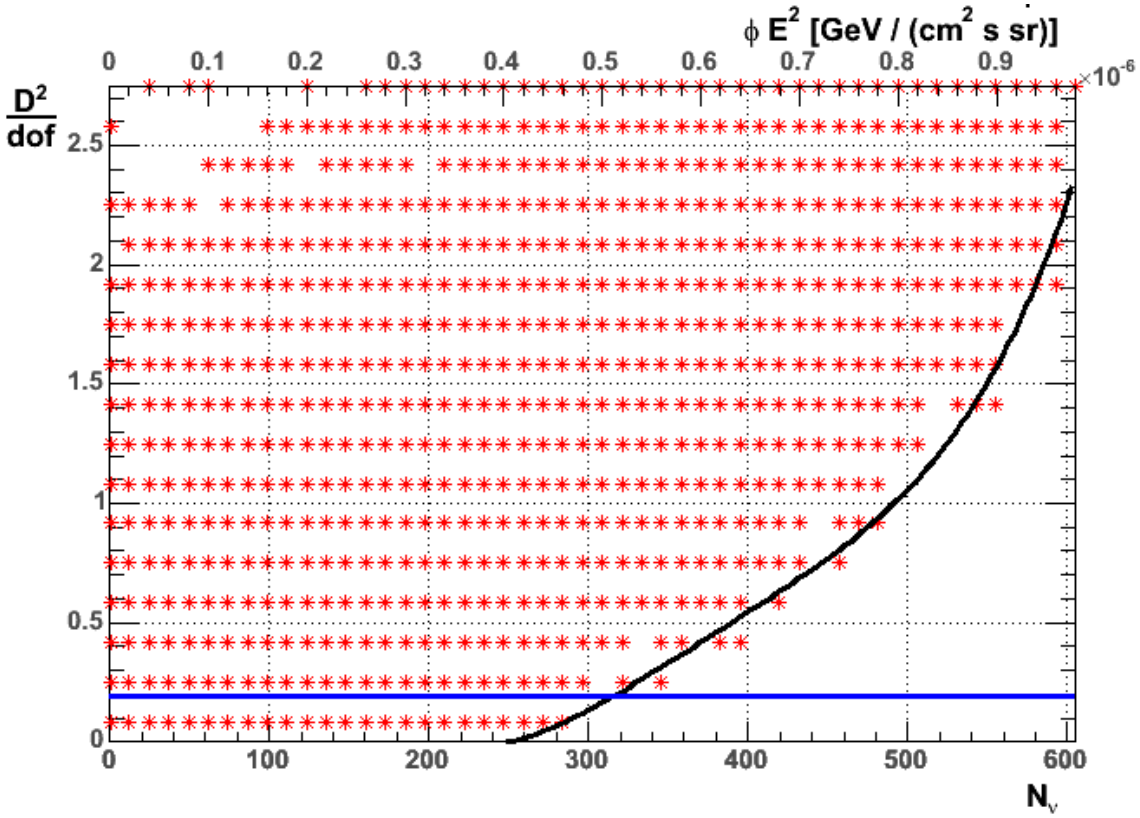

Figure 43: Confidence belt for mini sources with $\gamma = 2$, $\mu = 3$ and a range $l = 2, 3, 5$. The area with the red stars is the 90% confidence region, bordered by the black line. The blue line is the measured data ($D^2 = 0.19$). The intersection with the black line corresponds to the upper limit $N_{\nu\ tot}^{limit} = 318$.

For the further analysis the range with the highest sensitivity is used. This range ($l = 2, 3, 5$ for $\gamma = 2$ and $l = 1 - 40$ for $\gamma = 2.5$) also provides the smallest limits.
From chapter 6 is known that the range $l = 1 - 40$ includes a range with no sensitivity ($l = 6 - 12$) and a range with lower sensitivity ($l = 13 - 40$). The inclusion of these ranges would lead to results worse than if only the range $l = 2, 3, 5$ were used. If, however, the limits for the whole range $l = 1 - 40$ were unexpectedly bad this would be a hint that there is an unexpected effect in the experimental data.

The result of this procedure (table 9 and figure 44) is a limit of less than 350 neutrinos in the 4-year-sample from isotropic sources with a energy spectrum proportional to E^{-2}. These are less than 11% (90% CL) of the events in the 4-year-sample and is nearly independent of the source strength μ. Such a result is only achieved for $\gamma = 2$. For $\gamma = 2.5$ the sensitive range in l shows dependencies on the source strength and the limits depend on μ. Here the number of neutrinos is below 775 neutrinos for $\mu = 2$ and below 625 for $\mu = 3$.
So far all results are given in terms of neutrino numbers in the 4-year-sample. An upper limit for the number of neutrino sources and a limit on the diffuse flux are calculated in the following sections 9.1.1 and 9.1.2.

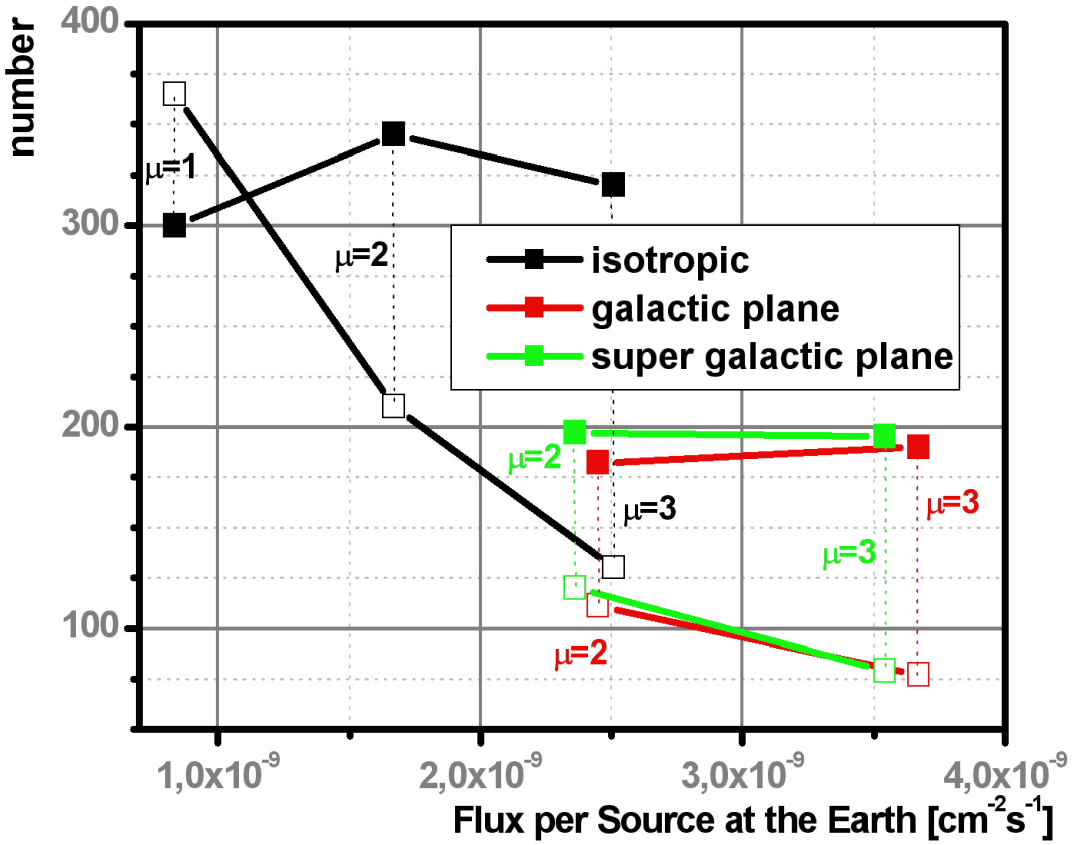

Figure 44: Upper limits on neutrino numbers (filled boxes) and source numbers (empty boxes) for different neutrino distributions and a E^{-2} energy spectrum. The black lines are the limits for the isotropically distributed sources. The red and green data points correspond to sources in the galactic plane and in the super galactic plane respectively.

For the absolute flux normalisation the detector acceptance is determined from the Monte Carlo data set. With this it is possible to calculate the mean flux per source at the Earth ϕ_{source} corresponding to the number of neutrinos per source in the 4-year-sample μ.

$$\frac{d\phi_{source}}{dE} E^{\gamma} = 2\pi \mathrm{sr} \epsilon_{\gamma} \mu \phi_0 \tag{73}$$

where $\phi_0(\gamma)$ is the flux per observed neutrino calculated in $\mathrm{GeV}^{\gamma-1}\mathrm{cm}^{-2}\mathrm{sr}^{-1}\mathrm{s}^{-1}$ from Monte Carlo data, it depends on the power index γ. ϵ is a factor due to the simulation technique (chapter 5) and the factor 2π sr results from an integral over the half sphere. Additionally it is useful to calculate the total flux per source using:

$$\phi_{source} = \int dE \frac{d\phi_{source}}{dE} \ . \tag{74}$$

The integration is done for energies above 10 GeV, both values are listed in table 10.

9.1.1 Limits on the Number of Point Sources

From the limit obtained on the number of neutrinos in the 4-year-sample a limit on the number of sources in the half sky is calculated using:

$$N_{sources}^{limit} = \frac{N_{\nu\ tot}^{limit}}{\mu\epsilon_\gamma} \tag{75}$$

where ϵ_γ is a parameter due to the simulation technique (chapter 5). Table 10 lists the values and figure 44 shows a diagram with the limit on the number of sources $N_{sources}^{limit}$ versus the total flux per source ϕ_{source}.
The number of allowed sources in the limit decreases with increasing source strength. E.g. for micro sources ($\mu = 1$, $\gamma = 2$), less than 365 sources in the northern sky are allowed and for $\mu = 3$ less than 130 are allowed. The limits for the steeper spectrum with $\gamma = 2.5$ are larger. Here no limit is obtained for the micro sources ($\mu = 1$) and the limits for mini sources are: 555 sources for $\mu = 2$ and 298 sources for $\mu = 3$.
The decrease of sources with rising source strength is explained by the $1/\mu$ dependence of the upper source limits on the neutrino limits. For the energy spectrum with $\gamma = 2.5$ the neutrino limit for $\mu = 3$ is smaller than the limit for $\mu = 2$. Thus, the limit on the source number becomes smaller.
The astrophysical interpretation of the limit on the number of sources is difficult because it is obtained under the assumption of a specific strength for all sources. This is unrealistic. What message does this limits provide?
For an energy spectrum with $\gamma = 2$ the final limit on the neutrino number is independent of the source strength (in the inspected range). The limit of ~ 350 neutrinos would be similar for any distribution of strengths between $\mu = 1$ and 3.
The situation for $\gamma = 2.5$ is more difficult to interpret. Here the observed limits on the number of neutrinos depends on the source strength. However, a weak source has a smaller contribution for the same multipole moments as a strong source. It is expected that the limits decrease for a mixture of different strengths.

9.1.2 Limits on the Diffuse Flux

From the measured neutrino number a diffuse flux limit $d\phi/dE$ can also be derived, the flux per observed neutrino ϕ_0 is used (see equation 73). The diffuse flux is:

$$\frac{d\phi}{dE} E^\gamma = N_{\nu\ tot}^{limit} \phi_0 \ . \tag{76}$$

$N_{\nu\ tot}^{limit}$ is the observed neutrino limit given in table 9. The values for diffuse flux are shown in table 10.
For an energy spectrum with $\gamma = 2$ the upper limit for the diffuse flux is $d\phi/dE\ E^2 \leq 5.6 \cdot 10^{-7}$ GeV cm^{-2}s^{-1}sr^{-1}, nearly independent of the flux per source ϕ_{source}. The diffuse flux for the energy spectrum with a power of $\gamma = 2.5$ is larger than that for $\gamma = 2$. Here, the upper limit is $d\phi/dE\ E^{2.5} \leq 1.6 \cdot 10^{-4}$ GeV$^{1.5}$cm^{-2}s^{-1}sr^{-1}.
The different scale of the upper flux limits appears due to the smaller detector acceptance at low energies. Thus, the same number of neutrinos in the 4-year-sample for both energy spectra would be produced by fluxes of different sizes.

γ	μ	<flux/source> $d\phi_{source}/dE\ E^{\gamma}$	ϕ_{source}	$N^{limit}_{sources}$ (90% CL)	flux $d\phi/dEE^{\gamma}$
2	1	$8.37 \cdot 10^{-9}$	$8.37 \cdot 10^{-10}$	365	$4.86 \cdot 10^{-7}$
	2	$1.67 \cdot 10^{-8}$	$1.67 \cdot 10^{-9}$	210	$5.59 \cdot 10^{-7}$
	3	$2.51 \cdot 10^{-8}$	$2.51 \cdot 10^{-9}$	130	$5.18 \cdot 10^{-7}$
2.5	1	$9.17 \cdot 10^{-7}$	$2.90 \cdot 10^{-8}$	-	-
	2	$1.83 \cdot 10^{-6}$	$5.80 \cdot 10^{-8}$	555	$1.62 \cdot 10^{-4}$
	3	$2.75 \cdot 10^{-6}$	$8.70 \cdot 10^{-8}$	298	$1.31 \cdot 10^{-4}$

Table 10: Limits on source numbers and neutrino flux from isotropic mini and micro sources. The parameter γ of the energy spectrum and μ define the different hypotheses. In the 3rd colum <flux/source> expresses the mean flux per source reaching the earth. Here the differential flux $d\phi_{source}/dE\ E^{\gamma}$ is given in $\mathrm{GeV}^{\gamma-1}\mathrm{cm}^{-2}\mathrm{s}^{-1}$ and the total flux ϕ_{source} in $\mathrm{cm}^{-2}\mathrm{s}^{-1}$. $N^{limit}_{sources}$ is the upper limit on the number of sources in the northern sky. The flux ϕ is the diffuse flux in $\mathrm{GeV}^{\gamma-1}\mathrm{cm}^{-2}\mathrm{s}^{-1}\mathrm{sr}^{-1}$.

Limits on the diffuse flux obtained from a dedicated analysis of AMANDA-II data do exist already. The actual upper limit is [IC05]:

$$\frac{d\phi}{dE}E^2 = 2.6 \cdot 10^{-7}\frac{\mathrm{GeV}}{\mathrm{cm}^2\ \mathrm{sr}\ \mathrm{s}}\ . \tag{77}$$

This is about a factor 2 better than the result obtained in this analysis. Additionally for the result given above only the AMANDA-II data of the year 2000 is used. A better limit for the full data is expected. However, the method used in this analysis is largely complementary to the direct one used to obtain the diffuse limit. The result can thus be interpreted as an independent confirmation of the limits obtained by the direct analysis.

9.2 Limits on Mini Sources in the (Super-) Galactic Plane

For neutrino sources in the galactic plane the confidence belts are created as described in chapter 6.5, and the results are shown in appendix F. Here, only one range $l = 1 - 15$ is used (chapter 6). Table 11 shows the upper limits obtained for the number of neutrinos from the planes in the 4-year-sample.
The limits on the neutrino numbers are less than 200 neutrinos and show only weak dependencies on the different hypotheses. The upper limits for the steep spectrum, with $\gamma = 2.4$ are smaller than the corresponding values for $\gamma = 2$. Another effect is that the limits for the super galactic plane are somewhat larger than the corresponding limits for the galactic plane (table 11).
The weak dependence of the upper limits on γ and μ is expected due to the similar angular power spectra; they are dominated by the shape of the plane.
The difference in the limits between the galactic and the super galactic plane is small but it can be an effect due to the different positions of the two planes in the sky. This produces a small difference because the detector does not have the same acceptance for different zenith angles. Neutrinos from the super galactic plane have a larger maximum

γ	μ	$N_{\nu\ tot}^{limit}$ (90% CL) for gal. pl.	super gal. pl.
2	2	182	197
	3	190	195
2.4	2	168	175
	3	172	178

Table 11: Limits on the number of neutrinos for mini and micro sources in the galactic and super galactic planes.
The parameters γ of the energy spectrum and μ define the different hypotheses. $N_{\nu\ tot}^{limit}$ is the upper limit for the total number of neutrinos from one hypothesis in the full data sample of $N_\nu = 3329$ neutrinos.

.

zenith angle ($\approx 74°$ in equatorial coordinates) than the neutrinos from the galactic plane ($\approx 63°$).
The limits on the number of neutrinos for both planes are about a factor 1.7 lower than for the isotropic distribution of the sources (see table 9). The effective sky coverage of the two planes is $A_{cov} = 0.0038 \cdot 2\pi$. The covered part of the sky by both planes is the same. Thus, the sources in the planes are located in a small part of the sky compared to the isotropic distributed sources. This creates additional angular structures leading to smaller upper limits on the neutrino numbers.
The limits on the number of sources in the (super-) galactic plane are calculated in section 9.2.1 and the corresponding values for a diffuse flux from the planes in section 9.2.2.
The mean flux at the Earth is determined from μ. This is done similar to equation 73 and 74[19]. The values for the differential flux $d\phi_{source}/dE$ and for the total flux ϕ_{source} are given in table 12.
The results for the mean flux per source are different to the corresponding results from the isotropically distributed point sources. This is explained by the angular dependent detector acceptance (figure 19 to 22) in combination with the anisotropic event distribution due to the description of the (super-) galactic plane. Thus, $\phi_0(\gamma)$ in equation 73 depends on the distribution of the neutrinos in the sky and is calculated separately for both planes from the Monte Carlo data set by re-weighting the events. The calculation is described in appendix B.

9.2.1 Limits on the Number of Point Sources in the (Super-) Galactic Plane

The upper limit on the number of sources $N_{sources}^{limit}$ in the (super-) galactic plane is calculated in the same way as the limit for isotropically distributed point sources (equation 75). The results are listed in table 12 and are shown in figures 44 and 45.
The number of sources is below 120 for $\mu = 2$ and below 81 for $\mu = 3$. These results are nearly independent of the choice of the plane and the energy spectrum.
The smaller upper limits for stronger sources $\mu = 3$ results from the similar upper limits on the neutrino number and the $1/\mu$ dependence in equation 75.

[19]The integration in equation 74 is again done for $E > 10$ GeV.

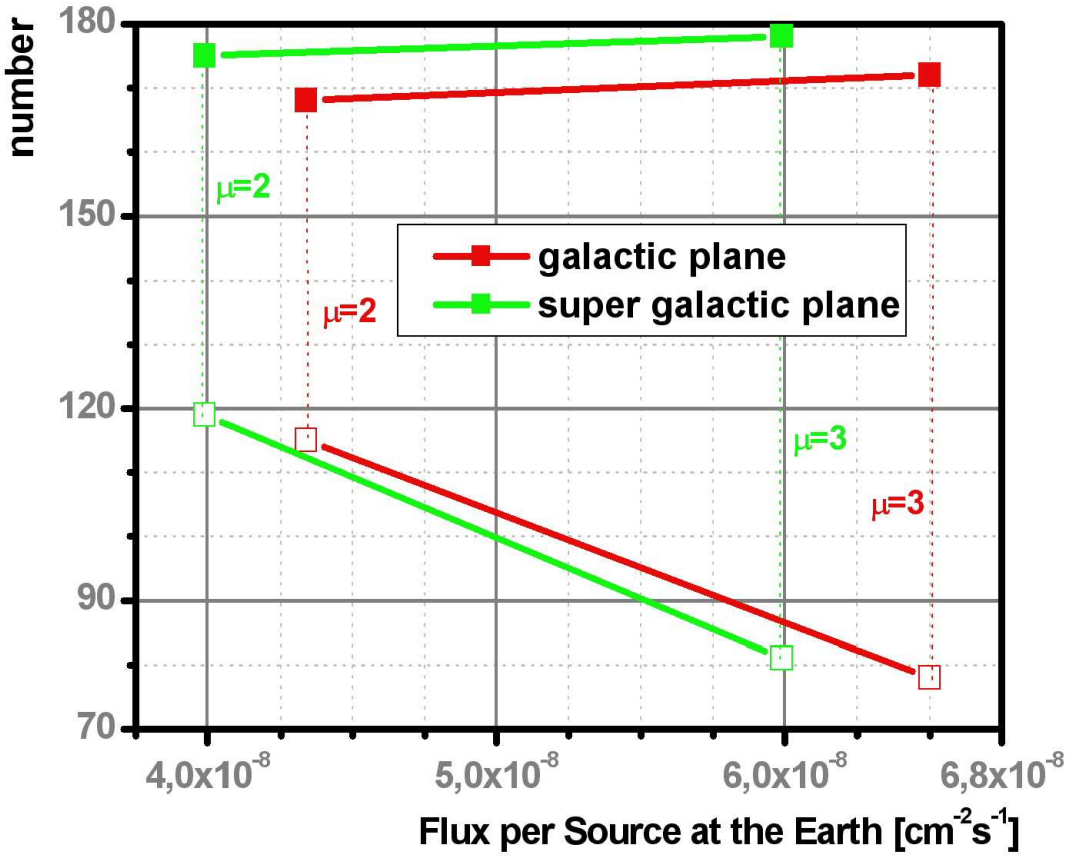

Figure 45: Limits on the number of neutrinos (filled boxes) and the number of sources (empty boxes) for sources in the (super-) galactic plane and a $E^{-2.5}$ energy spectrum.

A comparison of the limits on the number of sources in the planes and on the number of isotropically distributed sources (table 10) shows the same factor of about 1.7 as the limits for the neutrino numbers.

9.2.2 Limits on the Diffuse Flux from the (Super-) Galactic Plane

The diffuse flux from the (super-) galactic plane is calculated analogously to equation 76. Here, the fraction of the half sphere covered by the (super-) galactic plane $A_{cov} = 0.0038 \cdot 2\pi$ is included.

$$\frac{d\phi_{pl}}{dE} E^{\gamma} = N_{\nu\ tot}^{limit} \phi_0(\gamma) \frac{2\pi}{A_{cov}} \tag{78}$$

Again $\phi_0(\gamma)$ depends on the distribution of the sources in the sky and is different for both planes. It is calculated from the Monte Carlo data set by re-weighting (appendix B). Table 12 shows the obtained limits on the flux.

For an energy spectrum with $\gamma = 2$ and for both planes an upper limit of $d\phi_{pl}/dE\ E^2 < 2.8 \cdot 10^{-5}$ GeV cm^{-2} s^{-1} sr^{-1} is obtained. The corresponding value for the steeper spectrum, with $\gamma = 2.5$, is $d\phi_{pl}/dE\ E^{2.4} < 3.2 \cdot 10^{-3}$ GeV$^{1.4}$cm^{-2} s^{-1} sr^{-1}.

γ	μ	<flux/source> $d\phi_{source}/dE\ E^{\gamma}$	ϕ_{source}	$N^{limit}_{sources}$	$d\phi_{pl}/dE\ E^{\gamma}$
		galactic plane			
2	2	$2.45 \cdot 10^{-8}$	$2.45 \cdot 10^{-9}$	111	$2.71 \cdot 10^{-5}$
	3	$3.67 \cdot 10^{-8}$	$3.67 \cdot 10^{-9}$	71	$2.83 \cdot 10^{-5}$
2.4	2	$1.09 \cdot 10^{-6}$	$4.34 \cdot 10^{-8}$	115	$3.14 \cdot 10^{-3}$
	3	$1.63 \cdot 10^{-6}$	$6.50 \cdot 10^{-8}$	78	$3.22 \cdot 10^{-3}$
		super galactic plane			
2	2	$2.36 \cdot 10^{-8}$	$2.36 \cdot 10^{-9}$	120	$2.82 \cdot 10^{-5}$
	3	$3.54 \cdot 10^{-8}$	$3.54 \cdot 10^{-9}$	79	$2.79 \cdot 10^{-5}$
2.4	2	$1.00 \cdot 10^{-6}$	$3.99 \cdot 10^{-8}$	119	$3.01 \cdot 10^{-3}$
	3	$1.50 \cdot 10^{-6}$	$5.99 \cdot 10^{-8}$	81	$3.06 \cdot 10^{-3}$

Table 12: Limits on the number of sources and neutrino flux from mini and micro sources in the (super-) galactic plane. The parameter γ of the energy spectrum and μ define the different hypotheses. The values for the mean flux per source reaching the earth is given as differential flux in $\mathrm{GeV}^{\gamma-1}\mathrm{cm}^{-2}\mathrm{s}^{-1}$ and total flux in $\mathrm{cm}^{-2}\mathrm{s}^{-1}$. $N^{limit}_{sources}$ is the upper limit on the number of sources in the northern sky and the diffuse flux limit is $d\phi_{pl}/dE\ E^{\gamma}$ in $\mathrm{GeV}^{\gamma-1}\mathrm{cm}^{-2}\mathrm{s}^{-1}\mathrm{sr}^{-1}$.

It is possible to compare the diffuse flux from the isotropically distributed sources with the flux from the planes because both describe the neutrino limit per unit area. All upper limits on the diffuse flux from the planes are more than one order of magnitude larger than the corresponding diffuse limits for the isotropic sources (table 10). This is explained by the small fraction of the sky covered by the planes, included in the normalisation of the diffuse flux.

9.3 Neutrinos from Cosmic Ray Interactions in the Galactic Plane

The search for neutrinos from cosmic ray interactions in the galactic plane (chapter 2.4.5) is related to the search for a diffuse flux from that area with a spectral index of $\gamma = 2.7$. Here, only one confidence belt (chapter 6.5) is created with the range $l = 1 - 15$ (chapter 6) and is shown in appendix F. The result is an upper limit of:

$$N^{limit}_{\nu,cri} \leq 142 \qquad 90\%CL\ . \tag{79}$$

This limit is smaller than the limits on neutrino numbers from sources in the (super-) galactic plane (table 12). The existence of point sources means that a part of the power is concentrated at small angular scales and large l respectively. In the case of the diffuse flux all power goes to smaller l where this analysis is more sensitive.
The flux from the galactic plane is:

$$\frac{d\phi_{cri}}{dE} E^{2.7} \leq 3.42 \cdot 10^{-3} \mathrm{GeV}^{1.7}\mathrm{cm}^{-2}\mathrm{s}^{-1}\mathrm{sr}^{-1}\ . \tag{80}$$

The result is 3 orders of magnitude above the expected flux from the galactic plane of $10^{-6}\mathrm{cm}^{-2}\mathrm{sr}^{-1}\mathrm{s}^{-1}$ estimating a $E^{-2,7}$ spectrum (chapter 2.4.5). Thus, this analysis does

not have the sensitivity required to measure the flux of neutrinos from the interactions of cosmic rays with matter in the galactic plane, assuming the standard scenario.

The limit obtained here, is also about a factor seven worse compared to results from a direct search. An upper limit of 20 neutrinos from the galactic plane with a confidence of 90% is obtained [IC05] for the same data set. This is substantially better than the result of this analysis. However, as explained in the conclusion (chapter 12) substantial improvements are still possible for this analysis.

10 Limits on Neutrino Oscillations

The study of the neutrino oscillation hypothesis is different from all previous ones, because no astronomical sources are required here. As discussed in chapters 2.3.1, 5.5 and 6.5 the observable from the confidence belt (figure F.5) is the square mass difference Δm^2. An upper limit of:

$$\Delta m^2_{atms} < 4.8 \cdot 10^{-3} \text{ eV}^2 \qquad 90\% \text{ CL} \tag{81}$$

is obtained. This value has to be compared with the values from Super-Kamiokande (chapter 2.1.1):

$$1.3 \cdot 10^{-3} \text{ eV}^2 < \Delta m^2_{atms.} < 3 \cdot 10^{-3} \text{ eV}^2 \, . \tag{82}$$

The sensitivity on Δm^2 is smaller for this analysis and only an upper limit can be given. However as AMANDA-II was not designed to measure atmospheric neutrino oscillations, this result can be considered remarkably good.

11 Outlook to the IceCube Sensitivity

IceCube is the successor experiment of AMANDA. It is based on the same detection technique but it is larger by about a factor 100 (about 1 km^3 instrumented volume). The low energy threshold is larger because the distances between optical modules in IceCube are bigger. Interesting for this analysis is the expected higher event rate for atmospheric neutrinos. AMANDA-II triggers about 11000 "up-going" muon neutrino events per lifetime year [A+04] while IceCube is expected to have 0.8 million triggers from atmospheric neutrinos per year [Wi02]. The improvement of this analysis by the about 70 times higher statistic is discussed in the following.

The number of events affects this analysis in different ways. The maximum multipole moment l_{max} used for the analysis (compare chapter 6) is restricted by the area per source and the degrees of freedom. The limit is given by (in first order):

$$l_{max}^{dof} \propto \sqrt{N_{tot}} \qquad l_{max}^{angular} \propto \sqrt{N_{tot}} \; . \tag{83}$$

Both increase with the square-root of the number of events. The minimum value for the multipole moments that "GLESP" calculates is already given in equation (69):

$$C_{min} \propto \frac{1}{N_{tot}} \; . \tag{84}$$

The relative width of the C_l becomes smaller with rising statistics. The 1σ spreads corresponding to the statistical error are shown in figure 46 for different numbers of events. The spreads become smaller with rising statistic. For large multipole moments the error is proportional to $1/N_{tot}$. For high statistics the small multipole moments are dominated by the uncertainty in the distribution of the atmospheric neutrinos. Here the spreads decrease slower.
A mean multipole moment $< C_l^0 >$ for a sample with a signal can be given by:

$$< C_l^0 >=< C_{l,atms} > +\delta_l \; . \tag{85}$$

δ_l is the difference between the two mean spectra. The sensitivity s of the analysis can be expressed by:

$$s(N_{tot}) \sim \frac{\delta_l(N_{tot})}{\sqrt{\sigma^2_{l,atms}(N_{tot}) + (\sigma_l^0(N_{tot}))^2}} \; . \tag{86}$$

	r_s								
N_{tot}	$l=2$			$l=15$			$l=30$		
f_{sig}	0.37%	0.74%	1.11%	0.37%	0.74%	1.11%	0.37%	0.74%	1.11%
3329	1	1	1	1	1	1	1	1	1
9987	15.4	2.07	1.65	3.25	1.60	1.57	15.4	1.19	1.18
33290	32.1	2.61	2.00	5.39	2.13	1.76	46.4	1.6	1.34
99870	35.8	2.88	2.21	8.85	2.81	2.14	166	3.83	2.29

Table 13: Relative sensitivity depending on N_{tot} for chosen multipole moments.

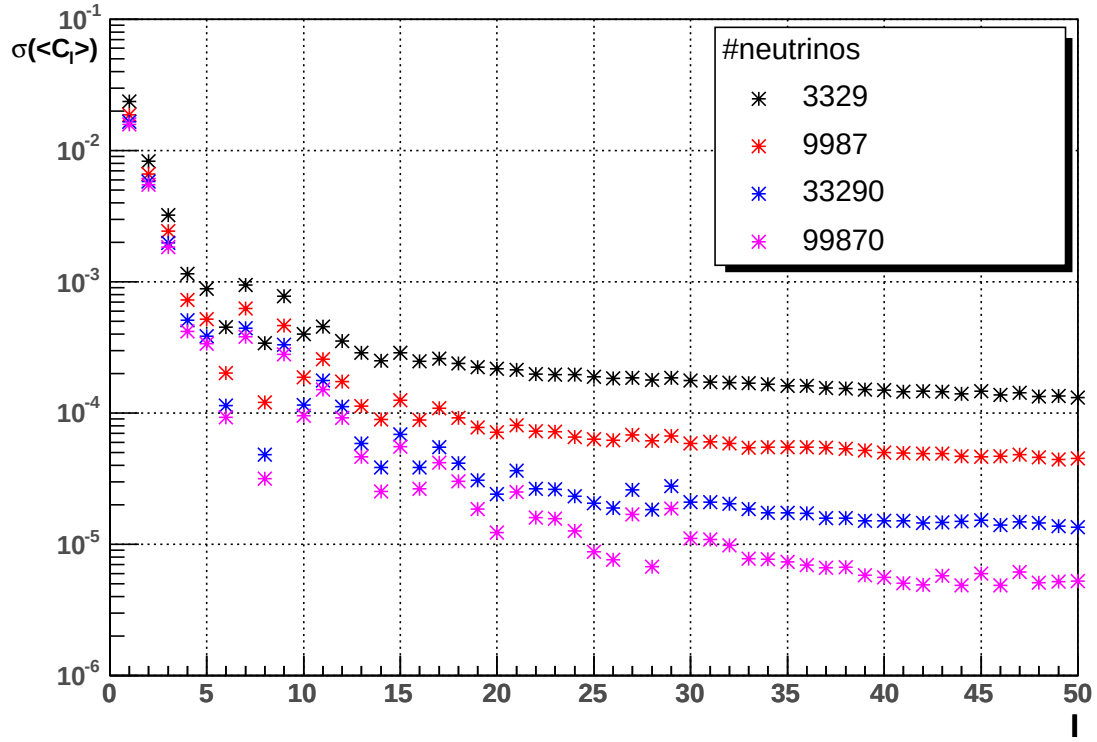

Figure 46: Spread of the multipole moments for atmospheric neutrinos depending on the number of events.

σ_l^0 is the statistical error of the mean $< C_l^0 >$ with a signal contribution determined from 1000 simulations. The relative improvement of the sensitivity with respect to AMANDA-II is given by:

$$r_s = \frac{s(N_{tot})}{s(N_{tot}^0)} \; . \tag{87}$$

$N_{tot}^0 = 3329$ is the number of events in the AMANDA 4-year-sample. The results are shown in table 13 and figures 47 to 49 for three specific multipole moments. Here, the relative signal fraction f_{sig} is fixed to the values 0.37%, 0.74% and 1.11% of N_{tot}; this corresponds to a constant signal.
In all cases the relative sensitivity rises faster for small signals ($f_{sig} = 0.37\%$). Only a small improvement is obtained for the larger signals.
With changing number of events the largest improvement is achieved between 3329 and about 10000 events. Here the errors are dominated by the statistics; Above the statistical uncertainty is not the main contribution to the error.
A large improvement for small signals is achieved by the higher statistics of the IceCube detector. In general the improvement depends strongly on the signal strength. This raise in the sensitivity for a single multipole moment must be combined with the larger number of available moments l_{max}.

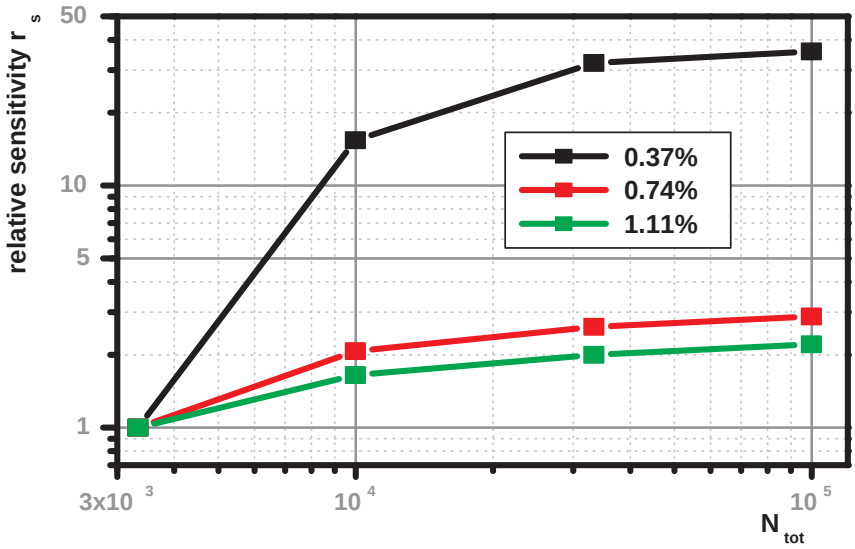

Figure 47: Sensitivity for l=2 versus the number of events.

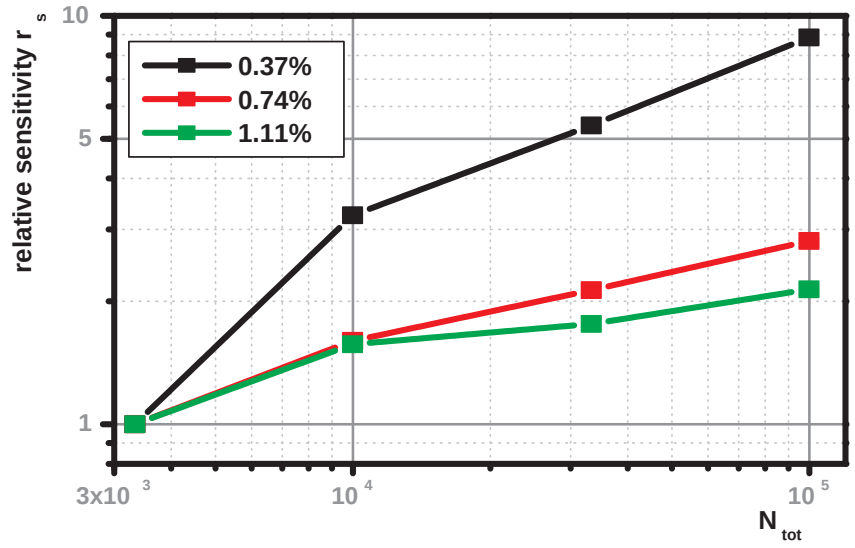

Figure 48: Sensitivity for l=15 versus the number of events.

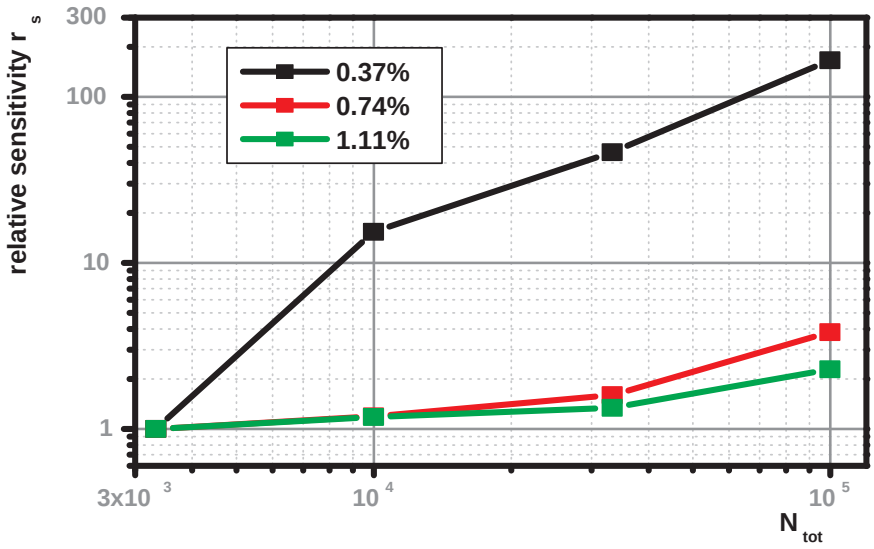

Figure 49: Sensitivity for l=30 versus the number of events.

12 Summary and Outlook

AMANDA-II is a neutrino telescope located at the South Pole. From the measurement during the years 2000-2003 a sky map with 3329 neutrino events from the northern sky was generated.
In this thesis a search for signatures of extra-terrestrial neutrinos is performed. This involves studying anisotropies in the sky distribution of neutrino directions by calculating the angular power spectrum. This method has already been used to analyse the anisotropies in the cosmic background radiation and is used here the first time for AMANDA-II data.
In order to find neutrinos from extra-terrestrial sources the angular power spectrum of the measured data is compared to the expectation from the atmospheric neutrino background. Different source types correspond to different structures in the power spectrum. The atmospheric neutrino background and all hypotheses for extra-terrestrial sources are simulated 1000 times to take statistical effects into account.
The result of the analysis is that the experimental data fits well to the assumption of atmospheric neutrinos. Here, no specific information about the source type is used and no contribution from any source is seen. No deviations due to reconstruction artefacts or other not understood detector effects are observed and the exhalent quality of the data set is verified in this way. An analysis for unexpected background sources finds no significant contamination of the data set and upper limits can be set in agreement with previous estimates. No definite statement about the distribution of remaining background events is possible.
For specific model assumptions, the contributions from extra-terrestrial sources can be quantitatively constrained. The limits for different possible sources are almost competitive to direct search methods. The limits for diffuse fluxes are only a factor 2 to 3 worse than the limits of the direct searches. For the weakest case (neutrinos from cosmic ray interactions in the galactic plane) the limit is larger by a factor 7. For each individual search a specialised analysis is thus more sensitive. However, the results achieved with this approach are complementary and provide independent proof.
The limits on the number of astrophysical sources of neutrinos in the northern sky are between 70 and 370 depending on the source strength. They are more difficult to interpret since the assumption of equal strength is not well motivated. Limits were obtained for isotropically distributed sources as well as for sources in the galactic and super-galactic planes.
A limit is also obtained for angular distortions due to neutrino oscillations: $\Delta m^2 < 4.8 \cdot 10^{-3}\mathrm{eV}^2$. This is a remarkable result because AMANDA-II was not designed for this measurement.
The limits presented here partially include systematic uncertainties. Uncertainties in the distribution of atmospheric neutrinos and statistical uncertainties in the Monte Carlo data set are taken into account as well as the finite detector resolution. Possible admixtures of different contributing source types are not included.

Different possibilities exist to improve this analysis. One possibility is to use a larger data sample as discussed above. Therefore additional AMANDA-II data from the year 2004 with 953 additional events could be used or the data from IceCube with two orders of magnitude higher statistics. It is shown in this thesis that for the high statistics with

IceCube, systematic errors would then dominate the sensitivity.
A second possibility for improvement is to exchange the discriminating quantity D^2 by a more sensitive one. For example the sign of the deviations or the behaviour of neighbouring multipole moments can be included. Also a Fischer-discriminant analysis could be applied. An optimised selection of the binning might further improve the sensitivity.

In this thesis the analysis of the neutrino sky-map was performed using a multipole analysis, a method new to this field and adapted from cosmology. It has been demonstrated that the application of this technique to the AMANDA-II data is possible. Doing so provides a new perspective on the detector systematics and the opportunity to gain insights in to the high energy neutrino sky.

Appendix

A Multipole Moments of the Half Sphere

It is difficult to calculate the multipole moments for a general function $f(\theta, \phi)$. One example can be calculated without difficulties. This is the half sphere:

$$f(\theta, \phi) = 1_{[0,\pi/2]}(\theta) \text{ with } 0 < \phi < 2\pi, 0 < \theta < \pi \ . \tag{88}$$

The following integral for the coefficients has to be evaluated:

$$a_{lm} = \int_\Omega f(\theta, \phi) \bar{Y}_l^m(\theta, \phi) d\Omega \ , \tag{89}$$

$$a_{lm} = \int_0^{2\pi} d\phi \int_0^\pi d\cos(\theta) f(\theta, \phi) \bar{Y}_l^m(\theta, \phi) \ . \tag{90}$$

The integration separates inserting the spherical harmonics Y_l^m (equation (51) and the function f. The integration over ϕ is done easily:

$$\int_0^{2\pi} e^{im\phi} d\phi = 0 \text{ for } m \neq 0 \text{ and } \int_0^{2\pi} d\phi = 2\pi \text{ for } m = 0 \ . \tag{91}$$

Thus, the second integral is only calculated for $m = 0$.

$$a_{l0} = 2\pi \sqrt{\frac{1}{2l+1}} \int_0^1 P_l(x) dx \qquad C_l = \frac{1}{2l+1} a_{l0} \tag{92}$$

The orthogonality relation (equation (55)) for $m = 0$ is:

$$2\pi \sqrt{\frac{1}{2l+1}} \sqrt{\frac{1}{2l'+1}} \int_0^\pi P_l(\cos\theta) P_{l'}(\cos\theta) d\theta = \delta_{ll'} \ . \tag{93}$$

With $P_l(-x) = (-)^l P_l(x)$ (from equation (54)) follows for even l:

$$\int_0^1 P_l(x) dx = \frac{1}{2} \left(\int_0^1 P_l(x) dx + \int_{-1}^0 P_l(x) dx \right) \propto \delta_{l0} \ . \tag{94}$$

All $a_{lm} = 0$ for l even and greater zero or $m \neq 0$. For $l = 0$ the result is $a_{00} = 2\pi$. For the other coefficients the integral must be solved:

$$a_{l0} = 2\pi \sqrt{\frac{1}{2l+1}} 2^{-l} \sum_{i=0}^{[l/2]} (-)^i \frac{[2(l-i)!]}{i!(l-i)!(l-2i+1)!} \ . \tag{95}$$

This description is not useful for programming, because it is not stable for large l. Thus, a recursive definition would be better. In [By59] can be found:

$$\int_0^1 P_l(x) dx = \frac{P_{l-1}(0) - P_{l+1}(0)}{2l+1} \ , \tag{96}$$

$$a_{l0} = 2\pi \sqrt{\frac{1}{2l+1}} \frac{P_{l-1}(0) - P_{l+1}(0)}{2l+1} \qquad l \quad \text{odd} \ . \tag{97}$$

The multipole moments for the half sphere are shown in figure 50 for $l = 1 - 40$. In this range the odd multipole moments can be described by a power law $C_l \propto l^a$, $a \sim -2.5$.

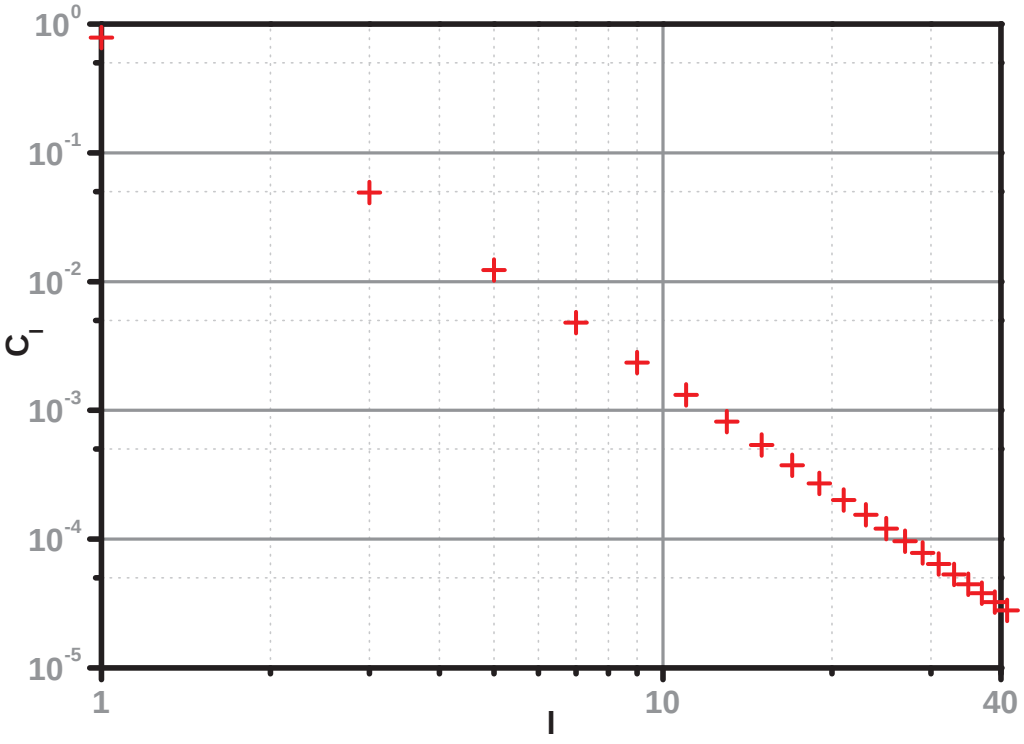

Figure 50: Odd multipole moments of the half sphere. The even moments with $l \neq 0$ are zero.

B Re-Weighting the MC for the (Super-) Galactic Plane

For the generation of neutrinos which are Gaussian distributed around the (super-) galactic equator with the Monte Carlo (described in 3.4) the events must be sorted and re-weighted. Simulated events have a zenith and azimuth angle but no right assertion. No time is set for the event. Since the detector is rotating the right ascension is thus free. In the Monte Carlo the weights for an isotropic sky distribution are included. To simulate events from the (super-) galactic plane the time is set so that all events originate from the (super-) galactic plane. Events in the pole region have to be discarded. After positioning the events in the plane they are re-weighted to obtain a flat distribution in the (super-) galactic longitude.
First, for each neutrino event the (super-) galactic longitude l is calculated:

$$\sin l = \pm \sin\theta \sqrt{1 - \cot^2\beta \cot^2\theta} \; . \tag{98}$$

Here l is given in degrees, θ is the zenith angle given from the Monte Carlo and β is the highest angle of the (super-) galactic plane in equatorial coordinates. (In numbers: $\beta \approx 63°$ for the galactic plane and $\beta \approx 74°$ for the super galactic plane.) This equation can be easily obtained by rotations. The different signs correspond to the two possible solutions for each zenith angle. A random sign is chosen for each direction. For neutrinos with a zenith angle θ larger than β the root is imaginary and no right assertion is calculated. These events cannot be shifted to the (super-) galactic plane and receive the weight zero. Skipping these events reduces the initial number of neutrino events in the Monte Carlo. The number of events is:

$$\bar{N}_{MC} = N_{MC} \sin\beta \; . \tag{99}$$

N_{MC} is the number of events in the Monte Carlo and $\bar{N}_{MC}$ the effective number.
In the Monte Carlo the events are isotropically distributed.

$$dn/d\cos\theta = C \tag{100}$$

C is a not specified constant. A weight $w(\cos\theta)$ for an flat sky distribution in (super-) galactic longitude has to fulfil:

$$\frac{dn}{dl} w(\cos\theta) = C \; . \tag{101}$$

Comparing both equations gives the weight w:

$$w(\cos\theta) = \frac{dl}{d\cos\theta} \; . \tag{102}$$

With equation (98) this leads to:

$$w(\cos\theta) = \pm \sqrt{\frac{1 + \cot^2\beta}{1 - (1 + \cot^2\beta)\cos^2\theta}} \; . \tag{103}$$

This is the weight added to the isotropic weight for each event to get Monte Carlo data for the (super-) galactic plane together with the correction of the number of events given by equation (99).

C Table of factors for the relative acceptance

γ	ϵ
2	0.8230
2.4	0.7329
2.5	0.6988
2.7	0.6449

Table 14: ϵ depending on different γ. The zenith angle distributions for the detector efficiency are normalised to a maximum of 0.95, this leads to an integral which is not one. Thus only a fraction of the neutrinos is accepted. This fraction is given by ϵ for isotropically distributed neutrino directions.

D Angular Power Spectra for the Different Hypotheses

D.1 Isotropic Micro and Mini Sources

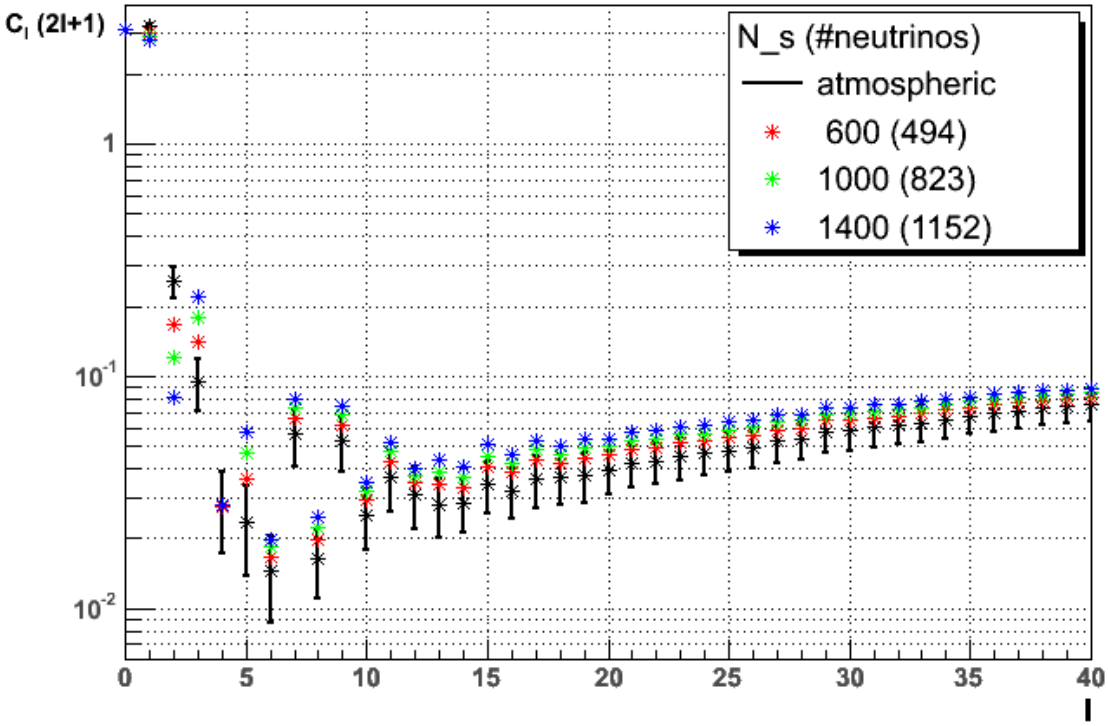

Figure 51: The mean angular power spectrum for mini sources with $\gamma = 2$ and $\mu = 2$ for different source numbers compared to the expectation from the atmospheric neutrinos. The black stars are the mean values for the atmospheric expectation $< C_{l\_atms} >$ with 1σ spread as error bars. The coloured stars are the mean multipole moments for the mini source hypothesis. They have a statistical spread of similar size which is not plotted here. In the legend the number of sources on the whole sphere and the mean number of neutrinos from these sources in the data sample (in brackets) are given.

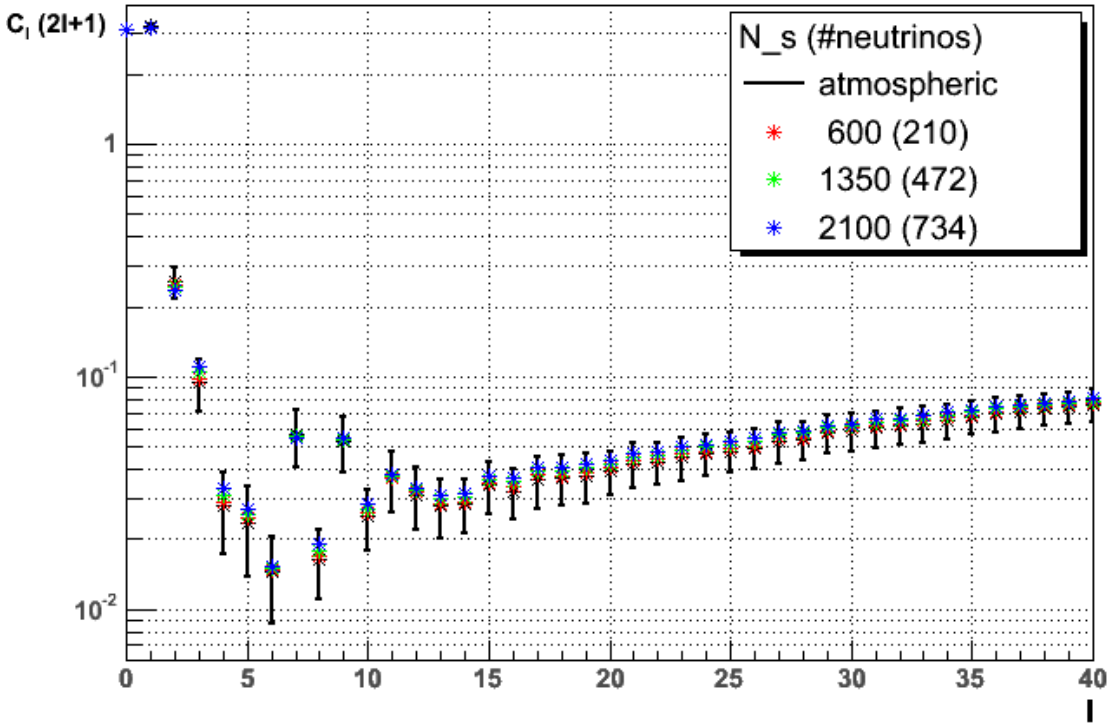

Figure 52: The mean angular power spectrum for micro sources with $\gamma = 2.5$ and $\mu = 1$ for different source numbers compared to the expectation from the atmospheric neutrinos. The black stars are the mean values for the atmospheric expectation $< C_{l\_atms} >$ with 1σ spread as error bars. The coloured stars are the mean multipole moments for the micro source hypothesis. They have a statistical spread of similar size which is not plotted here. In the legend the number of sources on the whole sphere and the mean number of neutrinos from these sources in the data sample (in brackets) are given.

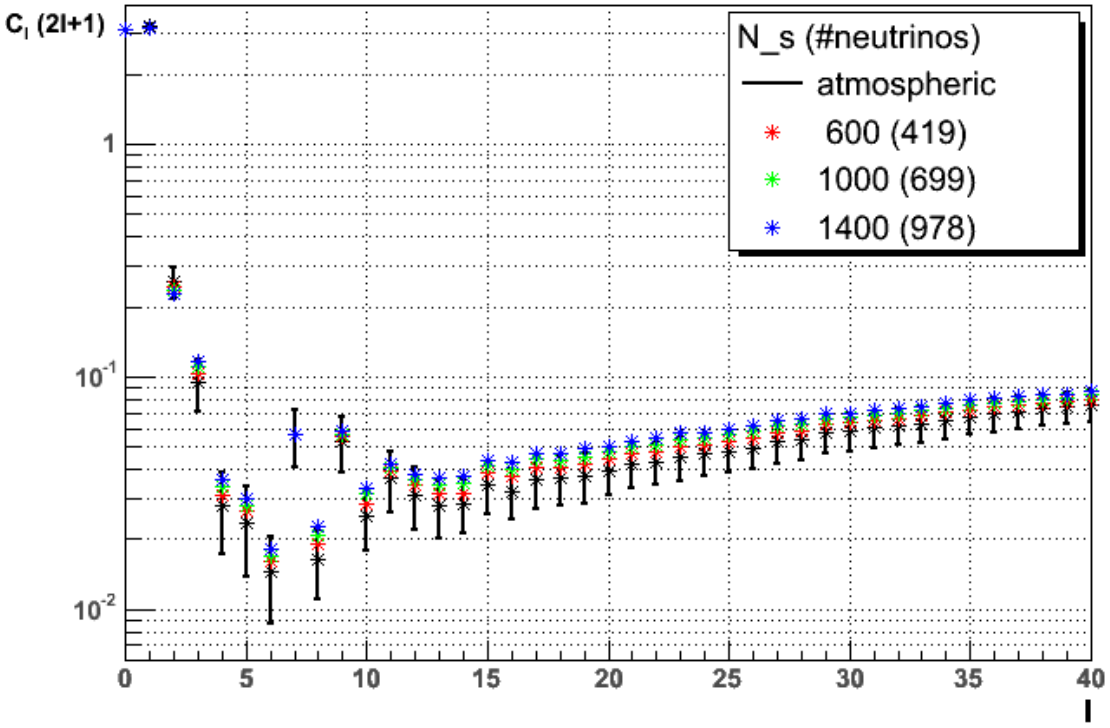

Figure 53: The mean angular power spectrum for mini sources with $\gamma = 2.5$ and $\mu = 2$ for different source numbers compared to the expectation from the atmospheric neutrinos. The black stars are the mean values for the atmospheric expectation $< C_{l\_atms} >$ with 1σ spread as error bars. The coloured stars are the mean multipole moments for the mini source hypothesis. They have a statistical spread of similar size which is not plotted here. In the legend the number of sources on the whole sphere and the mean number of neutrinos from these sources in the data sample (in brackets) are given.

D.2 Micro and Mini Sources in the Galactic Plane

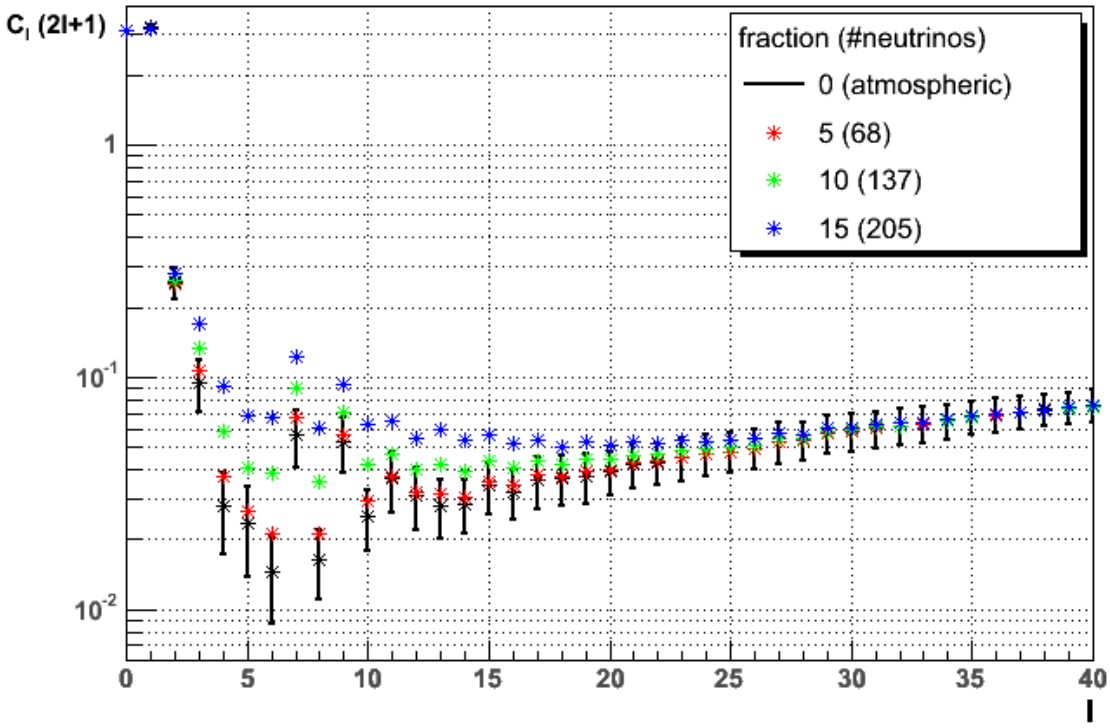

Figure 54: Angular power spectrum for mini sources ($\gamma = 2$,$\mu = 2$) in the galactic plane compared to the expectation from the atmospheric neutrinos. The black stars are the mean values for the atmospheric expectation $< C_{l\_atms} >$ with 1σ spread as error bars. The coloured stars are the mean multipole moments for the signal hypothesis. They have a statistical spread of similar size which is not plotted here. In the legend the fraction of neutrinos from sources in the galactic plane and the mean number of neutrinos from these sources in the data sample (in brackets) are given.

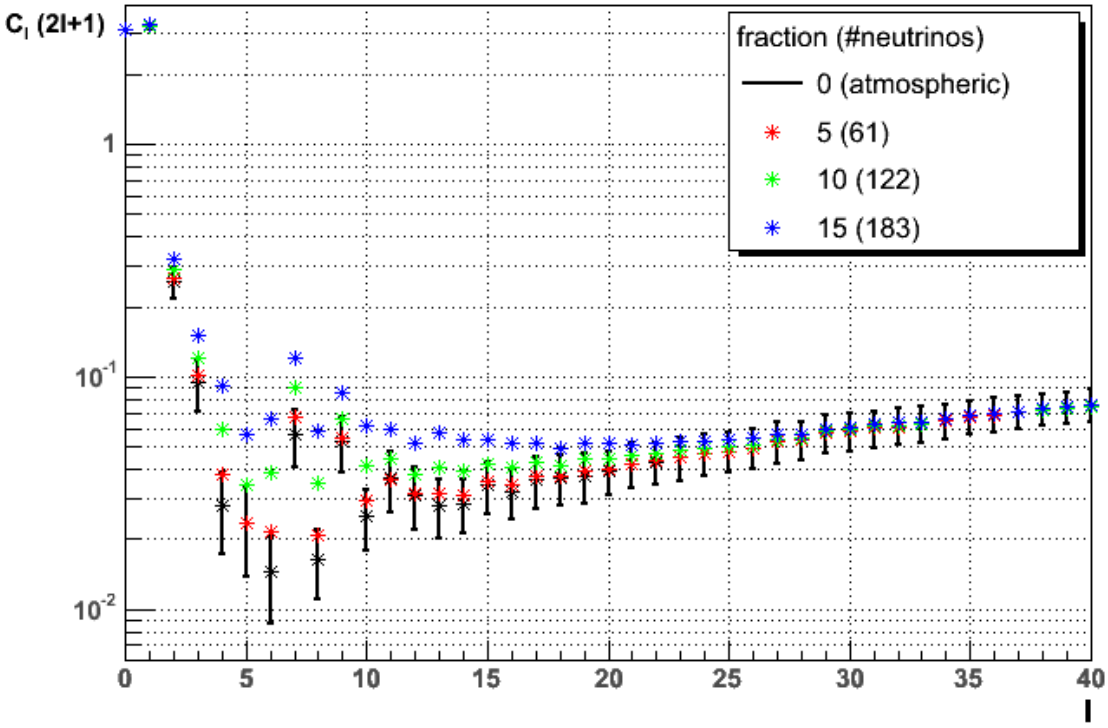

Figure 55: Angular power spectrum for mini sources ($\gamma = 2.4, \mu = 2$) in the galactic plane compared to the expectation from the atmospheric neutrinos. The black stars are the mean values for the atmospheric expectation $< C_{l\_atms} >$ with 1σ spread as error bars. The coloured stars are the mean multipole moments for the signal hypothesis. They have a statistical spread of similar size which is not plotted here. In the legend the fraction of neutrinos from sources in the galactic plane and the mean number of neutrinos from these sources in the data sample (in brackets) are given.

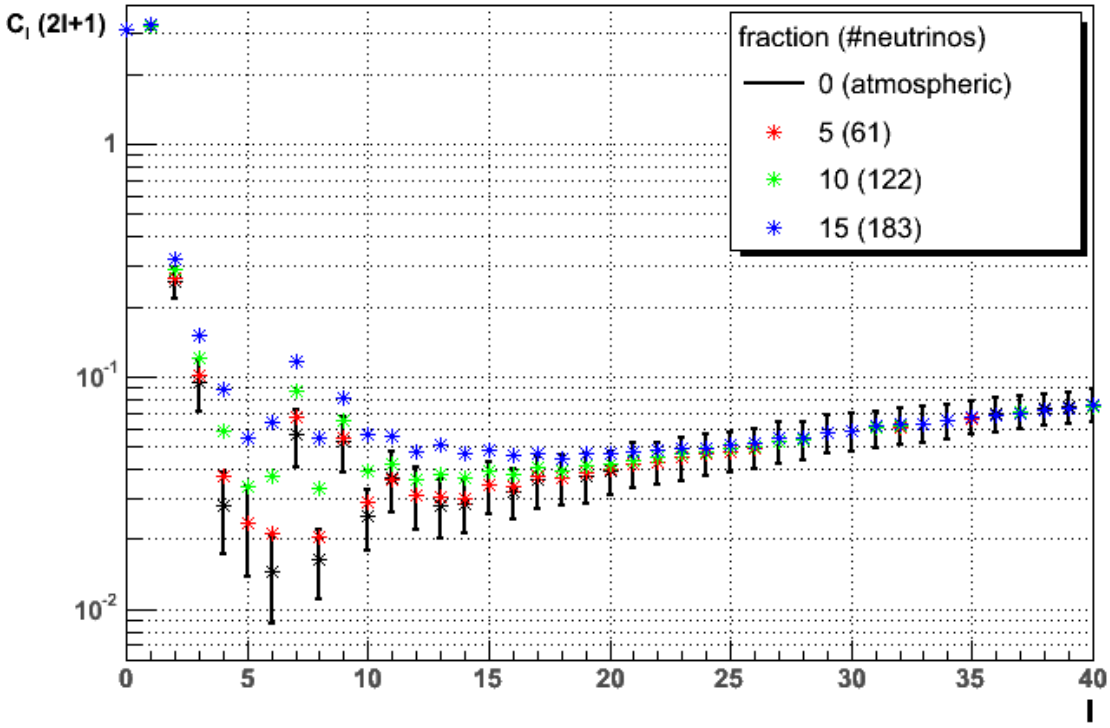

Figure 56: Angular power spectrum for mini sources ($\gamma = 2.4, \mu = 3$) in the galactic plane compared to the expectation from the atmospheric neutrinos. The black stars are the mean values for the atmospheric expectation $< C_{l\_atms} >$ with 1σ spread as error bars. The coloured stars are the mean multipole moments for the signal hypothesis. They have a statistical spread of similar size which is not plotted here. In the legend the fraction of neutrinos from sources in the galactic plane and the mean number of neutrinos from these sources in the data sample (in brackets) are given.

D.3 Micro and Mini Sources in the Super Galactic Plane

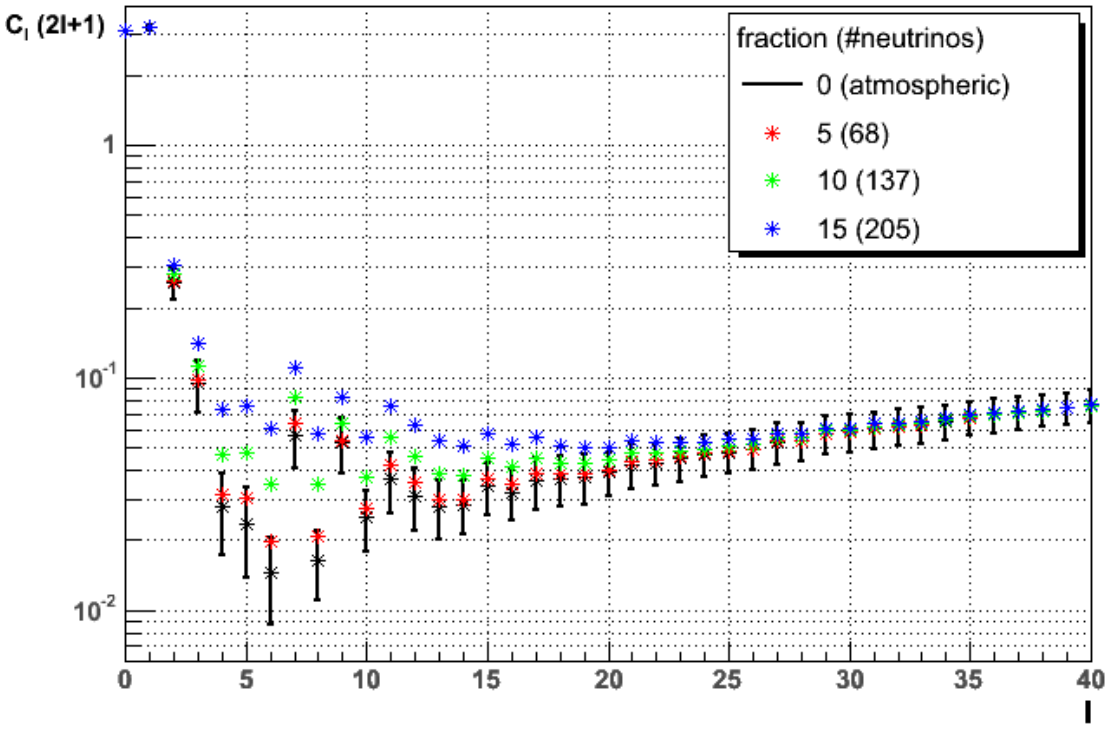

Figure 57: Angular power spectrum for mini sources ($\gamma = 2$,$\mu = 2$) in the super galactic plane compared to the expectation from the atmospheric neutrinos. The black stars are the mean values for the atmospheric expectation $< C_{l\_atms} >$ with 1σ spread as error bars. The coloured stars are the mean multipole moments for the signal hypothesis. They have a statistical spread of similar size which is not plotted here. In the legend the fraction of neutrinos from sources in the galactic plane and the mean number of neutrinos from these sources in the data sample (in brackets) are given.

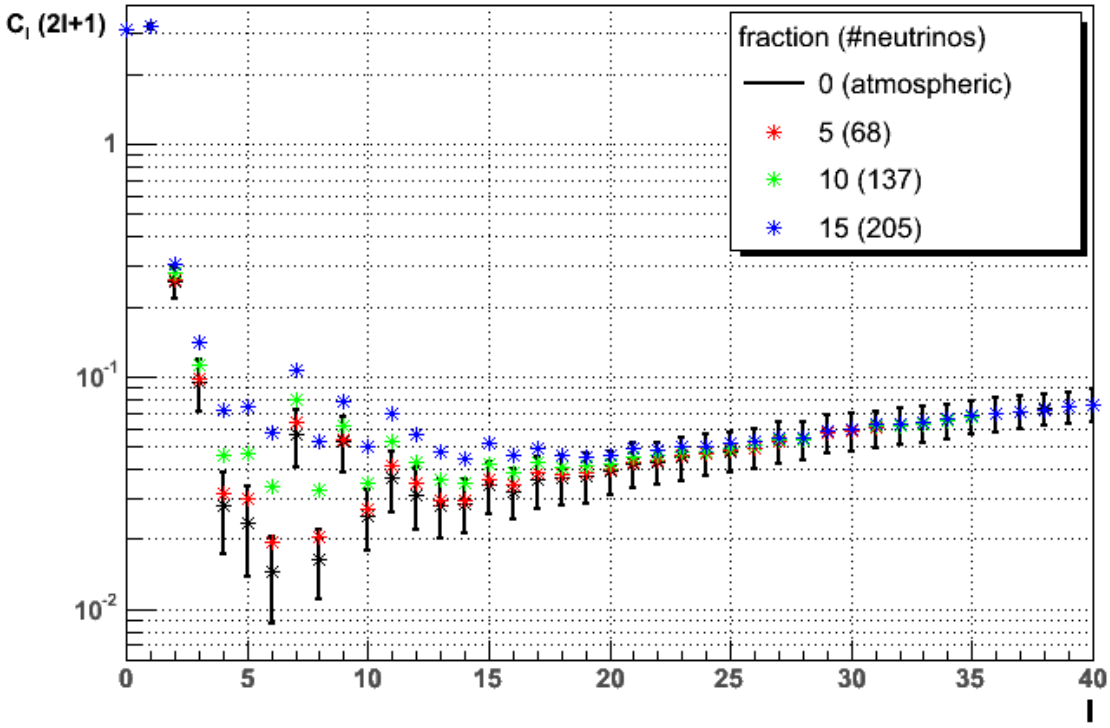

Figure 58: Angular power spectrum for mini sources ($\gamma = 2$,$\mu = 3$) in the super galactic plane compared to the expectation from the atmospheric neutrinos. The black stars are the mean values for the atmospheric expectation $< C_{l\_atms} >$ with 1σ spread as error bars. The coloured stars are the mean multipole moments for the signal hypothesis. They have a statistical spread of similar size which is not plotted here. In the legend the fraction of neutrinos from sources in the galactic plane and the mean number of neutrinos from these sources in the data sample (in brackets) are given.

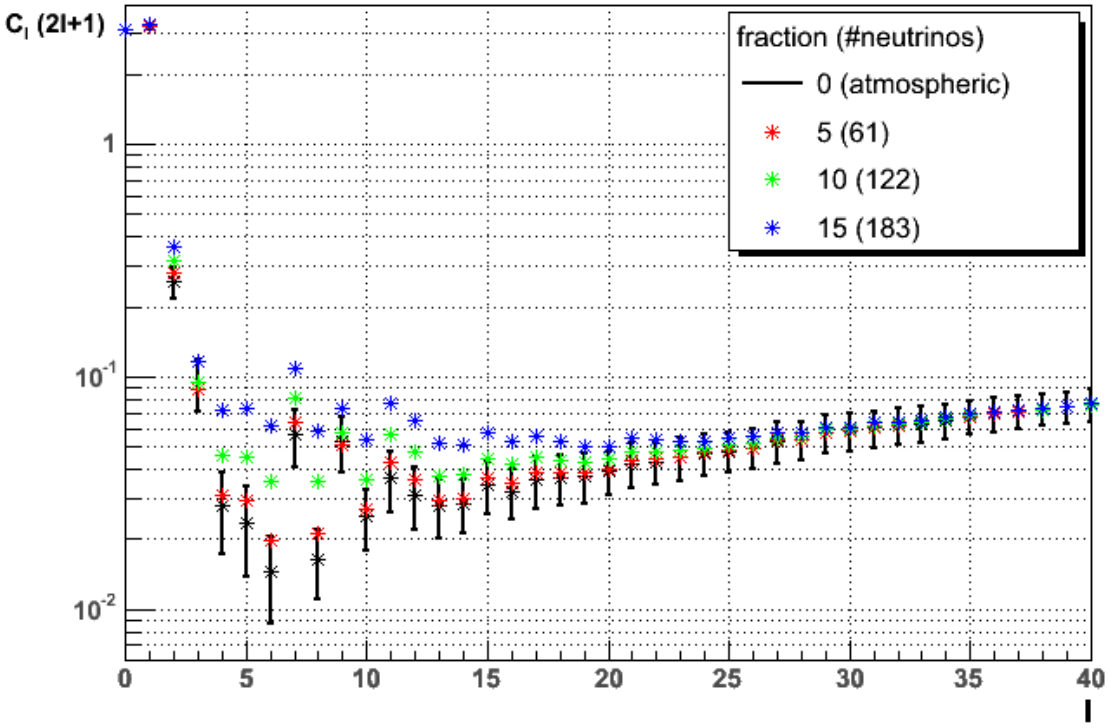

Figure 59: Angular power spectrum for mini sources ($\gamma = 2.4$,$\mu = 2$) in the super galactic plane compared to the expectation from the atmospheric neutrinos. The black stars are the mean values for the atmospheric expectation $< C_{l\_atms} >$ with 1σ spread as error bars. The coloured stars are the mean multipole moments for the signal hypothesis. They have a statistical spread of similar size which is not plotted here. In the legend the fraction of neutrinos from sources in the galactic plane and the mean number of neutrinos from these sources in the data sample (in brackets) are given.

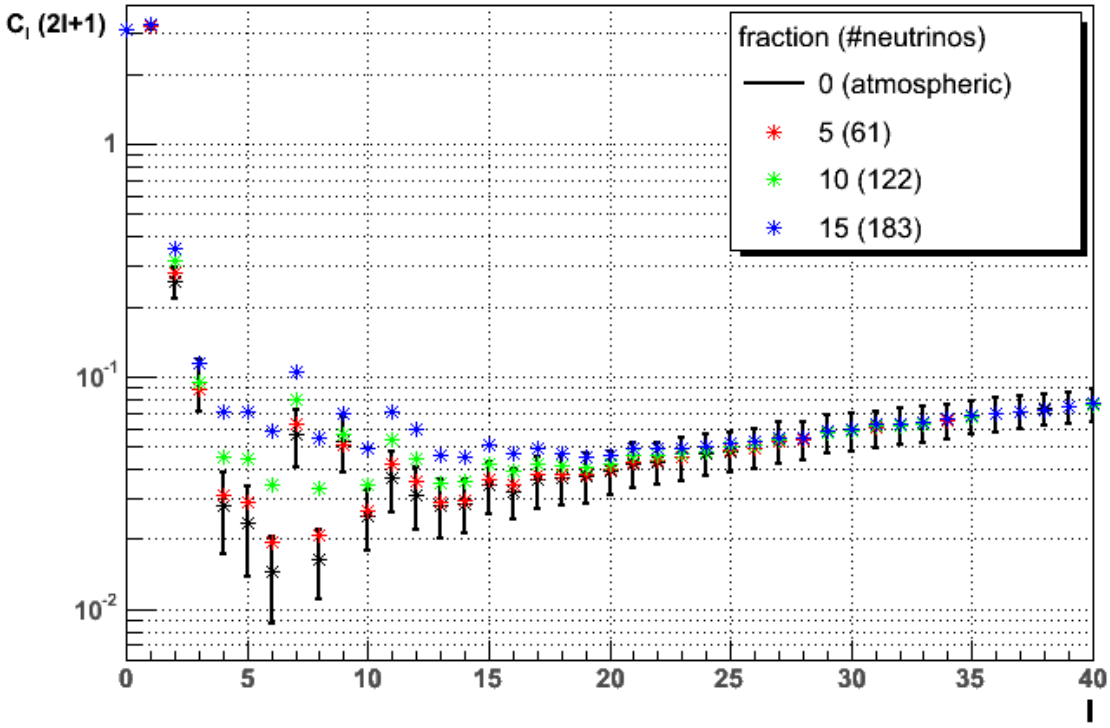

Figure 60: Angular power spectrum for mini sources ($\gamma = 2.4$,$\mu = 3$) in the super galactic plane compared to the expectation from the atmospheric neutrinos. The black stars are the mean values for the atmospheric expectation $< C_{l\_atms} >$ with 1σ spread as error bars. The coloured stars are the mean multipole moments for the signal hypothesis. They have a statistical spread of similar size which is not plotted here. In the legend the fraction of neutrinos from sources in the galactic plane and the mean number of neutrinos from these sources in the data sample (in brackets) are given.

E Probabilities for Signals to Appear as Background

E.1 Isotropic Micro and Mini Sources

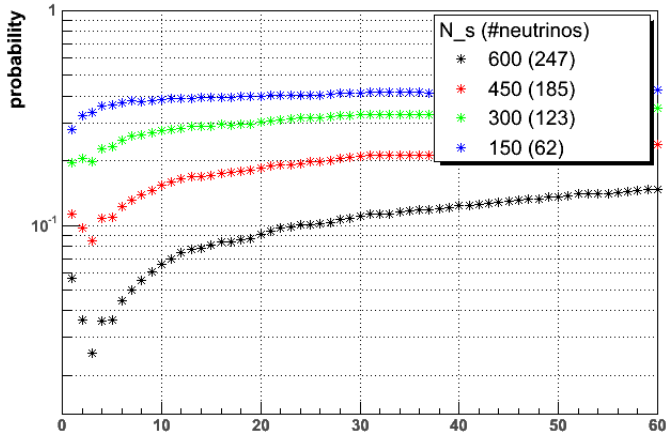

Figure 61: χ^2-probability for an angular power spectrum of micro sources ($\gamma = 2$ and $\mu = 1$) to appear as atmospheric background signal depending on the used multipole moments.

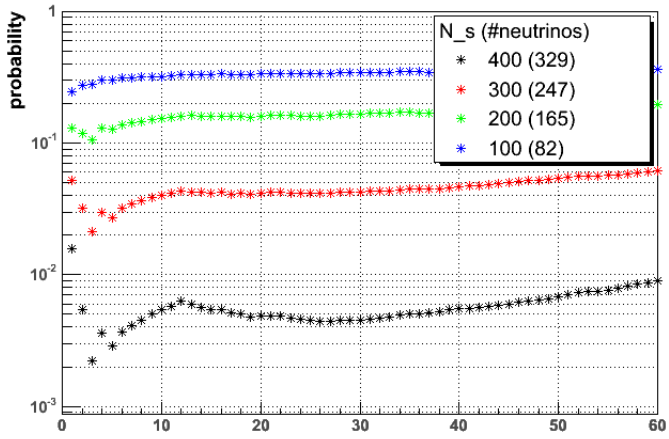

Figure 62: χ^2-probability for an angular power spectrum of mini sources ($\gamma = 2$ and $\mu = 2$) to appear as atmospheric background signal depending on the used multipole moments.

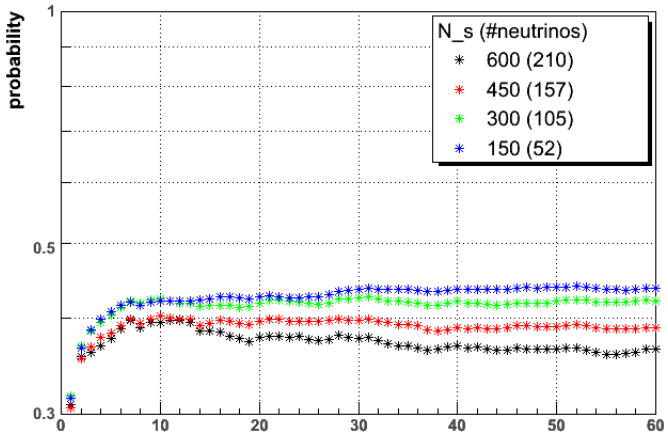

Figure 63: χ^2-probability for an angular power spectrum of micro sources ($\gamma = 2.5$ and $\mu = 1$) to appear as atmospheric background signal depending on the used multipole moments.

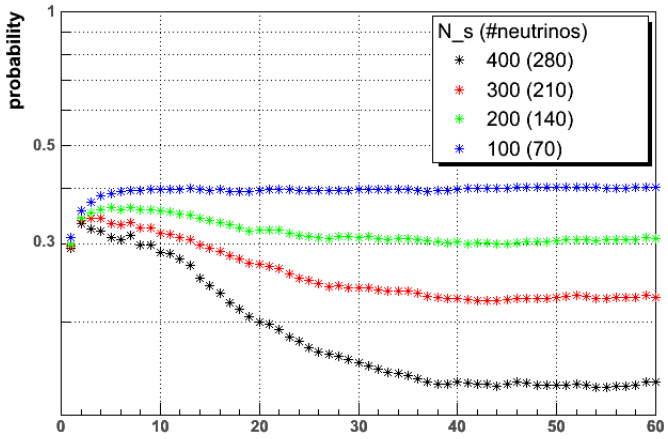

Figure 64: χ^2-probability for an angular power spectrum of mini sources ($\gamma = 2.5$ and $\mu = 2$) to appear as atmospheric background signal depending on the used multipole moments.

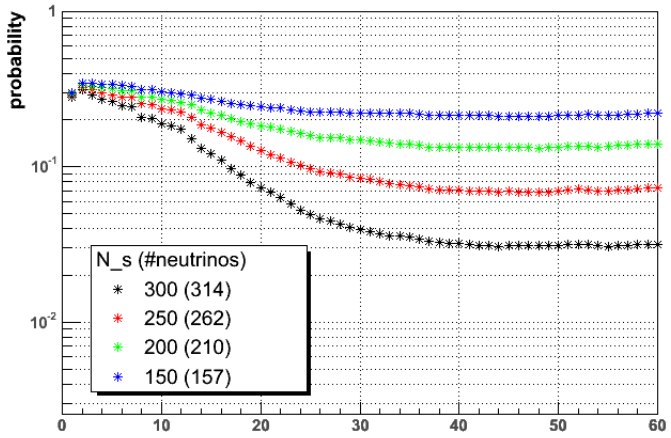

Figure 65: χ^2-probability for an angular power spectrum of mini sources ($\gamma = 2.5$ and $\mu = 3$) to appear as atmospheric background signal depending on the used multipole moments.

E.2 Micro and Mini Sources in the Galactic Plane

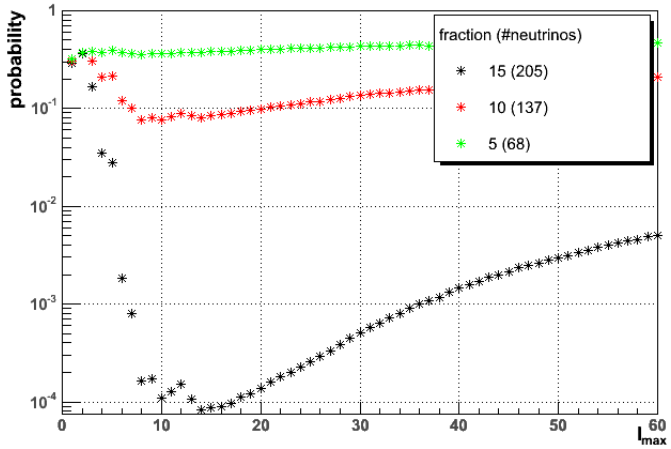

Figure 66: χ^2-probability for an angular power spectrum of the galactic plane with mini sources ($\gamma = 2$ and $\mu = 2$) to appear as atmospheric background depending on the used multipole moments.

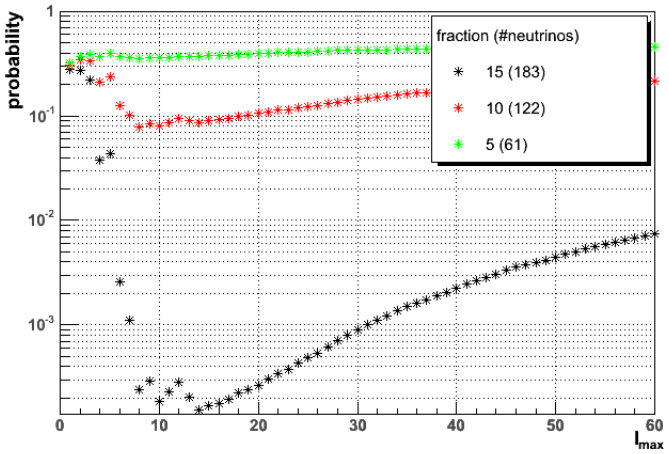

Figure 67: χ^2-probability for an angular power spectrum of the galactic plane with mini sources ($\gamma = 2.4$ and $\mu = 2$) to appear as atmospheric background depending on the used multipole moments.

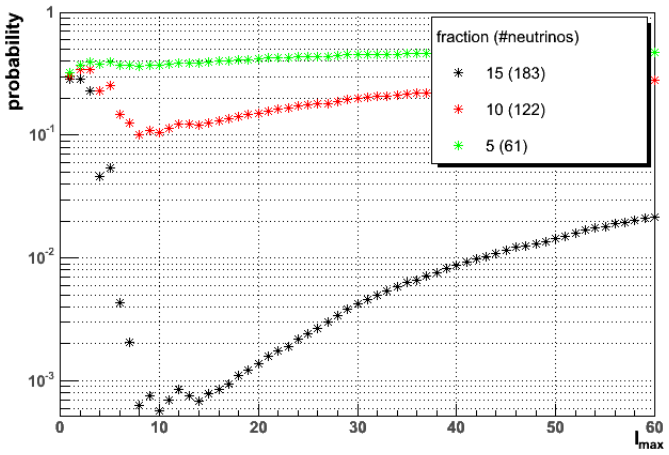

Figure 68: χ^2-probability for an angular power spectrum of the galactic plane with mini sources ($\gamma = 2.4$ and $\mu = 3$) to appear as atmospheric background depending on the used multipole moments.

E.3 Micro and Mini Sources in the Super Galactic Plane

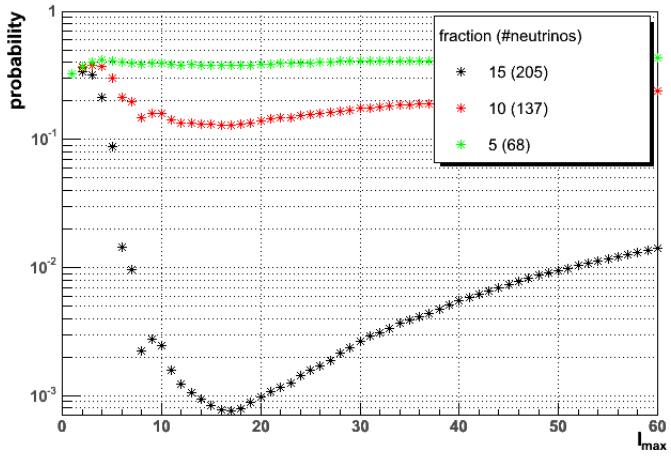

Figure 69: χ^2-probability for an angular power spectrum of the super galactic plane with mini sources ($\gamma = 2$ and $\mu = 2$) to appear as atmospheric background depending on the used multipole moments.

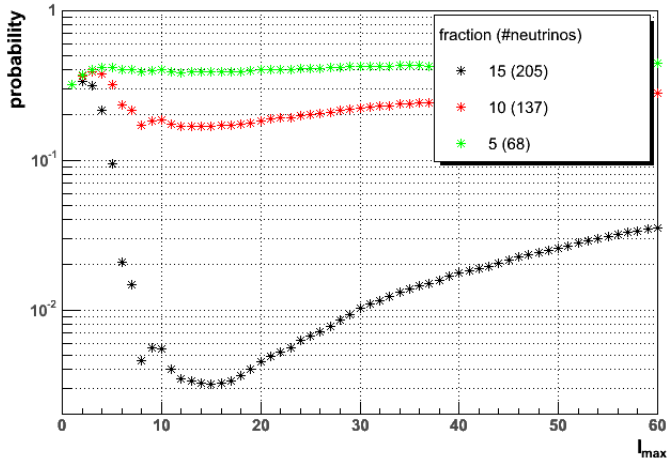

Figure 70: χ^2-probability for an angular power spectrum of the super galactic plane with mini sources ($\gamma = 2$ and $\mu = 3$) to appear as atmospheric background depending on the used multipole moments.

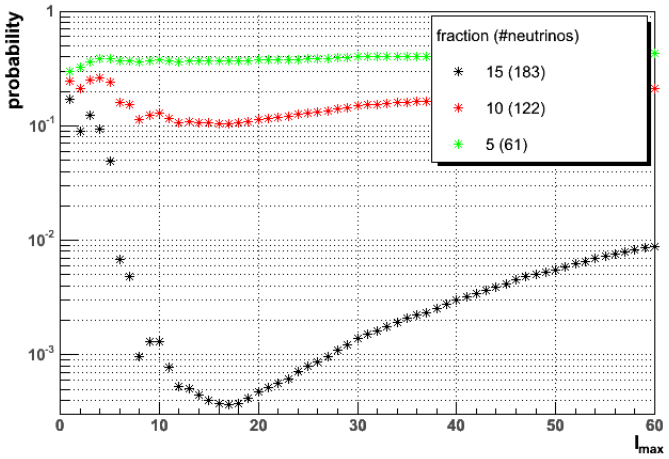

Figure 71: χ^2-probability for an angular power spectrum of the super galactic plane with mini sources ($\gamma = 2.4$ and $\mu = 2$) to appear as atmospheric background depending on the used multipole moments.

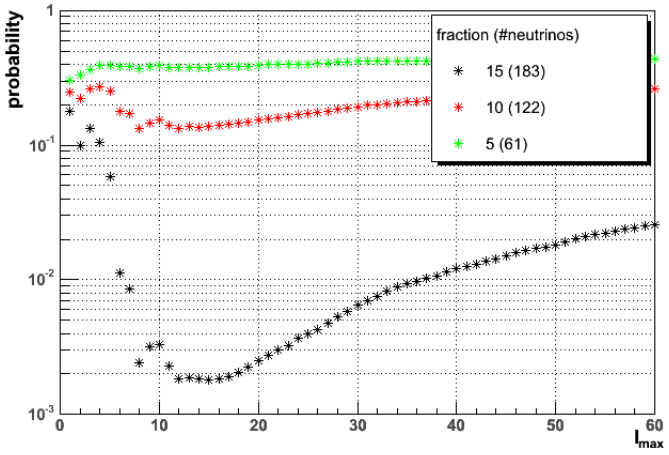

Figure 72: χ^2-probability for an angular power spectrum of the super galactic plane with mini sources ($\gamma = 2.4$ and $\mu = 3$) to appear as atmospheric background depending on the used multipole moments.

F Confidence Belts for Different Hypotheses

F.1 Isotropic Micro and Mini Sources

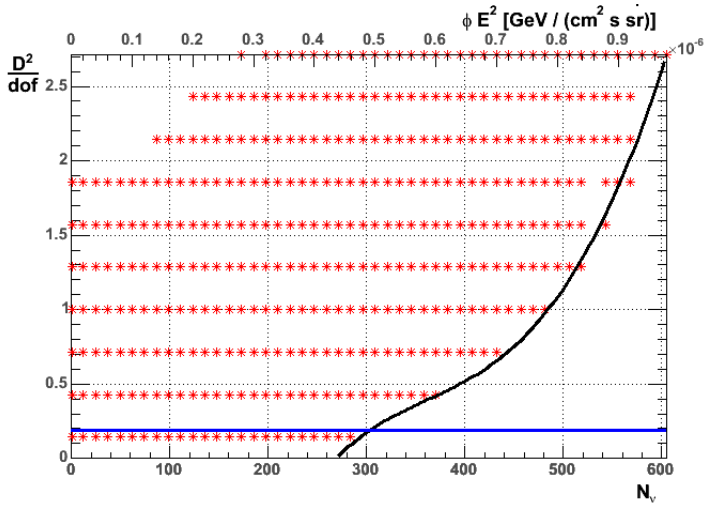

Figure 73: Confidence belt for micro sources with $\gamma = 2$, $\mu = 1$ and a range $l = 2, 3, 5$. The area with the red stars is the 90% confidence region, bordered by the black line. The blue line is the measured data ($D^2/dof = 0.19$). The intersection with the black line corresponds to the upper limit $N_{\nu\ tot}^{limit} = 300$.

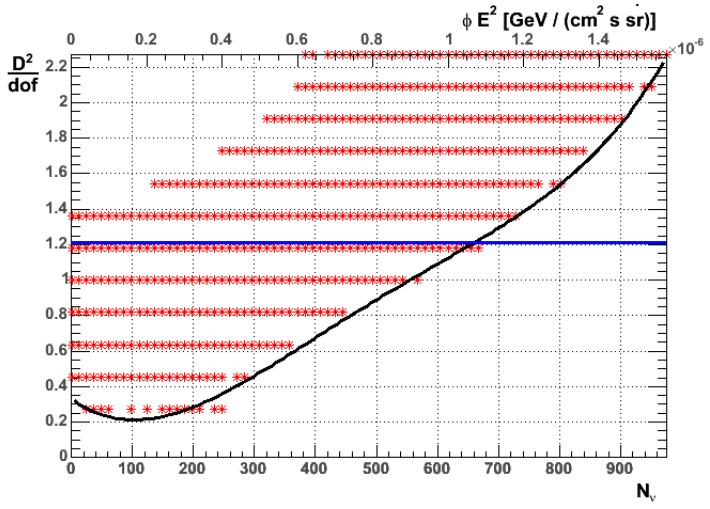

Figure 74: Confidence belt for micro sources with $\gamma = 2$, $\mu = 1$ and a range $l = 1 - 40$. The area with the red stars is the 90% confidence region, bordered by the black line. The blue line is the measured data ($D^2/dof = 1.21$). The intersection with the black line corresponds to the upper limit $N_{\nu\ tot}^{limit} = 660$.

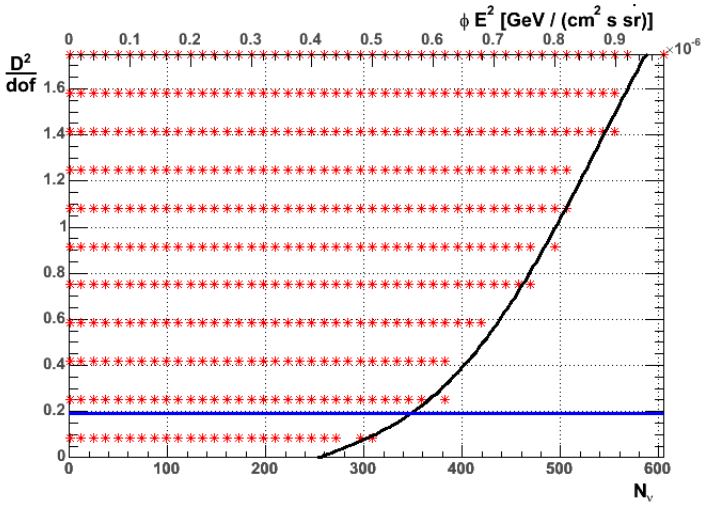

Figure 75: Confidence belt for mini sources with $\gamma = 2$, $\mu = 2$ and a range $l = 2, 3, 5$. The area with the red stars is the 90% confidence region, bordered by the black line. The blue line is the measured data ($D^2/dof = 0.19$). The intersection with the black line corresponds to the upper limit $N_{\nu\ tot}^{limit} = 345$.

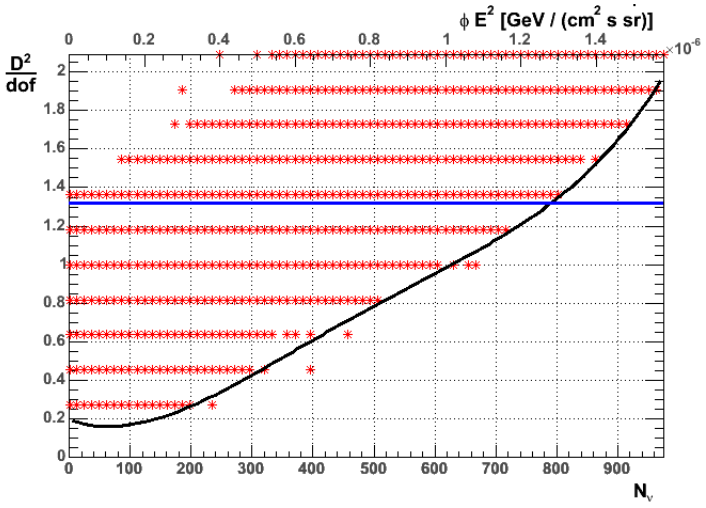

Figure 76: Confidence belt for mini sources with $\gamma = 2$, $\mu = 2$ and a range $l = 13 - 40$. The area with the red stars is the 90% confidence region, bordered by the black line. The blue line is the measured data ($D^2/dof = 1.32$). The intersection with the black line corresponds to the upper limit $N_{\nu\ tot}^{limit} = 785$.

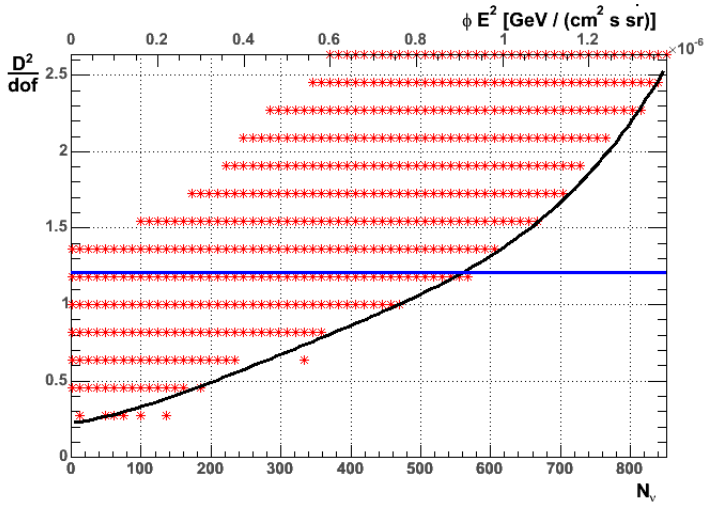

Figure 77: Confidence belt for mini sources with $\gamma = 2$, $\mu = 2$ and a range $l = 1 - 40$. The area with the red stars is the 90% confidence region, bordered by the black line. The blue line is the measured data ($D^2/dof = 1.21$). The intersection with the black line corresponds to the upper limit $N_{\nu\ tot}^{limit} = 560$.

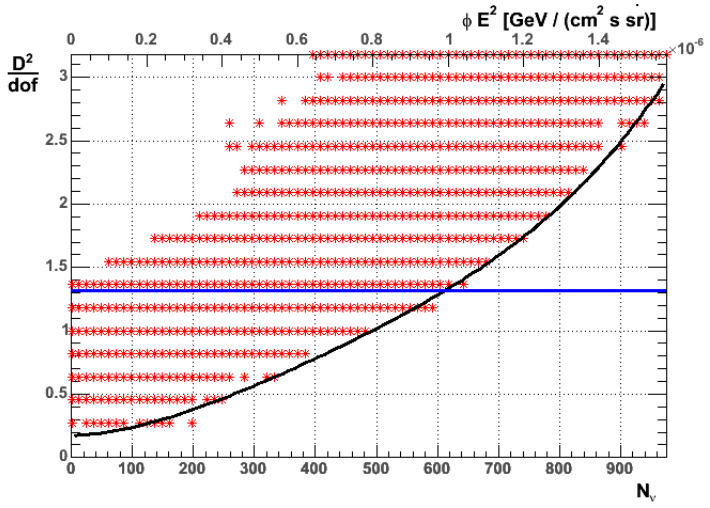

Figure 78: Confidence belt for mini sources with $\gamma = 2$, $\mu = 3$ and a range $l = 13 - 40$. The area with the red stars is the 90% confidence region, bordered by the black line. The blue line is the measured data ($D^2/dof 1.32$). The intersection with the black line corresponds to the upper limit $N_{\nu\ tot}^{limit} = 620$.

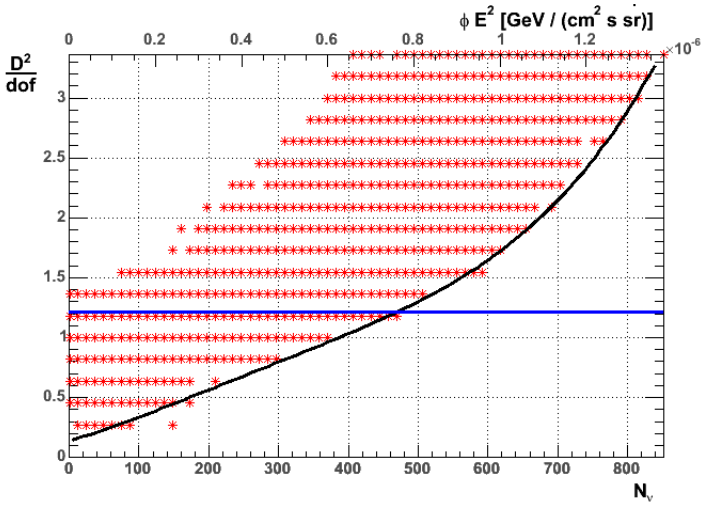

Figure 79: Confidence belt for mini sources with $\gamma = 2$, $\mu = 3$ and a range $l = 1 - 40$. The area with the red stars is the 90% confidence region, bordered by the black line. The blue line is the measured data ($D^2/dof = 1.21$). The intersection with the black line corresponds to the upper limit $N_{\nu\ tot}^{limit} = 460$.

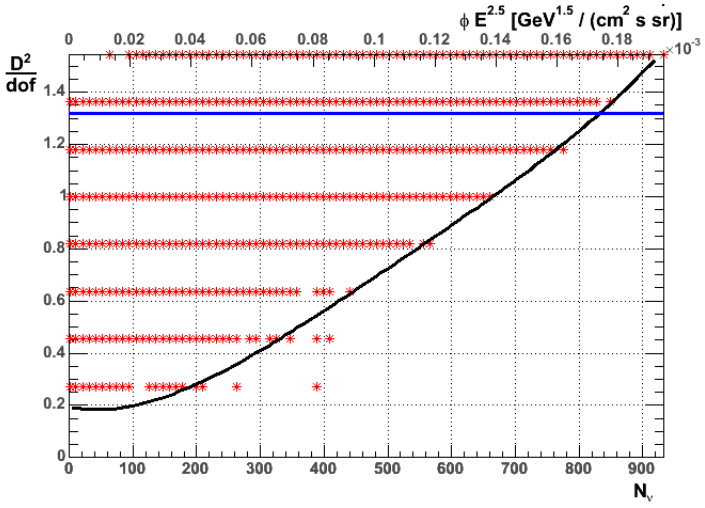

Figure 80: Confidence belt for mini sources with $\gamma = 2.5$, $\mu = 2$ and a range $l = 13 - 40$. The area with the red stars is the 90% confidence region, bordered by the black line. The blue line is the measured data ($D^2/dof = 1.32$). The intersection with the black line corresponds to the upper limit $N_{\nu\ tot}^{limit} = 825$.

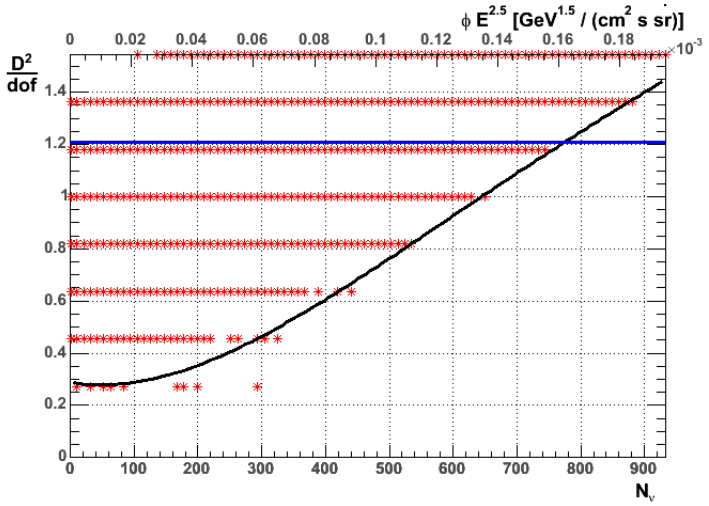

Figure 81: Confidence belt for mini sources with $\gamma = 2.5$, $\mu = 2$ and a range $l = 1 - 40$. The area with the red stars is the 90% confidence region, bordered by the black line. The blue line is the measured data ($D^2/dof = 1.21$). The intersection with the black line corresponds to the upper limit $N_{\nu\ tot}^{limit} = 775$.

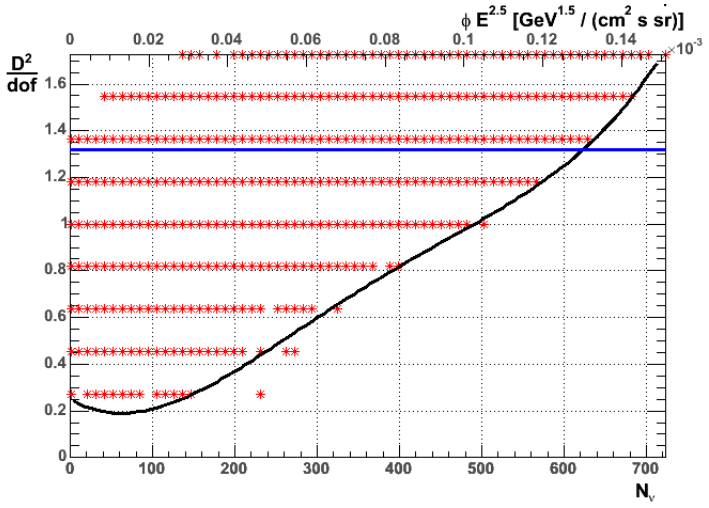

Figure 82: Confidence belt for mini sources with $\gamma = 2.5$, $\mu = 3$ and a range $l = 13 - 40$. The area with the red stars is the 90% confidence region, bordered by the black line. The blue line is the measured data ($D^2/dof = 1.32$). The intersection with the black line corresponds to the upper limit $N_{\nu\ tot}^{limit} = 572$.

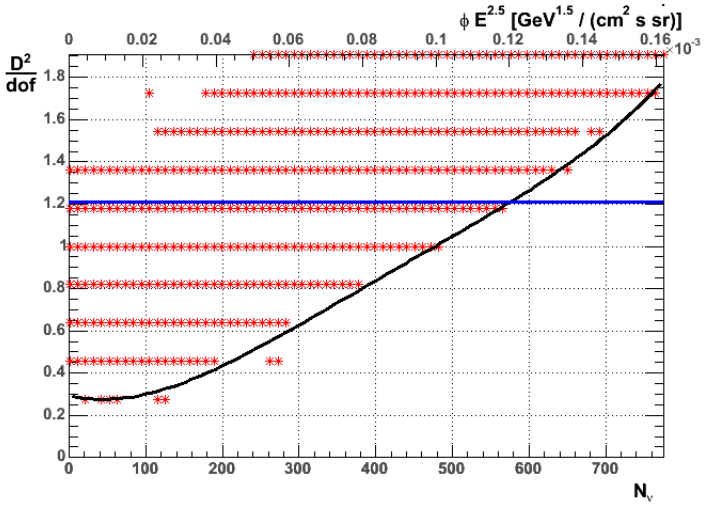

Figure 83: Confidence belt for mini sources with $\gamma = 2.5$, $\mu = 3$ and a range $l = 1 - 40$. The area with the red stars is the 90% confidence region, bordered by the black line. The blue line is the measured data ($D^2/dof = 1.21$). The intersection with the black line corresponds to the upper limit $N_{\nu\ tot}^{limit} = 625$.

F.2 Micro and Mini Sources in the Galactic Plane

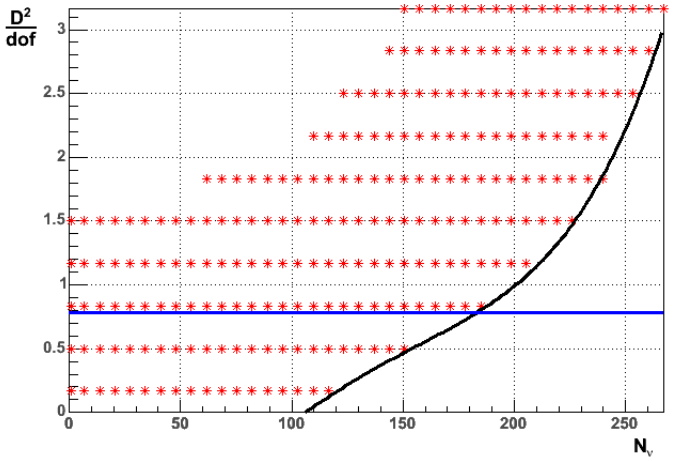

Figure 84: Confidence belt for mini sources with $\gamma = 2$, $\mu = 2$ in the galactic plane and a range $l = 1 - 15$. The area with the red stars is the 90% confidence region, bordered by the black line. The blue line is the measured data ($D^2/dof = 0.78$). The intersection with the black line corresponds to the upper limit $N_{\nu\ tot}^{limit} = 182$.

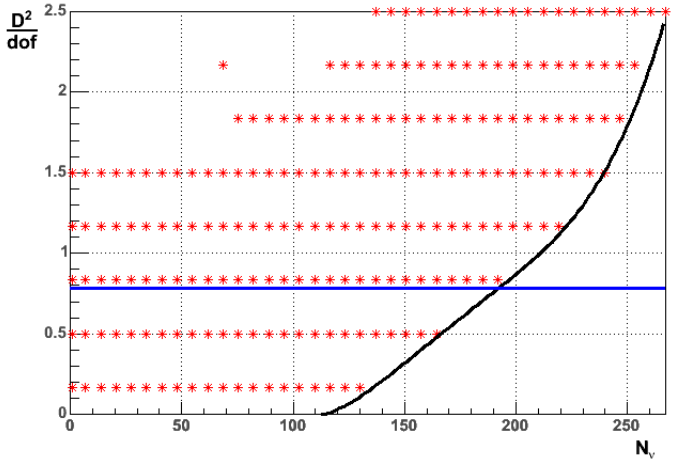

Figure 85: Confidence belt for mini sources with $\gamma = 2$, $\mu = 3$ in the galactic plane and a range $l = 1 - 15$. The area with the red stars is the 90% confidence region, bordered by the black line. The blue line is the measured data ($D^2/dof = 0.78$). The intersection with the black line corresponds to the upper limit $N_{\nu\,tot}^{limit} = 190$.

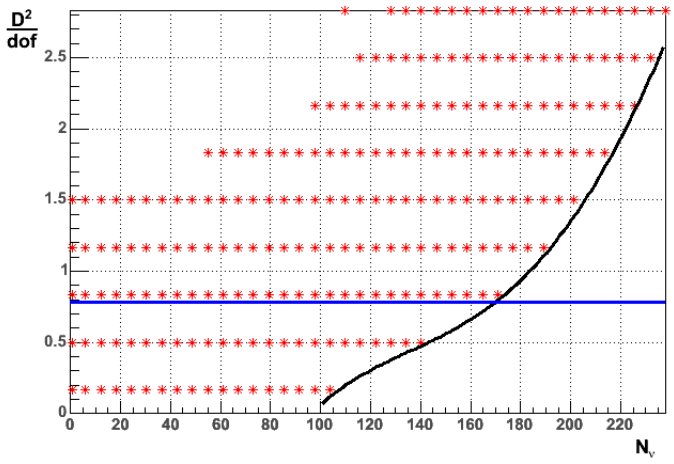

Figure 86: Confidence belt for mini sources with $\gamma = 2.4$, $\mu = 2$ in the galactic plane and a range $l = 1 - 15$. The area with the red stars is the 90% confidence region, bordered by the black line. The blue line is the measured data ($D^2/dof = 0.78$). The intersection with the black line corresponds to the upper limit $N_{\nu\,tot}^{limit} = 168$.

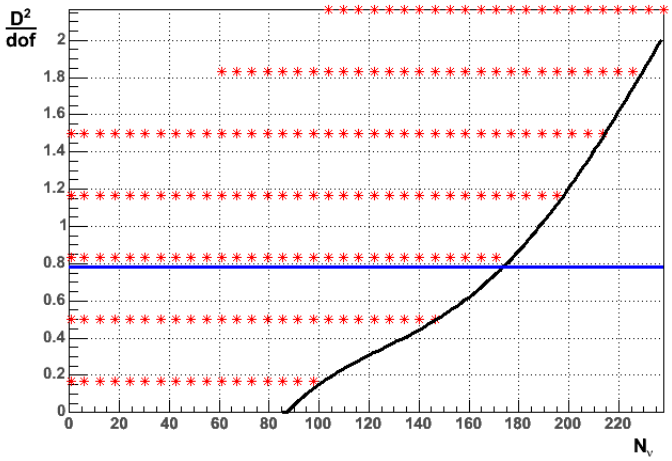

Figure 87: Confidence belt for mini sources with $\gamma = 2.4$, $\mu = 3$ in the galactic plane and a range $l = 1 - 15$. The area with the red stars is the 90% confidence region, bordered by the black line. The blue line is the measured data ($D^2/dof = 0.78$). The intersection with the black line corresponds to the upper limit $N_{\nu\ tot}^{limit} = 172$.

F.3 Micro and Mini Sources in the Super Galactic Plane

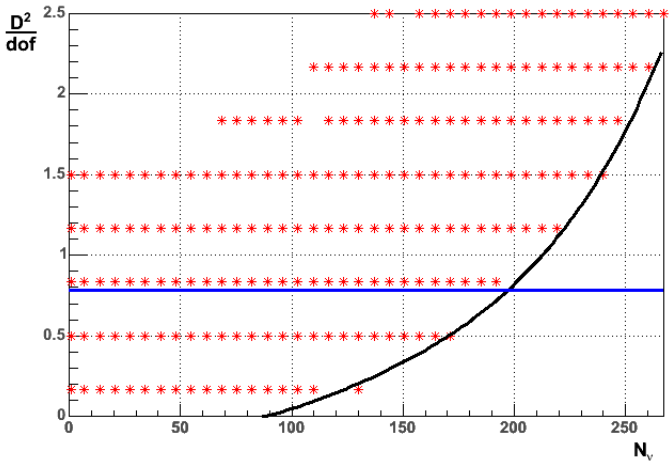

Figure 88: Confidence belt for mini sources with $\gamma = 2$, $\mu = 2$ in the super galactic plane and a range $l = 1-15$. The area with the red stars is the 90% confidence region, bordered by the black line. The blue line is the measured data ($D^2/dof = 0.78$). The intersection with the black line corresponds to the upper limit $N_{\nu\ tot}^{limit} = 197$.

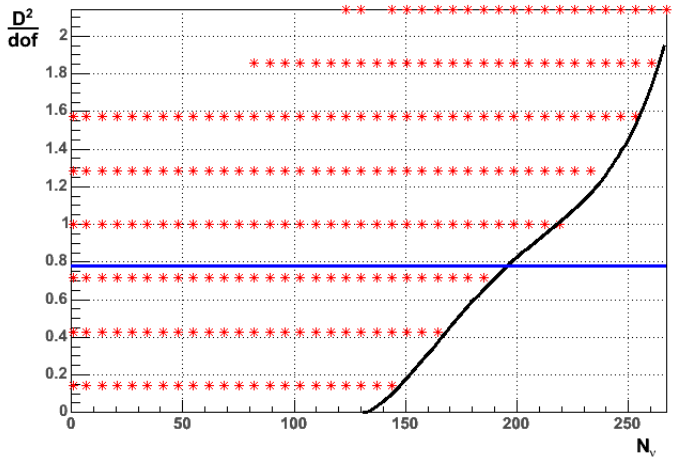

Figure 89: Confidence belt for mini sources with $\gamma = 2$, $\mu = 3$ in the super galactic plane and a range $l = 1-15$. The area with the red stars is the 90% confidence region, bordered by the black line. The blue line is the measured data ($D^2/dof = 0.78$). The intersection with the black line corresponds to the upper limit $N_{\nu\ tot}^{limit} = 195$.

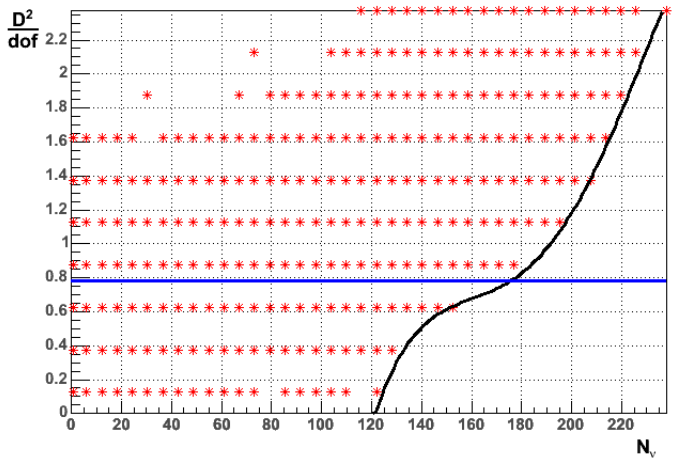

Figure 90: Confidence belt for mini sources with $\gamma = 2.4$, $\mu = 2$ in the super galactic plane and a range $l = 1 - 15$. The area with the red stars is the 90% confidence region, bordered by the black line. The blue line is the measured data ($D^2/dof = 0.78$). The intersection with the black line corresponds to the upper limit $N_{\nu\ tot}^{limit} = 175$.

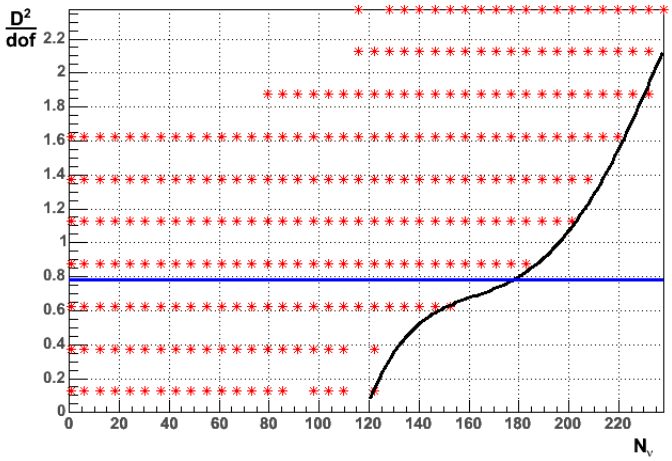

Figure 91: Confidence belt for mini sources with $\gamma = 2.4$, $\mu = 3$ in the super galactic plane and a range $l = 1 - 15$. The area with the red stars is the 90% confidence region, bordered by the black line. The blue line is the measured data ($D^2/dof = 0.78$). The intersection with the black line corresponds to the upper limit $N_{\nu\ tot}^{limit} = 178$.

F.4 Neutrinos from Interactions in the Galactic Plane

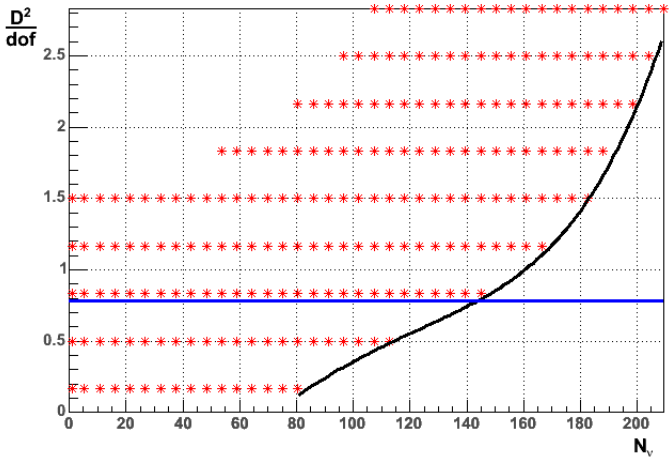

Figure 92: Confidence belt for neutrinos from cosmic ray interactions in the galactic plane and a range $l = 1-15$. The area with the red stars is the 90% confidence region, bordered by the black line. The blue line is the measured data ($D^2/dof = 0.78$). The intersection with the black line corresponds to the upper limit $N_{\nu\ tot}^{limit} = 145$.

F.5 Neutrino Oscillation

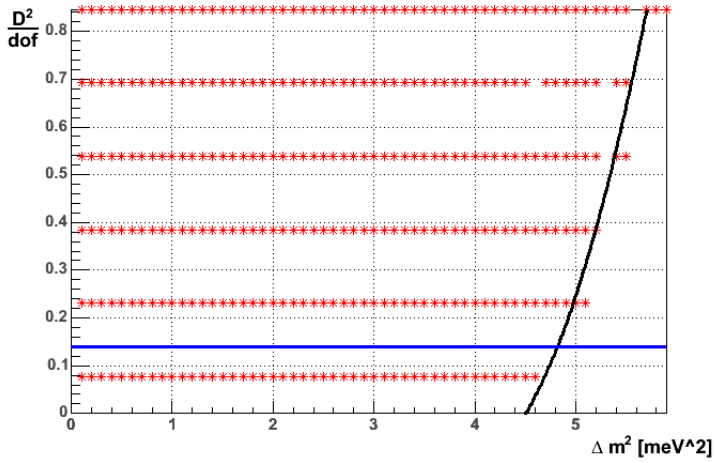

Figure 93: Confidence belt for neutrino oscillations. The moments C_2 and C_3 are used. The area with the red stars is the 90% confidence region, bordered by the black line. The blue line is the measured data ($D^2/dof = 0.78$). The intersection with the black line corresponds to the upper limit $\Delta m^2_{limit} = 4.8 \cdot 10^{-3}$ eV^2.

F.6 Mis-reconstructed Down-Going Muons

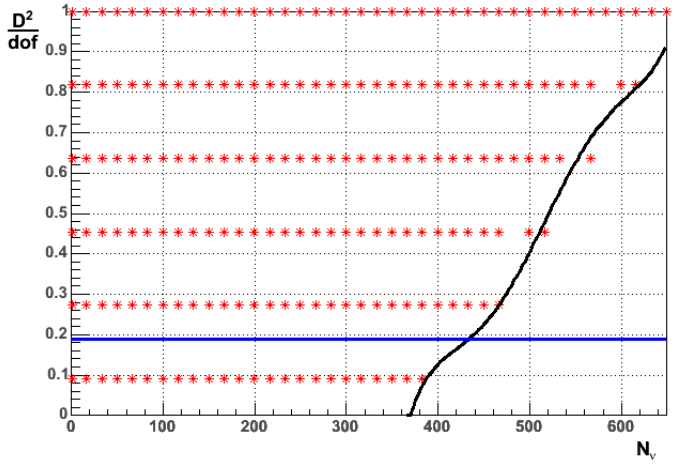

Figure 94: Confidence belt for flat distributed mis-reconstructed down-going muons ($l = 2, 3, 5$). The area with the red stars is the 90% confidence region, bordered by the black line. The blue line is the measured data ($D^2/dof = 0.19$). The intersection with the black line corresponds to the upper limit $N^{limit}_{\nu\ tot} = 440$.

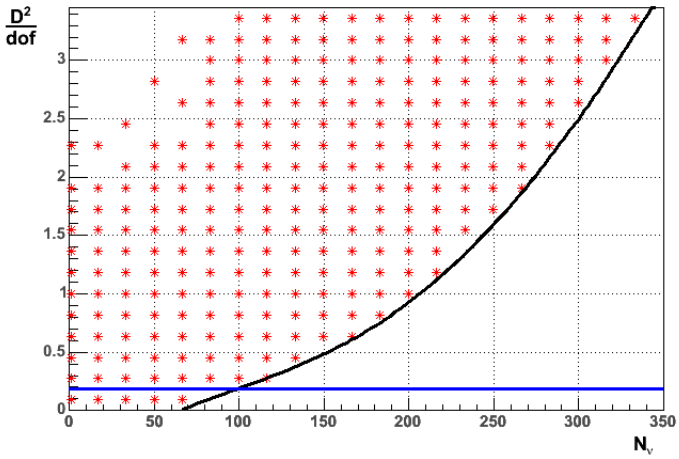

Figure 95: Confidence belt for mis-reconstructed down-going muons (g90) (range $l = 2, 3, 5$). The area with the red stars is the 90% confidence region, bordered by the black line. The blue line is the measured data ($D^2/dof = 0.19$). The intersection with the black line corresponds to the upper limit $N^{limit}_{\nu\ tot} = 100$.

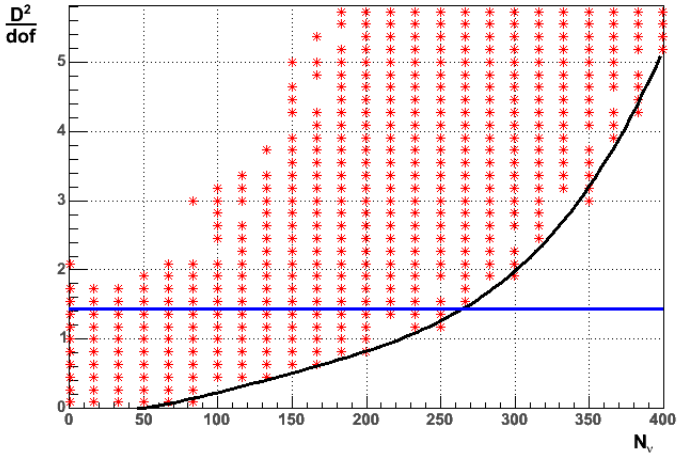

Figure 96: Confidence belt for mis-reconstructed down-going muons (g90) (range $l = 6 - 12$). The area with the red stars is the 90% confidence region, bordered by the black line. The blue line is the measured data ($D^2/dof = 1.43$). The intersection with the black line corresponds to the upper limit $N^{limit}_{\nu\ tot} = 265$.

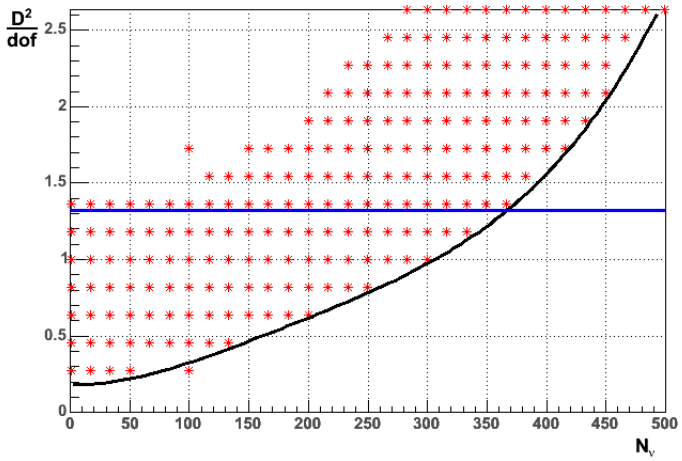

Figure 97: Confidence belt for mis-reconstructed down-going muons (g90) (range $l = 13 - 40$). The area with the red stars is the 90% confidence region, bordered by the black line. The blue line is the measured data ($D^2/dof = 1.32$). The intersection with the black line corresponds to the upper limit $N_{\nu\ tot}^{limit} = 370$.

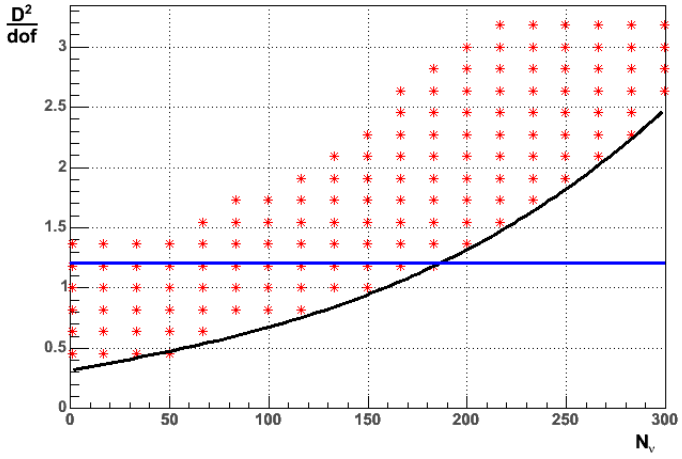

Figure 98: Confidence belt for mis-reconstructed down-going muons (g90) (range $l = 1 - 40$). The area with the red stars is the 90% confidence region, bordered by the black line. The blue line is the measured data ($D^2/dof = 1.21$). The intersection with the black line corresponds to the upper limit $N_{\nu\ tot}^{limit} = 185$.

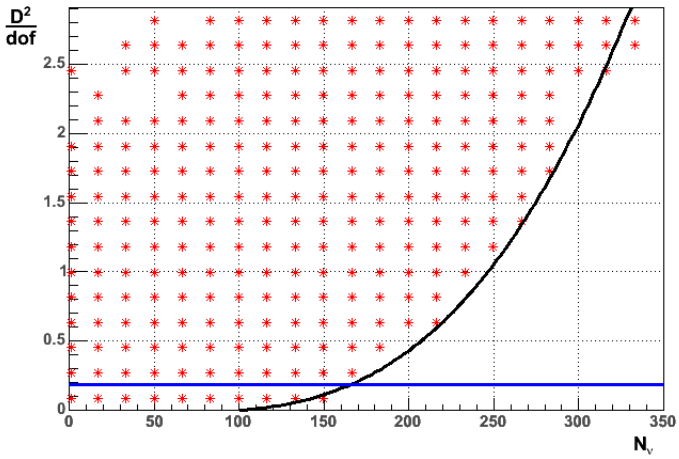

Figure 99: Confidence belt for mis-reconstructed down-going muons (g105) (range $l = 2, 3, 5$). The area with the red stars is the 90% confidence region, bordered by the black line. The blue line is the measured data ($D^2/dof = 0.19$). The intersection with the black line corresponds to the upper limit $N_{\nu\ tot}^{limit} = 167$.

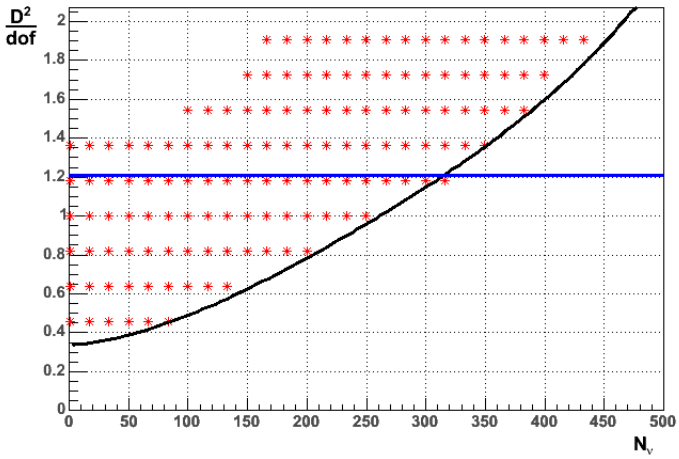

Figure 100: Confidence belt for mis-reconstructed down-going muons (g105) (range $l = 1 - 40$). The area with the red stars is the 90% confidence region, bordered by the black line. The blue line is the measured data ($D^2/dof = 1.21$). The intersection with the black line corresponds to the upper limit $N_{\nu\ tot}^{limit} = 320$.

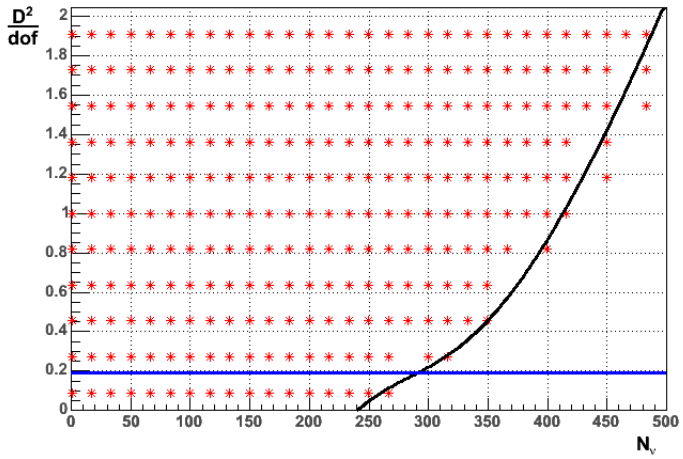

Figure 101: Confidence belt for mis-reconstructed down-going muons (g140) (range $l = 2, 3, 5$). The area with the red stars is the 90% confidence region, bordered by the black line. The blue line is the measured data ($D^2/dof = 0.19$). The intersection with the black line corresponds to the upper limit $N_{\nu\ tot}^{limit} = 290$.

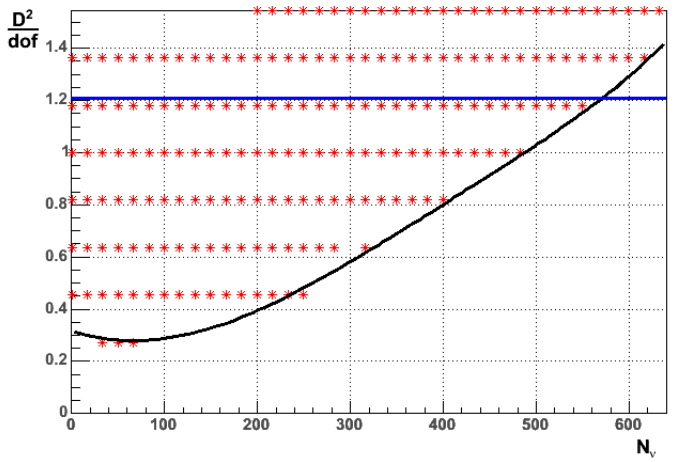

Figure 102: Confidence belt for mis-reconstructed down-going muons (g140) (range $l = 1 - 40$). The area with the red stars is the 90% confidence region, bordered by the black line. The blue line is the measured data ($D^2/dof = 1.21$). The intersection with the black line corresponds to the upper limit $N_{\nu\ tot}^{limit} = 570$.

Acknowledgements

This thesis would not have been possible in this way without the help of many people. I am thankful for this support.
Thanks to Prof. Dr. Karl-Heinz Kampert and Dr. Christopher Wiebusch. They inspired me and gave me a great insight to astro-particle physics.
Markus Ackermann and Raphael Lang did their best to explain me the data set used in this analysis and how to extract the information from the file. There are a lot of tricky details. Markus Ackermann also helped me with the usage of the corresponding Monte Carlo data set. A great help was Prof. Dr. Dominik Schwarz. The long discussions about the spherical harmonics and the multipole moments were very fruitful. It gave me a well conception and understanding of their different properties and behaviour. With Elisa Bernardini and Andreas GroßI had several discussions about the possible background from mis-reconstructed muons. Without these informations the chapters about the background scenarios would have been more difficult. I thank Teresa Montaruli for her help with the uncertainties in the background from atmospheric neutrinos. Prof. Dr. Peter Biermann gave me important hints and information about the (super-) galactic plane. This was necessary to get a proper understanding of these objects. Also the simulation of data for these objects was not simple. Here, I got help by John Kelley; how to re-weight the Monte Carlo data in these cases.
Special thanks to the group in Wuppertal. I had a great time working here. I got a warm welcome and took advantage of a constructive and friendly atmosphere. Dr. Christopher Wiebusch and Prof. Dr. Karl-Heinz Kampert were available for questions and discussions all the time. Additionally I should mention Andreas Tepe, Heiko Geenen, Prof. Dr. Klaus Helbing and Simon Robbins for discussions about various topics. Some of them related to this thesis. An additional thanks to Simon Robbins and Karl-Heinz Becker for their persistent work on the ALiCEnext computer cluster, I needed it during my work. Andreas Tepe, Benjamin Semburg and Maria Gurtner had to share the office with me. They had answered many small (bothering) questions as well as taken part in many discussions.
Im thankful to Dr. Christopher Wiebusch, Andreas Dolfen, Heiko Geenen, Timo Karg, Simon Robbins, Benjamin Semburg and Andreas Tepe for proofreading.
Last but not least I want to mention my family and my friends for their support during the last years. My parents took over all the "small unimportant" functions of daily life and gave me the possibility to study. Special thanks to Anke and Jens for dissuading me from working all night and day. They were not very successful but we had some funny evenings.
Every one not mentioned here: sorry. I give this special thanks to you!

References

[AB05] M. Ackermann, E. Bernardini, T. Hauschildt: Combined 2000-2003 Point Source Analysis, www-zeuthen.desy.de/nuastro/protected/point/combined00-03/combined00-03.html

[Ac06] M. Ackermann: PhD Thesis (to be published), DESY Zeuthen, 2006

[Ac+6] M. Ackermann: private communication

[Ah04] J. Ahrens et al.: Muon track reconstruction and data selection techniques in AMANDA, NIM A 524, 169-194, 2004

[A+04] J. Ahrens et al.: Sensitivity of the IceCube detector to astrophysical sources of high energy muon neutrinos, Astroparticle Phys. 20:507-532, 2004

[Be03] C.L. Bennet et al.: First year wilkinson microwave anisotropie probe (WMAP) observations: Preliminary maps and basic results, 2003; astro-ph/0302207

[Bi00] A. Biron: Reconstruction Uncertanties due to Time Calibration Errors, Internal report AIR/20001101, AMANDA Collaboration, 2000

[Bi01] A. Biron: Search for Atmospheric Muon-Neutrinos and Extraterrestric Neutrino Point Sources in the 1997 AMANDA-B10 Data, PhD Thesis, Humbolt University Berlin, Berlin, Germany, 2002

[Bi02] S. M. Bilenky et al.: Absolute values of neutrino mass: Status and prospects, 2002; hep-ph/0211462

[BW01] J.N. Bahcall, E. Waxman: High Energy Astrophysical Neutrinos: The Upper Bound is Robust, physical Review D, 64(2):023002.1-023002.8, 2001, hep-ph/9902383

[By59] W. E. Byerly: An Elementary Treatise On Fouriers Series And Spherical, Cylindrical And Ellipsoidal Harmonics. With Applications To Problems In Mathematical Physics; New York; 1959.

[Co02] J. Conrad et al.: Coverage of confidence intervals for poisson statistics in presence of systematic uncertainties; hep-ex/0206034 v1, 2002

[Co03] J. Conrad et al.: Including Uncertainties in Confidence Interval Construction for Poisson Statistics; hep-ex/0202013 v2, 2003

[Co05] J. Conrad, F. Tegenfeldt: Likelihood ratio intervals with byesian treatment of uncertainties: coverage, power and combined experiments; physics/0511055 v1, 2005

[CR01] D. Chirkin, W. Rhode: Muon Monte Carlo: a new high-precision tool for tracking of myons in medium, in Heinzelmann et al.: "Proceedings of the 27th International Cosmic Ray Conference" pages 1133-1136, Hamburg, Germany, 2001

[D104] O. Deligny et al.: Comparison of two approaches for computing the angular power spectrum from a set of events; GAP-2004-007, 2004

[D204] O. Deligny et al.: Angular power spectrum estimation of cosmic ray anisotropies with full or partial sky coverage; JCAP10(2004)008, 2004

[Do05] A.G. Doroshkevich et al.: Gauss-Legendre Sky Pixelation (GLESP) for CMB maps, astro-ph/0305537 v4, 2005

[FC99] G.J. Feldman, R.D. Cousins: Unified approach to the classical statistical analysis of small signals; Phys. Rev. D Volume 57 Number 7, 1998

[Fe49] E. Fermi: Physical Review, 75:1169, 1949

[Ga90] T.K. Gaisser: Cosmic Rays and Particle Physics, Cambridge University Press, Cambridge, 1990

[Ga94] T.K. Gaisser, F. Halzen, T. Stanev: Particle Astrophysics with High Energy Neutrinos, 1994; hep-ph/9410384

[Ga98] T.K. Gaisser et al.: Gamma-Ray Production in Supernova Remnants, Astroparticle Journal, 492:219-227, 1998, astro-ph/9609044

[Ga00] T.K. Gaisser: Uncertainty in Flux of Atmospheric Neutrinos - Implications for Upward Muons in AMANDA B10, AMANDA Internal Report/20001201, 2000

[GM03] G.J. Gounaris, G. Moultaka: The flavour distribution of Cosmic Neutrinos, hep-ph/0212110v3, 2003

[Go05] K.M. Gorsky et al.: The HEALPix Primer; astro-ph/9905275 v2, version 1, 2005

[Gr97] M. Gramann: Power spectrum of velocity fluctuations in the universe; The Astrophysical Journal, 493:28-38, 20.Jan.1998

[Gr06] A. Groß, private comunication, University Dortmund

[Gu05] G. Guillian et al.: Observation of the Anisotropies of 10 TeV primary cosmic ray nuclei flux with the Super-Kamiokande-I Detector; astro-ph/0508468 v1, 2005

[H105] A.J.S. Hamilton: Power Spectrum Estimation I. Basics, 2005; astro-ph/0503603, 2005

[H205] A.J.S. Hamilton: Power Spectrum Estimation II. Linear Maximum Likelihood; astro-ph/0503604 v1, 2005

[H+05] D. Harari, S. Mollerach, E. Roulet: Towards cleaner anisotropy analyses; GAP Note 2005-047, 2005

[Ha02] K. Hagiwara et al., Review of Particle Physics, Physical Rewiew D, 66:010001+, 2002

[Ha04] J.-C. Hamilton et al.: Decoupling modes in the angular power spectrum estimation in case of a variable or partial exposure of the sky; GAP-2004-008, 2004

[Hi01] E. Hivon et al: MASTER of the CMB anisotropy power spectrum: A fast method for statistical analysis of large and complex CMB data sets; astro-ph/0105302 v1, 2001

[Hi96] G.C. Hill: Experimental and Theoretical Aspects of High Energy Neutrino Astrophysics, PhD thesis, Adelaide, Australia, 1996

[Hu99] S. Hundertmark: AMASIM Neutrino Detector Simulation Program, in C. Spiering: "Proceedings of Workshop on the Simulation and Analysis Methods for Large Neutrino Telescopes" page 276-286, DESY-Proc-1999-01, DESY Zeuthen, Germany, 1999

[IC05] IceCube Collaboration: 29th ICRC 2005, Pune, India; astro-ph/0509330

[Ja96] J.D. Jackson: Classical Electrodynamics, New York, USA, 3rd edition, 1996

[Ka99] A. Karle: Monte Carlo simulation of photon transport and detection in deep ice: muons and cascades, in C. Spiering: "Proceedings of Workshop on the Simulation and Analysis Methods for Large Neutrino Telescopes" page 174-185, DESY-Proc-1999-01, DESY Zeuthen, Germany, 1999

[LeMa] J. G. Learned, K. Mannheim: High-Energy Neutrino Astrophysics

[Li93] P. Lipari: Lepton spectra in the earth's atmosphere, Astroparticle Physics, 1(2): 195-227, 1993

[MA01] The MACRO collaboration: Matter Effects in Upward-Going Muons and Sterile Neutrino Oscillations, hep-ex/0106049v2, 2001

[MS53] H. Motz, L.I. Schiff: Cherenkov Radiation in a Dispersive Medium, American Journal of Physics, 21:258-259, 1953

[Ne04] Till Neuenhöfer: Die Entwicklung eine Verfahrens zur Suche nach kosmischen Neutrino-Punktquellen mit dem AMANDA-Neutrinoteleskop; 2004, Shaker Verlag Aachen

[Pa96] D. Pandel: Bestimmung von Wasser- und Detektorparametern und Rekonstruktion von Myonen bis 100 TeV mit dem Baikal-Neutrinoteleskop NT-72, Diploma Thesis, Humboldt-University in Berlin, Berlin, Germany, 1996

[PP04] Particle Data Group: Review of Particle Physics, Physics Letters B592,1; 2004

[Pe91] D. H. Perkins: Hochenergiephysik, 3. Auflage, 1991; Addison-Wesley Publishing Company

[Po05] R. Porrata: Propagation of muon induced Cherenkov photons through a diffuse medium, Astroparticle Physics 23 566-571, 2005

[Pr96] R.J. Protheroe: Astrophysical sources of high energy neutrinos, Adelaide, Australia, 1996, astro-ph/9612213 v1

[Pr98] R.J. Protheroe: Acceleration and interaction of ultra high energy cosmic rays, 1998, astro-ph/9812055

[PW00] P.B. Price, K. Woschnagg, D. Chirkin: Age vs. depth of glacial ice at the Southe Pole, Geophysical Research Letters, 27(13):2129-2144,2000

[PW01] P.B. Price, K. Woschnagg: Role of Group and Phase Velocity in High-Energy Neutrino Observatories, Astroparticle Physics, 15(1):97-100, 2001, arXive:hep-ex/0008001

[Ri06] B. P. Reid: Java Applets for Chemical Education - Spherical Harmonics; www.bpreid.com/applets/pousDemo.html

[Ro05] W.A. Rolke, A.M. Lopez, J. Conrad: Limits and Confidence Intervals in the Presence of Nuisance Parameters; physics/0403059 v4, 2005

[Si98] Sian Peng Oh, D.N. Spergel, G. Hinshaw; An efficient technique to determine the power spectrum from cosmic microwave background sky maps, 1998; astro-ph/9805339

[SL04] U. Schwanke, T. Lohse: Calculation of upper limits and measurement errors for small signals, Humbolt University Berlin, 2004

[St95] T. Stanev et al.: Arrival directions of the most energetic cosmic rays; Physical Review Letters Volume 75 Number 17, 1995

[St00] P. Steffen: Direct Walk II, Internal Report AIR/20020201, AMANDA Collaboration, 2000

[St02] P. Steffen: AMANDA pattern recognition, talk at AMANDA/IceCube meeting, Stockholm, 21th-25th of June 2002

[Sw97] S. Swordy, private communication, taken from: The Auger Col1aboration: The Pierre Auger Observatory - Design Report, 1997

[Te03] M. Tegmark et al.: The tree-dimensional power spectrum of galaxies from the solan digital sky survey, 2003; astro-ph/0310725

[WB99] E. Waxman, J.N. Bahcall: High Energy Astrohysical Neutrinos: An Upper Bound, Physical Review D, 59(2):023002.1-023002.8, 1999, hep-ph/9807282

[Wi02] R. Wischnewski: The AMANDA-II Neutrino Telescope, astro-ph/0204268v1, 2002

[Wo99] K. Woschnagg: Optical Properties of South Pole Ice at Depths from 140 to 2300 Meters, HE.4.1.15 in Proceedings of the 26th International Cosmic Ray Conference, Salt Lake City, 1999

[Wo00] K. Woschnagg: Preliminary (Non-Optical) Position Calibration of Strings 14 to 19, Internal report AIR/20001002, 2000

[Wo03] K. Woschnagg: Review of Ice Models, AMANDA Collaboration Meetring, Madison, June, 2003

[Ze95] G. Zech: Comparing Statistical Data to Monte Carlo Simulation - Parameter Fitting and Unfolding;ISSN 0418-9833 ,1995

Erklärung

Hiermit erkläre ich, dass ich die vorliegende Arbeit selbst verfasst habe und keine anderen als die angegebenen Quellen und Hilfsmittel verwendet habe.

Jan-Patrick Hülß, Wuppertal, Juni 2006